The Fate of Landslide Debris After Large Earthquakes, Wenchuan, China

Oliver R. Francis

2020

Thesis submitted for the degree of

Doctorate of Philosophy

Summary

Large earthquakes are significant geomorphic events in mountain ranges; they can cause uplift while also triggering huge volumes of bedrock landsliding. Constraining the erosion of coseismic landslide deposits is important for understanding the long-term impact of earthquakes on landscape evolution and natural hazards. The 2008 M_w 7.9 Wenchuan earthquake provides an excellent opportunity to constrain the processes and rates that erode landslide deposits within and out of mountain catchments. I constructed a large multitemporal landslide inventory of the epicentral region of the earthquake to map the erosion of landslide deposits in the 10 years after the earthquake. In these 10 years less than 13% of the sediment had been deposited into the stores associated with the main trunk of the orogen draining river leaving up to 88% stored on the hillslope. Debris flows were the key remobilising process, transporting over 50% of all the sediment that is mobilised. Using slope stability modelling and analysis of the landslide inventory I identified most of the debris flows were triggered on the hillslope and their frequency decreased rapidly through time. Initially debris flows were triggered in small deposits with low drainage areas but through time the landslides closer to channel network become more likely to be the source of debris flow activity, a pattern that highlights a change in the physical properties of the deposits. I evaluate several theories that may explain this pattern and highlight strategies to identify the stabilising processes. Finally, I present a 0-Dimensional model investigating the impact of storage of coseismic sediment on landscape evolution. This model suggests coseismic sediment can remain in the mountain range for timescales greater than the recurrence time of large earthquakes causing a decrease in exhumation rates as sediment is remobilised. The long storage time of sediment in orogens reduces the impact of earthquakes on long term (>1000 years) exhumation records so that single earthquakes are only recorded in the most local or highest resolution records.

Acknowledgements

PhDs are a huge undertaking which cannot be completed without significant support and encouragement and mine has been no exception. Here I would like to thank the many people who have helped me along the way, either by pointing me in the right direction or by listening to me moan about everything.

First, I would like to thank my supervisory team of TC Hales and Dan Hobley. Our regular meetings have been a highlight of my PhD. These meetings typically started with 10 minutes of tangents before 5 to 10 minutes of focussed discussion of my work followed by another 10 minutes of tangents with 5 minutes of round up at the end. While this may not be the most efficient way of running meetings, they always helped me to put my work into perspective and tighten up my research questions and objectives. I have to also thank you for your long, detailed and constructive comments on the many drafts of my manuscripts. These comments taught me not to take constructive criticism personally and to acknowledge what I had achieved.

Next, I would like to thank everyone who I shared office 1.22 with, having people to distract me from programming errors and blue screens of death definitely helped me stay sane over these last few years. In chronological order these were Josh, Huw, Alex, Erin, Lucy, Jian, Ming, and Danielle. Josh, Huw, and Alex made me feel welcome and have been very supportive over the years with my inane questions about python, jobs, conferences, and grants. Special shout out to Alex for putting up with me on trips to both Borneo and China over the last 5 years. Erin, Lucy, and Danielle made sure I never took myself too seriously and I acknowledged my successes. They have also kept me well fed with various baking and tomato growing experiments, though I do not miss the lab jungle!

I also must thank everyone from my trips to Chengdu. Jing pretty much saved my life, ensuring I could eat and navigate the city and took me on a highly memorable tour of a small part of Sichuan and the pandas. Guillem showed me how to enjoy my time away with Chinese interpretations of pizza and long nights out in bars. Vito, Dai and Fang helped immensely with the data collection of my thesis and papers and made me feel very welcome at SKLGP. And finally, Xuanmei who offered us significant portions of her time while we were in Chengdu to help us with anything we could possibly need. I still think about the food I had during my trips and I hope to taste true Sichuan cuisine again.

Finally, I have to thank my family and non-academic friends. Thank you for putting up with my moaning and talking incessantly about landslides and debris flows. I had hoped the videos of debris flows would convince you that they were super cool and interesting, but I have a feeling that it may not have worked. Thank you for all the times you forced me to think about something else and get out of my head for a while, whether that was with the world cup, trips to Devon for Easter or just drinks at the pub.

And finally finally, as I know this may be the only page of this document she will read, I have to thank Cécile for everything she has done over the last 4 years. I have put you through a lot, making you move by yourself while I was in China, forcing you to sit through many presentations about debris flows and mountain building and bad moods after hard days. You have also ensured I am a more than just an academic by encouraging me to educate myself on topics of equality, diversity and, inclusivity. Our trips away all across Europe and the UK have been the highlight of the last few years and I look forward to many more adventures with you.

Table of contents

Table of figures

Table of tables

Chapter 1 Introduction

1.1 Context

Tectonic forces form some of the highest and fastest growing mountain ranges in the world which act as the source for most of the sediment deposited into ocean basins (Avouac 2007; Larsen et al. 2014). This dichotomy of rapid growth and erosion is very visibly shown during large earthquakes. Earthquakes along thrust faults can uplift huge volumes of crust while eroding the mountain ranges via the triggering of tens of thousands of coseismic landslides (Li et al. 2014; Marc et al. 2016b). The occurrence of earthquakes has long been associated with uplift in mountain ranges with the frequency of the large earthquakes closely matching recordings of rock uplift and crustal thickening (Avouac 2007). However, while the largest earthquakes may contribute the most to rock uplift, they may not significant contributors to surface uplift. Recent large earthquakes have revealed that the largest earthquakes can produce similar volumes of landsliding and rock uplift suggesting large earthquakes can be destructive (Hovius et al. 2011; Parker et al. 2011; Li et al. 2014; Marc et al. 2016b).

Along with being powerful geomorphic events, earthquakes cause significant numbers of casualties every year. The shaking of the main and aftershocks can destroy buildings and infrastructure in a radius of many kilometres. The shaking of steep mountain ranges also triggers coseismic landslides which are linked to further deaths in mountain communities. Earthquakes have long been known to produce landsliding with the first formal study investigating coseismic landslides caused by an earthquake in Calabria, Italy in 1783 (Keefer 2002). The volume of coseismic landslides triggered by an earthquake has been correlated to the energy release, the depth of the earthquake, and the modal slope of the landscape (Malamud et al. 2004b; Marc et al. 2016a). Other properties such as the rock strength and climate also play a secondary role (Gallen et al. 2015; Marc et al. 2016a). Coseismic landslides are triggered by the motion of seismic waves produced by an earthquake. The seismic waves decrease the normal force holding the hillslope together, reducing its resistance to shear stress causing failure (Brain et al. 2015). Convex topography, such as mountain ridges, amplify the seismic waves of the earthquake causing triggering to occur high up on the hillslopes (Meunier et al. 2008; Meunier et al. 2013). The shaking can also cause damage to the hillslope without causing failure leaving cracks in the landscape and weakened substrate which can fail many years after the earthquake (Dadson et al. 2003; Hovius et al. 2011; Marc et al. 2015; Parker et al. 2015; Fan et al. 2019b). Our understanding of the triggering of coseismic landsliding has increased

significantly over the last few decades due to the rapid increase in the accessibility of high temporal and spatial resolution satellite imagery (Guzzetti et al. 2012; Marc et al. 2016a).

Coseismic landslides have been linked to over 4000 deaths between 2004 and 2016 (Froude and Petley 2018). Landsliding can destroy buildings and their deposits are sources of further hazard. Coseismic landslide deposits can block rivers producing unstable landslide lakes (Dunning et al. 2006; Fan et al. 2012a; Fan et al. 2019b) which cause flooding or can be remobilised during rainstorms in the form of debris flows (Lin et al. 2004; Tang et al. 2011). This chain of hazards is commonly referred to as the seismic hazard chain (Zhang et al. 2016; Fan et al. 2019b). The seismic hazard chain can elevate the risk of death and economic damage in mountain communities for hundreds of years. Impacts such as the enhanced rate of landsliding on damaged hillslopes may only last a few years while effects such as the aggradation of the river network can last for centuries (Yanites et al. 2010; Hovius et al. 2011; Marc et al. 2015; Fan et al. 2019b). The seismic hazard chain dramatically slows the economic recovery of an earthquake struck area by destroying rebuilt infrastructure and can force the complete relocation of communities (Huang 2011). A key component of the seismic hazard chain is the remobilisation of coseismic sediment however the processes behind the remobilisation is currently poorly understood. Coseismic landslides, generally, move sediment short distances down the hillslope before another process, or multiple processes, erodes their sediment load out of the mountain range. I term this erosion of previously deposited sediment remobilisation. The residence time of coseismic sediment is defined as the time required to remove the sediment generated by the earthquake out of the mountain range.

Sediment derived from coseismic landslides impacts landscape evolution as well as the seismic hazard chain. Earthquakes build mountains through the thickening of the crust, this thickening causes adjustment in the mantle through isostasy which depends on the increase in weight over a particular area (Turcotte and Schubert 2002). The adjustment of the crust depends on both thickening and erosion so that if the coseismic landslide deposits are rapidly removed from the orogen a rebound in the upper crust can occur (Densmore et al. 2012; Molnar 2012). Without understanding the final distribution of coseismic sediment in the landscape and its residence time, the expected isostatic response to an earthquake is unconstrainable. Along with impacting the crust's isostatic response, landslide sediment can both enhance and dampen the bedrock incision done by rivers in the mountain range (Korup et al. 2010; Yanites et al. 2010; Egholm et al. 2013; Croissant et al. 2019). Sediment can be mobilised in rivers increasing the erosion via abrasion or it can armour the channel bed preventing incision. Understanding where and how long coseismic

sediment is stored in the landscape will help to us to understand the long-term impact of large earthquakes on long term landscape evolution.

Debris flows, along with being very hazardous, can rapidly mobilise significant volumes of sediment out of catchments (Iverson et al. 2011; Ouyang et al. 2015; Horton et al. 2019). Despite their importance to the residence time of coseismic landslide material in mountain ranges and risk assessments in mountain ranges their initiation is poorly understood (Iverson et al. 1997; McGuire et al. 2017a; Tang et al. 2019). Debris flows are made up of surges of poorly sorted water laden sediment which rush downslope and through channels. The continual movement and interactions between the fluid and sediment of debris flows separate them from long runout landslides (Iverson 1997; Iverson et al. 1997). The high fluid content of debris flows allows the entrainment of sediment along their runout (Wang et al. 2003; Iverson et al. 2011). The lack of good constraints on the entrainment of sediment by a debris flow during its runout prevents prediction of their final volume, the prime control on run out length and velocity (Iverson et al. 2011; de Haas et al. 2020). The frequency of debris flows is also impacted, generally enhanced, by the addition of coseismic landslide material to catchments but, the time scale (and the processes which control its length) for which the enhancement continues is unconstrained (Bovis and Jakob 1999; Guzzetti et al. 2008; Ma et al. 2017). Debris flows are primarily triggered by two mechanisms, either the disarticulation of landslides during runout or via overland flow in steep channels (Takahashi 1981; Iverson et al. 1997). Both of these mechanisms are recorded in post-earthquake landscapes, but which is more frequent is unknown (Hu et al. 2016; Dahlquist and West 2019). Identifying the triggering processes of debris flows and how coseismic landslide deposits affect these will aid in hazard modelling and constraining the residence time of coseismic landslide deposits.

The M_w7.9 2008 Wenchuan earthquake was one of the deadliest earthquakes of recent years. Reports after the earthquake estimate 69,200 people died and 374,216 people were injured as a direct result of the earthquake (Zhang et al. 2012). Over 46 million people in total felt the earthquake due to its strong magnitude and intensity. Many of the towns along the rupturing faults were severely damaged by the shaking of the earthquake and the resulting landsliding (Huang 2011). The earthquake took place in one of the steepest mountain ranges in the world, the Longmen Shan and as a result, tens of thousands of landslides were triggered (Dai et al. 2011; Li et al. 2014; Xu et al. 2014). These landslides enhanced the casualties resulting from the earthquake in two ways, first by destroying buildings and roads, and secondly by being remobilised in the years after the earthquake. In the months and years after the earthquake, landslides which blocked rivers producing

large lakes failed and flooded towns (Gorum et al. 2011; Fan et al. 2012b; Fan et al. 2012a) while others were remobilised by rainstorms producing significant debris flows which destroyed the rebuilt infrastructure (Tang et al. 2009; Tang et al. 2011).

Following the earthquake there have been 3 major periods of debris flows, during the monsoons of 2008, 2010 and 2013 with some minor activity occurring in other years as well (Tang et al. 2009; Tang et al. 2011; Fan et al. 2019c). These monsoons were characterised by debris flows, some carrying millions of cubic meters of sediment and water out of catchments and destroying towns and crucial infrastructure. The largest flows were able to block the Min Jiang, the major river in the mountain range, and cause flooding of the towns in the valleys. These flows were significantly larger than any that had been recorded in the area and as a result the engineering work that had been put in place was not able to prevent these disasters (Tang et al. 2009; Huang 2011; Yu et al. 2013). These flows are well studied and offer an excellent insight into the role of debris flows evacuating sediment from epicentral areas and their triggering.

Currently the mechanisms of coseismic landsliding are well understood, models can predict the location, volume, and total number of landslides (Malamud et al. 2004a; Marc et al. 2016a; Robinson et al. 2016; Marc et al. 2017; Nowicki Jessee et al. 2018; Li et al. 2019) but less is known about what happens after the earthquake. It has been shown that landsliding rates and suspended sediment concentrations are enhanced after earthquakes both of which return to pre-earthquake levels within a decade (Hovius et al. 2011; Marc et al. 2015; Wang et al. 2015). The mechanisms behind the enhanced erosion rates, either of the hillslope or of sediment in channels after earthquakes, are relatively unknown. The connectivity between landslide deposits and channels is not a good indicator of the suspended sediment (Li et al. 2016a; Wang et al. 2017; Tolorza et al. 2019) leaving a catchment, implying other processes are important. Debris flows are likely to contribute to the remobilisation of landslide deposits after earthquakes due to the increase in frequency and magnitude but their role of transporting sediment has not been quantified. Equally the triggering process behind the debris flows, particularly the largest and most hazardous flows remain mostly unconstrained (Hu et al. 2016; McGuire et al. 2017a). Finally, it is commonly assumed that the majority of the coseismic sediment produced by an earthquake will be evacuated rapidly from mountain ranges due to the lack of storage space within mountain ranges (Ouimet et al. 2009; Parker et al. 2011; Li et al. 2014; Marc et al. 2016b; Li et al. 2019). This assumption allows for easy calculation of surface uplift from earthquakes and fluvial incision rates, though this assumption has not been tested. If this

assumption is not accurate, the role of earthquakes in landscape evolution could be misunderstood and be potentially underappreciated.

1.2 Research aims and questions

The main aim of this thesis is to understand the remobilisation of coseismic landslide deposits following a large earthquake, both over short (~10 years) and long (~1000's) time scales. With this aim in mind, I investigate the 2008 M_w7.9 Wenchuan earthquake and its aftermath using a combination of remote sensing, data analysis, slope stability analysis, and modelling. Each methodology has its own section and are combined in the discussion to provide an overview of the impact of large earthquakes on landscape evolution and hazards in mountain ranges. The questions each methodology seeks to answer is listed below and each build upon the observations of the previous.

Research question 1; What are the key storage and sediment transport processes of coseismic sediment after the 2008 Wenchuan earthquake? In this section (Chapter 3) I design and produce a multitemporal landslide inventory of 42 catchments in the epicentral area in order to quantify the volume of sediment remaining within the catchments 10 years after the earthquake. I also investigate the key processes remobilising the sediment and how these change through time.

Research question 2; How and where are debris flows triggered after the 2008 Wenchuan earthquake? For this question (Chapter 4) I use a combination of the multitemporal landslide inventory and slope stability modelling to identify which coseismic landslides are remobilised by debris flows and suggest triggering mechanisms.

Research question 3; How does coseismically generated sediment affect surface uplift and exhumation rates? This question (Chapter 5) is investigated using a zero-dimensional seismic volume balance model which tracks the average depth of earthquake generated sediment in the landscape and identifies how earthquakes generate surface uplift.

Chapter 2 Literature review

2.1 Introduction

The 2008 M_w7.9 Wenchuan earthquake was one of the most significant and well-studied geomorphic events in the last decade (Fan et al. 2018b). The earthquake occurred in the Longmen Shan, a mountain range on the eastern margin of the Tibetan Plateau (Liu-Zeng et al. 2009; Densmore et al. 2010). This mountain range has long been studied due to its complex tectonic history and setting (Chen et al. 1994; Burchfiel et al. 1995; Royden et al. 1997). The combination of easily accessible high temporal and spatial resolution satellite data with a well constrained tectonic setting offers the chance to investigate the short- and long-term impacts of an earthquake on a landscape. Here I review our current understanding of the formation of the Longmen Shan, the Wenchuan earthquake and its connection to local tectonics. I then present an overview of the coseismic landsliding produced by the earthquake and our current knowledge of the erosion of coseismic landslide deposits.

2.1.1 The Longmen Shan

The Longmen Shan is found on the western edge of the Sichuan Basin in China and makes up the eastern margin of the Tibetan Plateau. The mountain range is one of the steepest in the world, rising from the low relief Sichuan Basin to elevations of 6500 m within 60km (Kirby et al. 2003). This study primarily focuses on a section of the Min Jiang catchment, a deeply incised tributary of the Yangtze river (Densmore et al. 2010; Godard et al. 2010). The Min Jiang starts in the Tibetan Plateau incises through the Longmen Shan and exits into the Sichuan basin at Dujiangyan. As the river passes through the mountain range it crosses through several different lithologies and across and along faults which make up the Longmen Shan thrust belt (Figure 1) (Burchfiel et al. 1995; Chen and Wilson 1996). While these faults are significant and noted for their seismic potential, in this particular part of the orogen there has been little history of seismic activity prior to the 2008 Wenchuan earthquake (Burchfiel et al. 1995; Densmore et al. 2007).

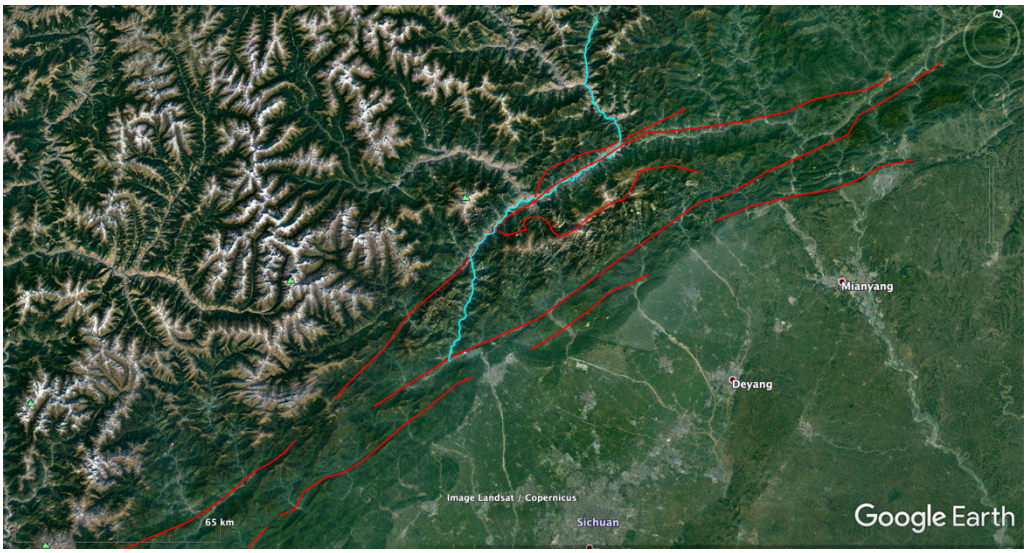

Figure 1. Satellite imagery of the foothills and front of the Longmen Shan bordering the Sichuan Basin to the South East. The major faults of the area are shown in red while a section of the main trunk of the Min Jiang is highlighted in light blue. The Min Jiang crosses and follows the main faults as it drains the orogen. Faults based upon Densmore *et al.*, 2007. The image is taken from Google Earth using Copernicus and Landsat imagery.

The Longmen Shan is noted for its long steep hillslopes and strong monsoons making it highly prone to landsliding (Ouimet et al. 2007; Ouimet et al. 2009). Much of the annual precipitation occurs during the monsoon, for example, 70 – 80% of the precipitation in the town of Yingxiu falls during this season (Wang et al. 2015; Li et al. 2016a) (Figure 2). The frontal lower part of the orogen can be densely vegetated with pine forests, shrubs and grasses being common while the higher slopes of the inner range have much less vegetation (Fusun et al. 2013; Shen et al. 2020).

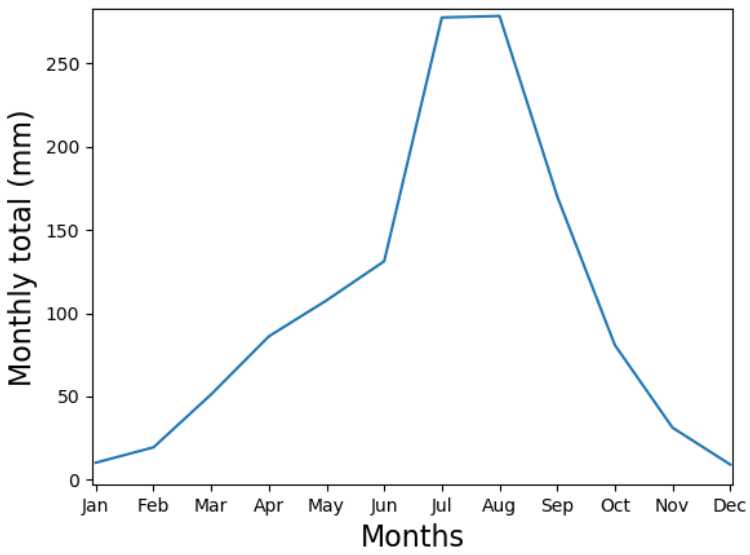

Figure 2 The distribution of precipitation in the town of Yingxiu (Zhang et al. 2014a). Yingxiu on average (based upon measurements from 1957-1981) experiences a total of 1100 mm of precipitation per year.

Due to the steep slopes of the valleys, much of the landscape is sparsely populated, however some counties and townships can be densely populated. Prior to the earthquake these included the towns of Yingxu, Beichuan and Wenchuan (Figure 3). These towns, particularly Beichuan and Yingxu were not just damaged by the shaking of the earthquake but also coseismic landsliding, flooding and significant debris flows in the years after the earthquake (Zhang et al. 2016).

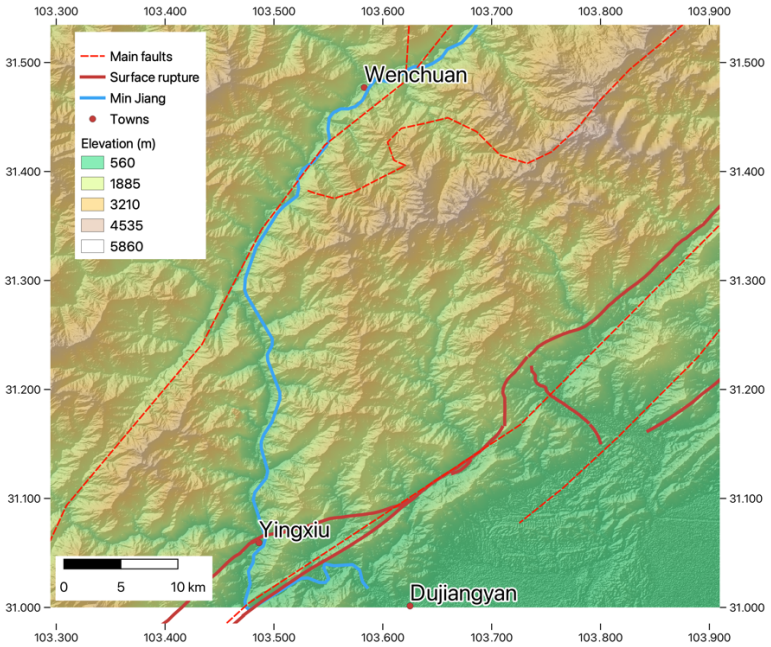

Figure 3 The locations of major towns in relation to the surface rupture of the 2008 Wenchuan earthquake. Fault locations based upon Densmore *et al.*, 2007, Surface rupture location taken from Densmore *et al.*, 2010. Elevation data made using a 30m DEM from JAXA ALOS World 3D Tadono *et al.*, 2016. Grid is in WGS 1984, 4236

2.1.2 **Tectonics and geology**

The evolution of the Longmen Shan is controlled by the complex regional tectonics of the Himalayan Orogen and the Tibetan Plateau (Burchfiel et al. 1995; Li et al. 2003; Burchfiel et al. 2008). The Longmen Shan thrust belt trends north east – south west parallel to the mountain range front (Chen et al. 1994; Densmore et al. 2007; Godard et al. 2009; Godard et al. 2010). The faults typically dip steeply (40 – 90°) to the North East and for the most part thrust their respective blocks South West towards the Sichuan Basin (Densmore et al. 2007; Hubbard and Shaw 2009; Li et al. 2014). All of these faults also have significant strike slip components. There are three main faults: the Wenchuan-Maowen, Yingxiu-Beichuan, and the Pengguan faults (from NW – SE), and all three faults have been active since the Triassic (Figure 4) (Chen et al. 1994; Li et al. 2003; Densmore et al. 2007). These faults can be mapped across the mountain range for over 200 km but are only continuous in

their centres, becoming branching at their ends (Densmore et al. 2007; Liu-Zeng et al. 2009). The Yingxu-Beichuan and the Pengguan faults were both ruptured during the 2008 Wenchuan earthquake (Hubbard and Shaw 2009; Liu-Zeng et al. 2009; Densmore et al. 2010).

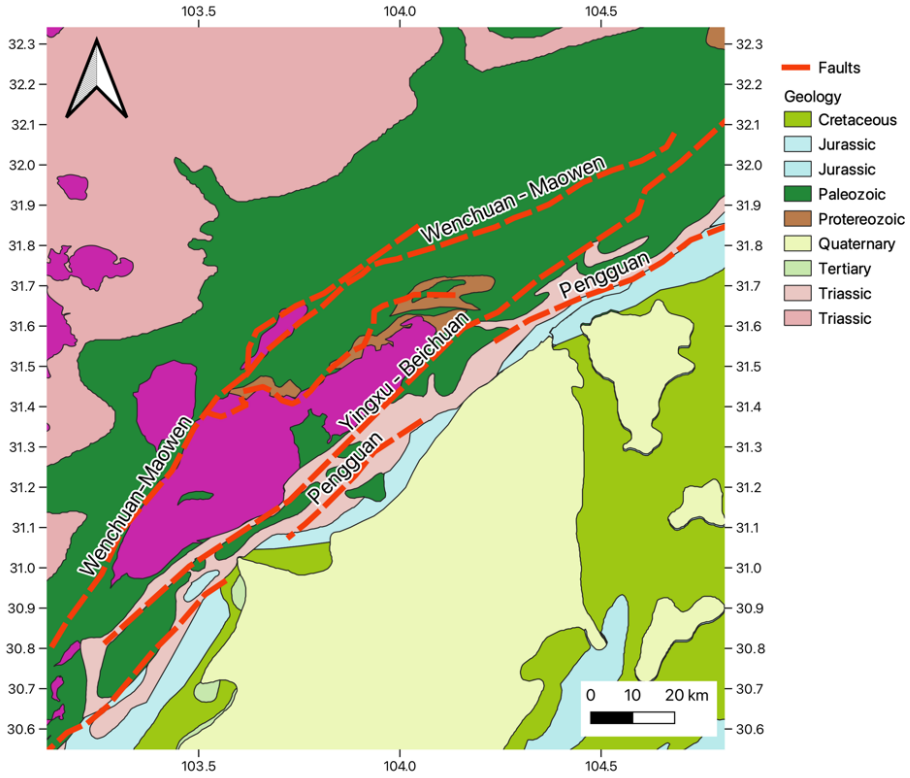

Figure 4 The major lithological units and faults of the Longmen Shan. The purple lithology is the granitic basement of the area. Geology shapefiles based upon MA, L. (2002). Faults mapped using Densmore *et al.*, 2007

The Longmen Shan is characterised by two significant periods of deformation beginning in the Late Triassic and Miocene, with several smaller events occurring both prior and between these periods (Burchfiel et al. 1995; Chen and Wilson 1996; Burchfiel et al. 2008). The Late Triassic Indosinian orogeny caused several crustal blocks to accrete on to the South China block and Eurasian plate during the closure of the Palaeo-Tethys Ocean (Chen and Wilson 1996; Li et al. 2003; Densmore et al. 2007). This period of compression produced several thrust faults which are in similar locations to the currently active faults. The deformation is primarily recorded in the westerly Songpan-Ganze Terrane as folded triassic beds of greywacke and turbidite sequences (Figure 4, light pink NW) (Kirby et al. 2003; Li et al. 2003; Densmore et al. 2007). The Songpan-Ganze Terrane is commonly described as a flysch due to its primarily marine nature showing a shift from deep marine to shallow sea sandstones. These deformed beds are unconformably thrust over the Protozoic Basement by the Wenchuan-Maowen Fault which itself is thrusted over basin

sediments (Li et al. 2003; Burchfiel et al. 2008). The Protozoic basement block, typically known as the Pengguan Massif or Pengxian-Guanxian Basement Complex, is bordered by the Wenchuan-Maowen Fault to the West and the Yingxu-Beichuan Fault to the East (Figure 4). The lack of basin sediment indicates this area was a topographic high prior to the Indosinian Orogeny (Chen and Wilson 1996; Li et al. 2003). The Massif is formed of gneisses and granites with some carbonate covering (Figure 4, centre purple and dark green) (Kirby et al. 2003; Li et al. 2003; Robert et al. 2010). The Massif is thrust over a former foreland basin filled with a mixture of cretaceous terrestrial rocks and shallow carbonate rocks. Finally this basin block is thrust towards the current foreland basin, in the Sichuan Basin along the Pengguan Fault (Densmore et al. 2007; Wang et al. 2012). Thrusting along the Pengguan Fault is recorded through the Jurassic before ceasing in the Cenozoic (Chen and Wilson 1996; Kirby et al. 2003).

The second period of deformation is believed to have initiated in the Miocene with significant reactivation of the thrust belts linked to the continuing collision of the Indian subcontinent into Eurasia (Chen and Wilson 1996; Royden et al. 1997; Clark et al. 2005; Burchfiel et al. 2008; Wang et al. 2012). The Himalayan Orogeny began around 50 million years ago as the Indian Plate pushed into Eurasia in an NNE direction, closing the Tethys Ocean, and forming the frontal range of the Himalaya. As the orogeny continued, the crust experienced severe shortening creating the high Himalayan Mountains and the Tibetan Plateau. While the main orogeny across the Himalayan Frontal Thrust continues in a NNE direction the Plateau is moving in a NE direction into northern China (Figure 5) (Tapponnier 2001). The rotation of the Tibetan Plateau is accommodated by several deep and long strike-slip faults and the reactivation of previously dormant thrust faults. These reactivated thrust faults include the Longmen Shan fault zone, especially the Yingxiu-Beichuan Fault (Godard et al. 2009). However, thrusting and shortening across these faults has also been argued to be minimal due to the lack of Cenozoic material in the foreland basin and slow GPS shortening rates (Figure 6) (Royden et al. 1997; Zhang et al. 2004; Densmore et al. 2007; Burchfiel et al. 2008). Rather than thrusting activity, uplift is instead proposed to occur due to the presence of a lower crustal flow under the Longmen Shan (Royden et al. 1997; Clark et al. 2005).

It is theorised by Royden et al, (1997) that the lower crust under the Tibetan Plateau is weakened and deformed by the overlying weight of the thickening upper crust of the plateau. Under the weight of the plateau the lower crust is forced to escape laterally to areas under less pressure, in this case the Longmen Shan (Clark et al. 2005). In the Longmen Shan the flow is blocked by the thick crust of the Sichuan Basin forcing the flow

to pool and cause uplift of the frontal range with minimal shortening of the upper crust. In this scenario any thrusting activity of the faults is minimal and simply the adjustment due to the differential uplift that takes place across the mountain range (Burchfiel et al. 2008).

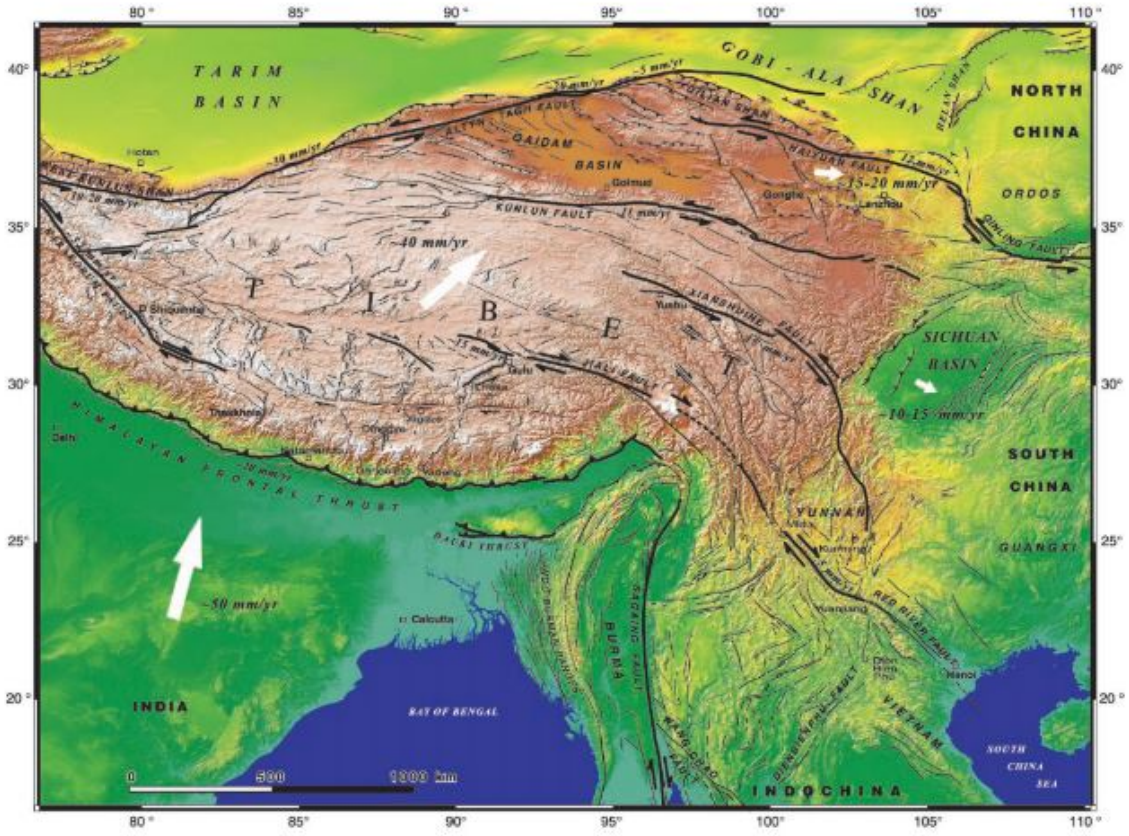

Figure 5 The movement of the Tibetan plateau constrained by recorded slip rates on faults from Tapponnier, 2001. Black arrows on faults denote the direction of the slip; large white arrows indicate areas moving faster than 5mm/yr (relative to Siberia).

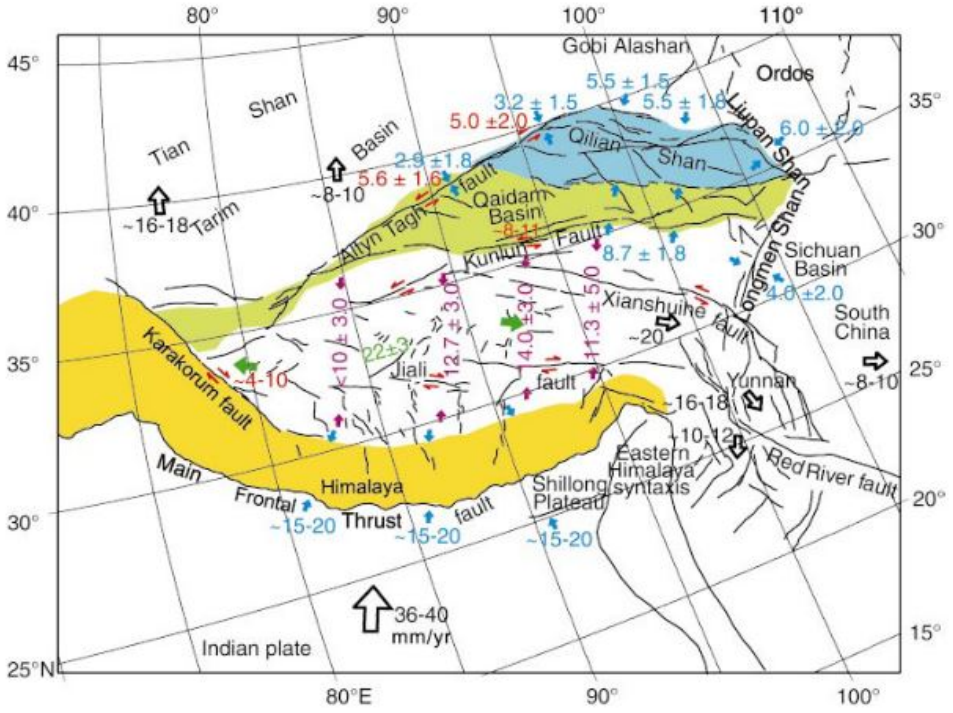

Figure 6 The tectonic motion of the Tibetan Plateau constrained by a network of global positioning systems. Blue arrows record shortening at the margins of the plateau, red arrows are strike slip, purple are shortening in the interior of the margin, green indicates extension and open arrows indicate the movement in respect to a stable Eurasia. Taken from Zhang *et al.*, 2004

2.1.3 **Surface uplift of the Longmen Shan**

There are two competing theories of surface uplift in the Longmen Shan, the first is that all crustal thickening and surface uplift occurs in the upper crust along the aforementioned faults. The second is that most of the uplift occurs because of motion in the lower more plastic crust, typically described as a lower crustal flow. Lower crustal flow driven uplift has been considered the major uplifting mechanism of the Longmen Shan since the mid 1990's (Burchfiel et al. 1995; Royden et al. 1997). If the eastward extrusion of the Tibetan Plateau was tectonically driven (as suggested by Tapponnier 2001 (Figure 5)) the thickening and resulting loading of the upper crust would have produced subsidence in a foreland basin. However geological maps demonstrate there is minimal Quaternary sedimentation in the forebasin of the Longmen Shan suggesting a lack of space for deposition i.e. no subsidence (Densmore et al. 2007). Lower crustal flow would allow for uplift to occur without loading of the crust and thus without subsidence (Royden et al. 1997; Royden et al. 2008).

GPS recordings of the eastern margin of the Tibetan Plateau indicate that the upper crust is rotating east and south between the Sichuan basin and the Eastern Himalayan syntaxis (Figure 6) (Zhang et al. 2004; Copley 2008). The surface velocities recorded by the GPS

stations are accommodated by strike slip faulting in this region. The movement also causes some compression in the Longmen Shan (Copley 2008). The velocities recorded by the GPS stations (4±2mm/yr) are significantly lower than the velocities suggested by the tectonically driven model proposed by Tapponnier (10-15 mm/yr). Geological observations along the faults in the Longmen Shan suggest that recent seismic activity has largely occurred in a strike slip fashion (1-10mm/yr) rather than thrusting (<1 mm/yr) (Densmore et al. 2007; Zhou et al. 2007; Li et al. 2016b). These observations suggest that another mechanism along with seismic activity along faults is required to account for the high mountains of the Longmen Shan and rapid movements of the upper crust (Royden et al. 1997; Burchfiel et al. 2008; Copley 2008).

Cenozoic uplift of the Longmen Shan is evidenced by thermochronometric methods. Despite the lack of evidence of shortening along many of the faults in the system, an increase in exhumation rates along the Yingxu-Beichuan and Wenchuan-Maowen Faults in the Late Miocene (Tian et al. 2013). Geomorphic studies of river channel profiles in the Longmen Shan suggest that rock uplift is greatest in areas where the highest Miocene exhumation rates are recorded (Kirby et al. 2003). The river profiles also reveal that rock uplift is not uniform across the entire orogen and in some areas cannot be linked to active faulting (Figure 7) (Kirby et al. 2003; Kirby and Ouimet 2011). The area of the highest uplift rates is found significantly far away from the frontal thrust faults which could be used as evidence for possible lower crustal thickening, however active thrust faults are likely to play a role in rock uplift as well (Kirby and Ouimet 2011).

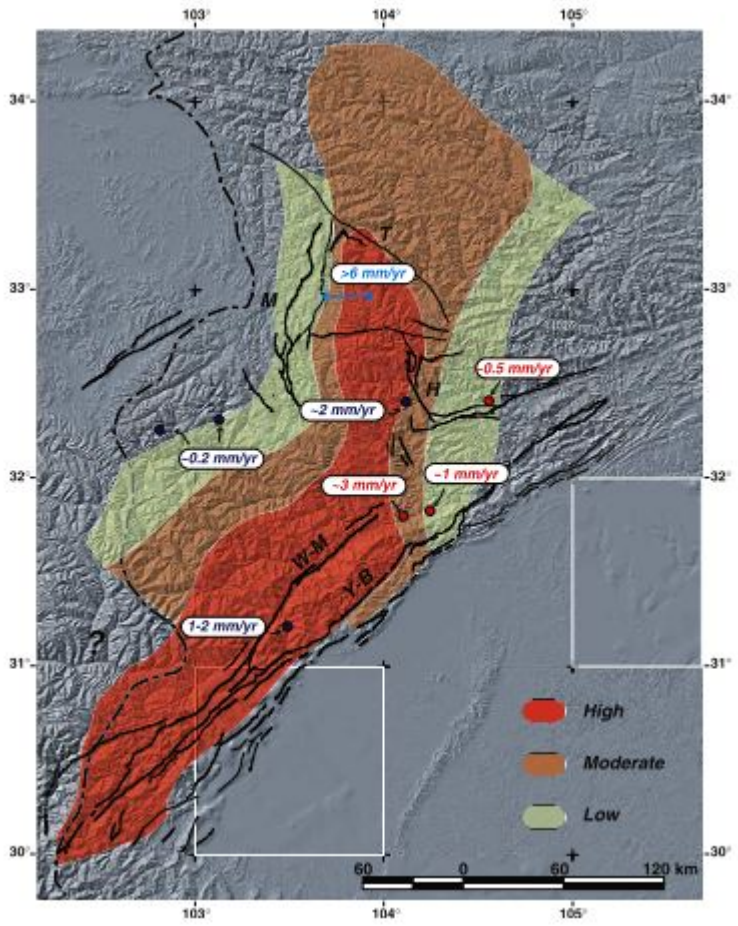

Figure 7 Estimated uplift rates derived from the steepness of channel profiles , taken from Kirby *et al.*, 2003. While the fastest uplift rates (red) are generally found near the faults, a large area (North) cannot be related to faulting activity along studied faults and thus can be related to aseismic uplift. The zones of uplift match well with estimated denudation rates. Red bubbles are the inferred incision rates from fluival terraces, dark blue bubbles are thermochronometric estimates of denudation. Light blue is an estimate of differential uplift

A complex pattern of exhumation is further demonstrated by the work of Wang et al. (2012) who use a combination of thermochronometric methods to identify 2 Cenozoic exhumation episodes in the Longmen Shan. The later (beginning 10-15Ma) has been long identified while evidence of a new older period of exhumation (25-30Ma) is also shown. This newly identified period of exhumation indicates relief has grown episodically in the Longmen Shan, rather than rapidly since the Mid Miocene. It has been proposed the earlier exhumation is related to active thrusting along the Wenchuan-Maowen Fault which was active during this time period (Tian et al. 2013). The early phase of thrusting could generate enough shortening that the entire mountain range can be built without the need for a lower crustal flow mechanism (Hubbard and Shaw 2009; Tian et al. 2013). Investigations of the 2008 Wenchuan earthquake and seismic profiles have identified that the 3 faults here are part of a listric detachment fault system which could accommodate the recorded shortening (Hubbard and Shaw 2009; Xu et al. 2009; Tian et al. 2013). Shortening along

this structure could account for up to 95% of the shortening that is recorded in the Longmen Shan (Hubbard and Shaw 2009).

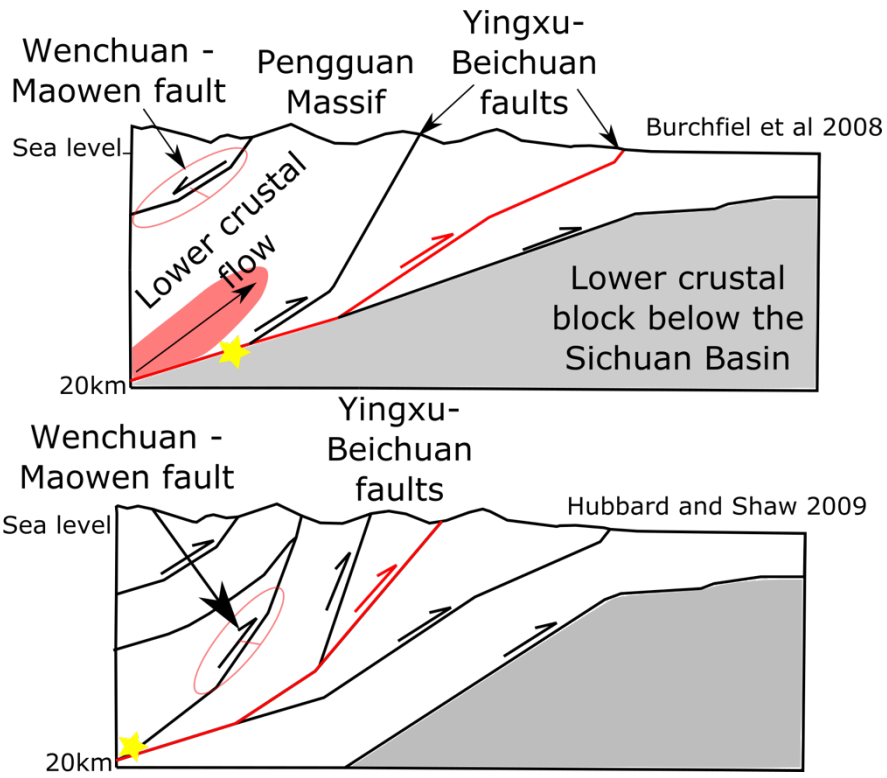

Figure 8 Two interpretations of geological cross sections and uplifting mechanisms. Burchfiel *et al.*, (2008) interpreted the Wenchuan-Maowen fault as a normal fault to allow a lower crustal flow to uplift the Pengguan Massif while Hubbard and Shaw, (2009) and Shen *et al.*, (2019) suggested it is a thrust fault to allow the Longmen Shan to be uplifted via faulting. The epicentre of the earthquake is highlighted as a yellow star and the rupturing fault is highlighted in red.

Studies of the Wenchuan earthquake and its relationship to the local tectonic setting have reopened the debate of the mechanisms producing surface uplift in the Longmen Shan. While evidence of a lower crustal flow has been interpreted from gravity analysis (Burchfiel et al. 2008) and topographic analysis (Clark et al. 2005), it is clear the thrusting potential of faults in the Longmen Shan had been underestimated (Densmore et al. 2010). Shortening has been shown to occur on all of the major faults, with or without earthquakes, and this shortening could account for the uplift in the Longmen Shan (Densmore et al. 2007; Hubbard and Shaw 2009; Shen et al. 2019). Shortening and thrusting on the Wenchuan-Maowen fault contradicts the crustal flow model which requires a normal fault to allow the crustal flow to inflate and uplift the footwall (Figure 8) (Tian et al. 2013; Shen et al. 2019). It is possible that crustal flow is present under the Longmen Shan and drives the current deformation via dragging the Longmen Shan towards the Sichuan Basin, but its

presence is not necessary to build the mountain range (Wang et al. 2012; Tian et al. 2013; Tian et al. 2018; Shen et al. 2019).

2.2 The 2008 Wenchuan earthquake

The M_w7.9 Wenchuan earthquake shook the Longmen Shan and the surrounding area on the 12th May 2008 and caused devastation in the counties of Wenchuan, Beichuan and Qingchan (Xu et al. 2009; Huang 2011; Zhang et al. 2012). The shaking produced by the earthquake destroyed buildings and infrastructure in the mountain range and caused thousands of landslides, which have been the source of many secondary hazards (Huang and Fan 2013; Fan et al. 2019b). Here I will first briefly discuss the technical details of the earthquake itself and then lead into a review of the landsliding and cascade of hazards and sediment which followed.

2.2.1 The earthquake

While adjacent to some of the most tectonically active areas in the world, the Longmen Shan had been noted for its lack of major historical earthquakes prior to 2008 (Densmore et al. 2007; Liu-Zeng et al. 2009). The faults dissecting the frontal range are long and easily traceable across the mountain range demonstrating their potential to produce massive earthquakes (Figure 4). The Wenchuan earthquake ruptured 2 of the 3 main faults of the area, the Yingxu-Beichuan and the Pengguan Faults, neither of which had been associated with major historical earthquakes prior to this event (Figure 3) (Chen et al. 1994; Densmore et al. 2007; Densmore et al. 2010).

The earthquake produced observable surface ruptures along the faults for over 220km (Liu-Zeng et al. 2009; Densmore et al. 2010). The earthquake had a focal depth of 14-19 km at the base of the Yingxu-Beichuan fault and propagated upwards rupturing the joining Pengguan fault (Figure 8) (Hubbard and Shaw 2009). While the Beichuan Fault included both thrusting and strike slip motion, the Pengguan fault almost exclusively failed in a thrusting motion (Liu-Zeng et al. 2009; Xu et al. 2009; Densmore et al. 2010). Along the Beichuan fault, thrusting was greatest in the South West and right lateral strike slip motion was greatest in the North East (Xu et al. 2009; Feng et al. 2010). The thrusting motion produced vertical ruptures of up to 10m high in some places, which when combined with the surface dip angle of the fault implies the earthquake produced significant crustal shortening (around 8.5 m) (Liu-Zeng et al. 2009; Xu et al. 2009). The significant crustal shortening produced by the earthquake was unexpected. Prior to the earthquake, GPS recordings and measurements along the fault suggested that the sense of motion on these faults were primarily strike slip (Figure 6) (Zhang et al. 2004; Densmore et al. 2007). The

Wenchuan earthquake fits largely within this trend, as it has both strike slip and thrusting components, while highlighting the fault system's crustal shortening abilities. This earthquake highlights the possibility of earthquakes missing from the geological record and issues in using short records of GPS movements to estimate long term crustal motions (Zhang et al. 2004; Densmore et al. 2010). The earthquake helped to identify the complex nature of the tectonics of the area, particularly the high connectivity of the faults. Due to this complexity it is not clear whether the Wenchuan earthquake is representative of the seismic activity on these faults (Densmore et al. 2010).

It is estimated the earthquake produced up to 7.5m of uplift along the rupturing faulting adding 2.6±1.2 km^3 of crust to the area (Xu et al. 2009; Parker et al. 2011; Li et al. 2014). However the earthquake also produced significant volumes, (~2.8 +0.9/-0.7 km^3) of erodible material in the form of landsliding (Li et al. 2014). These observations demonstrate, along with models of earthquake sequences (Marc et al. 2016b; Li et al. 2017a; Li et al. 2019), that earthquakes are important constructive and erosive agents. Understanding the triggering conditions of these landslides and the erosion of their deposits will be important for understanding hazards and the evolution of the Longmen Shan.

2.2.2 **Landsliding**

The Wenchuan earthquake is one of the most studied coseismic landsliding events of recent times (Fan et al. 2018b; Fan et al. 2019b). Landslides produced by the earthquake were rapidly identified by aerial and satellite imagery up to 100 km away from the earthquake (Huang and Fan 2013; Xu et al. 2014). After the earthquake at least 6 inventories of its coseismic landslides have been produced, mapping between 11,308 and 197,481 landslides (Fan et al. 2018b). Four inventories claim to be nearly complete giving total landslide numbers of 57,150 (Li et al. 2014), 59,108 (Dai et al. 2011), 60,109 (Gorum et al. 2011), and 197,481 (Xu et al. 2014). Each inventory uses slightly different methodologies varying from mapping the landslide deposits by hand (Dai et al. 2011; Xu et al. 2014) to running fully or semi-automated image analysis algorithms (Parker et al. 2011; Li et al. 2014). The differences in methodologies, imagery resolution and interpretation of the study authors will all contribute to the differences in reported numbers of landslides (Galli et al. 2008). In this study I use an estimate of ~60,000 landslides and a total volume of ~3 km^3 for two reasons. The first is that the total number and volume cited by Xu et al. (2014) and Xu et al. (2016) are significantly larger than the rest of the inventories. The total volume of 12 km^3 cited by Xu et al. 2016 is an order of magnitude greater than expected for an M_w 7.9 earthquake (Malamud et al. 2004b; Marc et al. 2016a).

The second reason is that the average areal landslide density is twice that of other inventories, despite mapping a significantly larger area. The study of Xu et al. 2014 offers no reasoning for these discrepancies. Without an in-depth comparison of the Xu et al. (2014) inventory it is not clear why the inventory is so significantly different from the others. I use the rounded values of ~3km^3 and ~60,000 landslides to acknowledge the differences in the other 3 inventories.

Along with estimating the total number of landslides, area and volume, inventories are important tools for understanding the magnitude-frequency relationship of coseismic landslides. Landslide inventories map the disturbed area (a combination of scar and deposit) as a polygon and use empirical scaling relationship to estimate the volumes of sediment within the polygon (Stark and Guzzetti 2009; Larsen et al. 2010). The magnitude – frequency relationship of the landslide area demonstrates that there are significantly more small landslides than large ones, but due to the exponential area – volume scaling these large landslides can contain most of the sediment produced by the earthquake (Stark et al. 2001; Malamud et al. 2004a; Stark and Guzzetti 2009). The magnitude – frequency of coseismic landslide area or volume can be approximated by a negative power law relationship for the larger deposits with a roll over in the frequency of the smallest landslides (Stark et al. 2001; Malamud et al. 2004a). The areas of the coseismic landslides of the Wenchuan earthquake follows this classic magnitude frequency shape (Figure 9). The power law of the inventory is estimated to start around 10^4m^2 and the largest landslides have an area of close to 10^7 m^2 (Dai et al. 2011; Xu et al. 2014). The largest landslide, the Daguangbao rock avalanche, has an estimated volume of 0.74 km^3 which could hold close to a third of the total sediment produced by the earthquake (Dai et al. 2011).

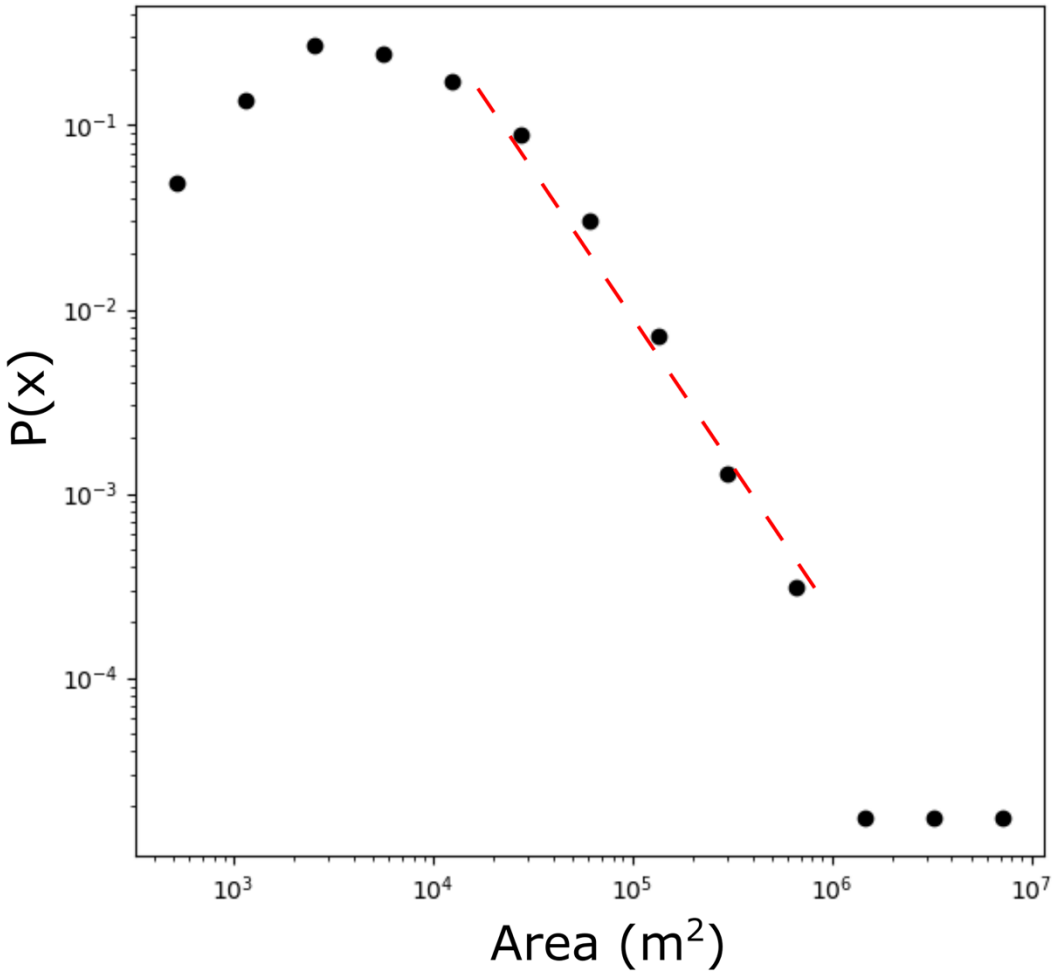

Figure 9 The magnitude – frequency of the coseismic landslide inventory of Li *et al.*, 2014. Part of the tail, marked with the red dashed line follows a negative power law until the very largest deposits.

The density of coseismic landslides has been found to vary with seismological parameters, lithology and relief (Dai et al. 2011; Gorum et al. 2011; Xu et al. 2014). Landslides are found in greater areal densities on the hanging wall of the main rupture (Yingxu – Beichuan fault), with the densities generally decreasing with distance from the fault (Dai et al. 2011; Gorum et al. 2011; Xu et al. 2014). Landslide density also correlates with coseismic slip, Peak Ground Acceleration (PGA), and seismic intensity. These findings are similar to those of previous earthquakes highlighting the strength of seismic waves is an important control on coseismic landslide occurrence (Meunier et al. 2013). Landslide density is also greatest on the steepest slopes and the weakest bedrock, particularly schists, sandstones and siltstones (Figure 10) (Dai et al. 2011). The lithologies of hillslopes closest to the faults has been shown to be significantly weaker than bedrock further away, highlighting a potential link between rock strength and seismic activity (Gallen et al. 2015). In catchments close to the fault with steep slopes and weak lithologies landslide

density can reach up to 10% choking catchments with sediment (Dai et al. 2011; Li et al. 2016a).

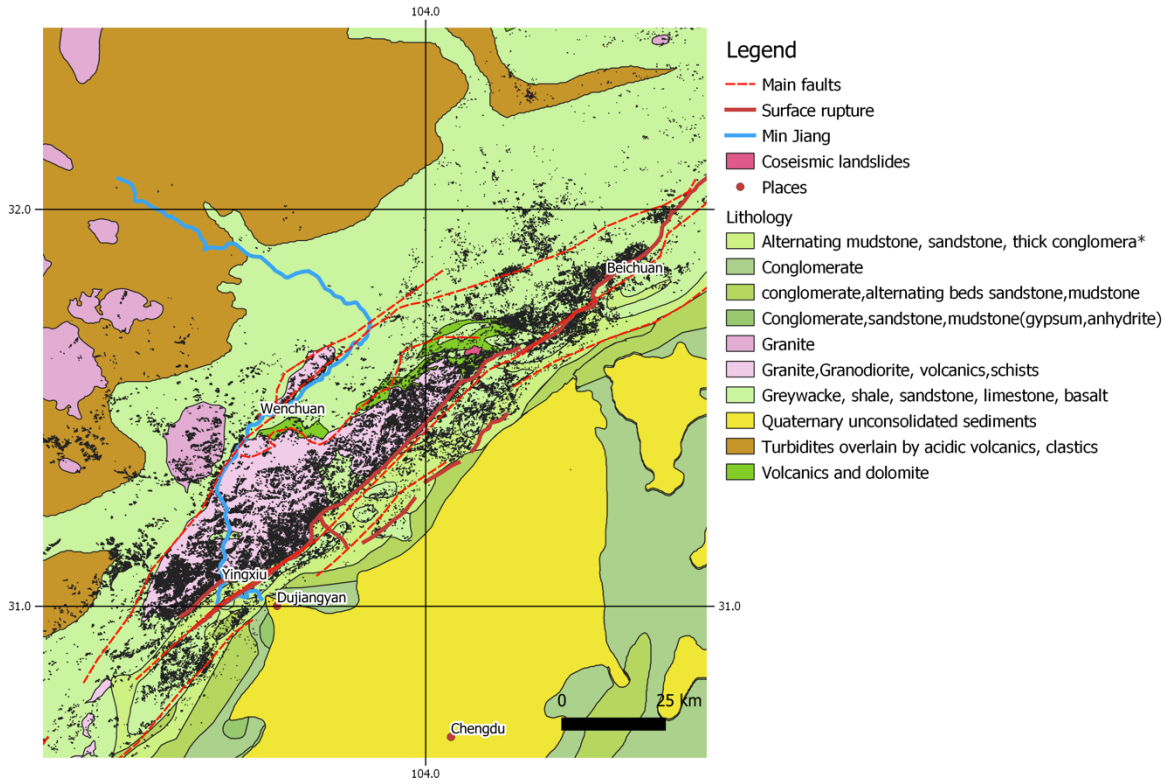

Figure 10 Coseismic landslides (here shown as black outlined polygons taken from Li *et al.*, 2014) occur in many lithologies but are found in greatest densities along the surface rupture of the faults (Bold red line). The major towns are also mapped for reference.

The correlation between landsliding density and the aforementioned factors highlight the complex nature of coseismic landslide triggering in mountain ranges. The magnitude of the seismic energy released by the earthquake drives failure with topography and hillslope conditions providing secondary controls (Dai et al. 2011; Gorum et al. 2011; Marc et al. 2016a; Valagussa et al. 2019). The combination of the shallow earthquake depth and the large magnitude of energy released produced one of the most erosive earthquakes on record (Marc et al. 2016a).

2.3 Post-earthquake sediment fluxes

The coseismic landslides triggered by the Wenchuan earthquake generated a similar volume of sediment in the Longmen Shan as was added through crustal thickening (Parker et al. 2011; Li et al. 2014; Marc et al. 2016b). If the sediment is rapidly removed from the landscape the earthquake will have not contributed to the surface uplift in the mountain range (Parker et al. 2011; Li et al. 2014). Quantifying the removal of sediment from the epicentral area of the earthquake is important for the isostatic balance of the mountain

range, landscape evolution through incision in the channel network and natural hazards (Yanites et al. 2010; Densmore et al. 2012; Molnar 2012; Egholm et al. 2013; Zhang et al. 2016).

Where a landslide comes to a rest is primarily controlled by the local slope of the surface it is traveling over and its water content (Iverson et al. 1997; Legros 2002). In general, only the most saturated landslides can travel significant distances while the majority rest on the hillslope. In Wenchuan just 43% of the sediment generated by the earthquake comes to rest near a channel (Li et al. 2016a).While in Taiwan only 8% of the landslides generated by the Chi-Chi earthquake delivered sediment into the channel network (Dadson et al. 2004). If a deposit cannot be immediately reworked by the channel system then further hillslope processes are required before the sediment can be evacuated from the catchment (Dadson et al. 2004; Hovius et al. 2011; Croissant et al. 2019). These further hillslope processes form a part of the sediment cascade which have been identified in Wenchuan and other mountainous locations (Benda and Dunne 1997; Blöthe and Korup 2013; Bennett et al. 2014; Tolorza et al. 2019). Common remobilising processes include debris flows (Benda and Dunne 1997; Howarth et al. 2012; Bennett et al. 2014), fluvial transport as suspended sediment load (Dadson et al. 2003; Hovius et al. 2011; Wang et al. 2015; Wang et al. 2017) and bedload transport (Pearce and Watson 1986; Yanites et al. 2010; Croissant et al. 2017). While these processes have been identified in the literature their contribution to long term sediment transport is unquantified.

2.3.1 **Transport by rivers, supply or transport limited?**

Immediately after many earthquakes increased suspended sediment loads in rivers draining the orogen are observed (Dadson et al. 2004; Wang et al. 2015). The enhanced rate of sedimentation is linked to landslide density suggesting that sediment from landslide deposits can be easily eroded following an earthquake (Hovius et al. 2011; Wang et al. 2015). Erosion of the landslide deposits can occur via entrainment in channel networks or surface runoff (Lamb et al. 2008; Collins and Dunne 2019), or via debris flows which can deposit large volumes of sediment into the river system (Benda and Dunne 1997; Yu et al. 2013; Bennett et al. 2014). However, the enhanced suspended sediment fluxes return to their pre earthquake levels long before all sediment can be removed from the catchments (Hovius et al. 2011; Wang et al. 2015). Catchments which rapidly respond to the increase of available sediment by remobilising the sediment, shown by an increase in the sediment flux leaving the catchment, are commonly classified as supply limited. These catchments are assumed to be capable of removing all sediment that is deposited into them as they consistently have the transport capacity to do so (Bovis and Jakob 1999; West et al. 2014).

Transport limited catchments however, only produce increased sediment fluxes when they have the transport capacity to do so, typically during storms (Benda and Dunne 1997; Zhang et al. 2019). While the simple correlation between landslide density and sediment flux implies that most catchments are supply limited, the decrease in flux before complete evacuation of the landslide sediment suggests this is an oversimplification. In the epicentral region of the Wenchuan earthquake it is likely there are both supply and transport limited catchments and these classifications may vary through time (West et al. 2014; Wang et al. 2017). Transport of fine sediment is shown to be greatest in catchments with high landslide densities and higher frequencies of large rainstorm events with high runoff (Wang et al. 2015; Li et al. 2016a). While catchments with similar landslide densities have lower transport rates due to a lack of intense rainstorms. For fine sediment the volume of sediment connected to the channel seems to be unimportant in the export of the sediment, perhaps implying in some catchments fine grained sediment is freely mobilised from hillslope and channel deposits (Li et al. 2016a). For coarser sediment the connectivity of deposits with the channel is more important, likely due to greater energy being required to mobilise this sediment (Wang et al. 2017). Coarser sediment requires greater discharges to be transported and is likely to be transported shorter distances, therefore requires deposits to be close to the channel system to be transported out of the catchment quickly. These results suggest that different sized sediment could have different residence times and transport mechanisms, thus catchments can be both supply and transport limited at different stages in time. A switch between supply limited to transport limited conditions in catchments could help to explain the decrease in sediment flux prior to evacuation of most of the landslide deposits.

The complex nature of supply and transport is revealed by sediment cores of the Zipingpu reservoir, 30 km downstream of the epicentre (Zhang et al. 2019). The sediment core shows two separate increases and decreases of grain size, the first occurred immediately after the earthquake while the second occurred after the 2010 monsoon (Figure 11) (Zhang et al. 2019). The first spike in grain size is linked to the immediate reworking of coseismic landslides in the rivers flowing into the reservoir. Once the most easily remobilised sediment, those with fine grained sediment and in sections of rivers with high discharge, is eroded the grain size returns to the long-term mean. The second spike occurs after the monsoon of 2010 which triggered a significant number of debris flows. The debris flows of 2010 transported large volumes of sediment from sub catchments and deposited it into the Min Jiang (Tang et al. 2012; Fan et al. 2019c). This sediment is then available for further remobilisation by the rivers flowing into the reservoir which then causes a second spike in

grain size. The spikes in grain size and its return to the mean grain size imply a supply limited system where the river system can easily remobilise the sediment deposited into it. However, the delivery of remobilised landslide sediment to the rivers is highly transport limited. It is also important to recognise that these cores do not record a significant increase in the sedimentation rate of the reservoir. The lack of a sedimentation rate increase can be inferred to mean that the overall discharge of sediment from the epicentre is slow due to the high volumes of sediment that are transport limited (Zhang et al. 2019).

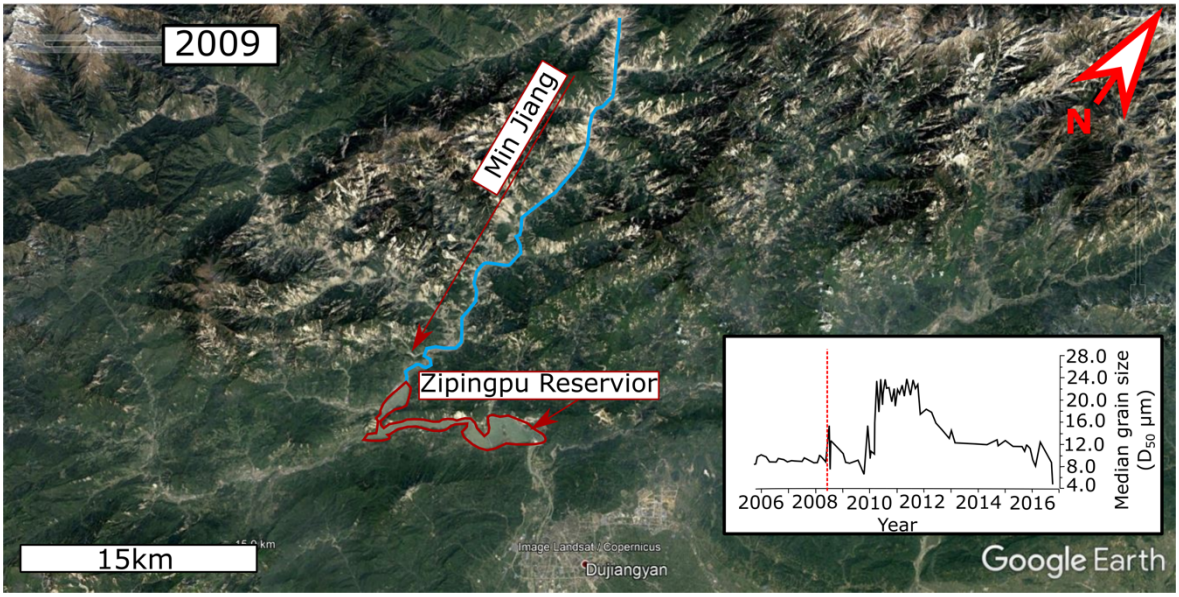

Figure 11 The location of the Zipingpu Reservoir in relation to the Min Jiang and coseismic landslides (patches of white in the satellite image). The inset shows median grain size of the dated core from Zhang *et al.*, 2019. A slight increase is seen after the earthquake, marked by the red dotted line followed by a much longer and larger peak in 2010.

2.3.2 **Debris flows**

Following the Wenchuan earthquake there was a significant increase in the frequency and magnitude of debris flows in areas with high areal landslide densities (Tang et al. 2009; Tang et al. 2012). Post seismic debris flows can occur either via completely new failures or through the remobilisation of coseismic landslide sediment (Dahlquist and West 2019). Following earthquakes the triggering of landslides, and debris flows, is enhanced due to the earthquake weakening the hillslopes (Hovius et al. 2011; Marc et al. 2015). Observations of the 1999 Chi-Chi earthquake in Taiwan revealed that sediment deposited onto stream beds during the earthquake greatly reduced the intensity-duration threshold of rainfall required to trigger a debris flow (Lin et al. 2004; Shieh et al. 2009). A similar trend is seen after the Wenchuan earthquake with the greatest decreases in the rainfall intensity-duration threshold being seen in the catchments with the largest volumes of sediment in their channels (Ma et al. 2017). The correlation between the ease for debris flows to occur

with the availability of coseismic sediment suggests debris flows are an important process for remobilising coseismic sediment after earthquakes (Tang et al. 2012; Yu et al. 2013).

The findings of decreasing intensity-duration thresholds imply that debris flows triggering is common in channels following earthquakes. However debris flows can also occur as a result of surface runoff entraining sediment on hillslopes or by the disarticulation of a landslide during its runout (Iverson et al. 1997; Larsen et al. 2006; Prancevic et al. 2014). To investigate the likely triggering mechanisms of post seismic debris flows we first have to understand the physics of how debris flows are triggered. Here I write a brief overview of our current understanding of the triggering of debris flows by focusing on the stability of sediment after deposition.

There are many types of slope stability models in the literature, ranging from topographic models which can be incorporated into GIS frameworks and more geotechnical applications focused on the stresses an individual slope experiences (Selby 1983; Wilkinson et al. 2002). These models are further separated into 1-dimensional models, such as the infinite slope model (Haefeli 1948; Taylor 1948; Milledge et al. 2012), which simply focus on the stresses holding a block in place versus those that want to pull it downslope, and 3D models which consider the external forces acting on a failing block within a slope (Milledge et al. 2014; Prancevic et al. 2018). Here I discuss 1-dimensonal models which use the factor of safety to model stability (Taylor 1948; Selby 1983) (Figure 12).

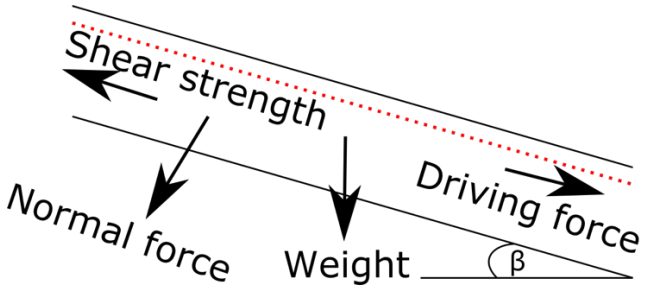

Figure 12 The infinite slope model. At the point of failure, the driving forces acting on the failure surface are equal to the normal forces holding the sediment to the slope.

An infinite slope is a homogeneous slope with a length significantly greater than its width and it is modelled at the point of failure so that all forces acting upon it are equal (Milledge et al. 2012). The model assumes a depth of failure, typically the thickness of the regolith layer (or in this case deposit thickness), to complete its stress calculations (Montgomery and Dietrich 1994; Iverson 2000). The infinite slope model is often defined in terms of a ratio of resistive forces to driving forces, called the factor of safety (F), to identify areas susceptible to landsliding.

$$F = \frac{c' + (\gamma_s - m\gamma_w)z\cos^2\beta \tan\phi}{\gamma_s z \sin\beta \cos\beta} \quad \text{Equation 1}$$

Where c' is the effective cohesion, γ_s is the unit weight of soil, m is the ratio between the height of the water table above the failure plane and the depth failure plane (z_w/z), γ_w is the unit weight of water, β is the slope angle and ϕ is the internal friction angle of the soil. The resistive forces are found on the top of the equation while the driving forces are below. The model suggests areas (typically pixels of a DEM) which may fail based on the input parameters. It cannot say anything about the timing of landsliding or the failure mode of the landslide.

Failure of sediment occurs when either the internal friction or cohesion of the sediment is decreased, pore pressure is enhanced reducing the effective normal force of the sediment, or the internal stresses within the sediment are changed. All of these processes occur in the presence of water either running into the deposit (infiltration) or over it (overland flow) (Iverson 2000; Anderson and Anderson 2010). Overland flow can apply a shear stress to the top of the deposit pulling it down slope and causing reorganisation of the grains. Reorganisation of grains in response to shear stress can cause widespread failure as a result of dilation, in compact sediment, or compaction in loose sediment (Iverson et al. 2000; Gabet and Mudd 2006; Iverson and George 2016). Infiltration can initiate failure by saturating the deposit increasing its weight and decreasing the normal stress. Many slope stability – hydrology models (Anderson and Lloyd 1991; Montgomery and Dietrich 1994; Milledge et al. 2014) use likelihood of saturation as an estimate of susceptibility to failure, while Iverson 2000 argues a pressure wave of pore pressure is required for failure. Effective normal stress is defined by

$$\sigma' = (\gamma_s - m\gamma_w)z \quad \text{Equation 2}$$

where σ' is the effective normal stress. The friction angle and cohesion can change through time, via compaction and vegetation growth; however, hydrology and the resulting reduction of the normal stress have the largest impact on slope stability during a storm event. Most slope stability models combine equation 1 with a hydrology model to estimate slope stability through time (Anderson and Lloyd 1991; Dietrich and Montgomery 1998; Iverson 2000).

The typical model for shallow landslide initiation argues during a rainstorm, water infiltrates vertically through the regolith into the ground until it meets a less permeable

surface (Figure 13). Once it meets the more impermeable layer the water begins to concentrate and move laterally, typically in a downslope direction. The rate at which water can pass through a saturated regolith is defined by its hydraulic conductivity (K).

$$K = \frac{k\rho_w g}{\mu} \qquad \text{Equation 3}$$

Where k (m^2) is the intrinsic permeability, ρ_w (kg m^{-3}) is the density of the fluid, g (m s^{-2}) is the acceleration due to gravity and μ (kg m^{-1} s^{-1}) is the dynamic viscosity. While most of these parameters can be measured or universal values can be used, the dynamic viscosity and intrinsic permeability must be estimated. The dynamic viscosity of the fluid can vary depending on the temperature of the fluid and the concentration of suspended fine sediment within the flow (Iverson et al. 1997). The intrinsic permeability is controlled by the distribution of grain sizes and shapes in the sediment and how close together they are (Anderson and Anderson 2010). The grain size distribution and their packing inside a landslide deposit (or any sediment) are not easily measured in the field due to the heterogeneous nature of sediment. Therefore the hydraulic conductivity is estimated directly from field observations or back-calculated from analysis of past landslides in the region (Montgomery and Dietrich 1994; Iverson 2000).

Deposits with high hydraulic conductivities tend to have low pore pressure build-up during storms as the water can pass through. Saturation does not occur easily in regolith of this kind making failure less likely. Typically in regolith the layers closest to the surface are the most conductive, with conductivity decreasing by several orders of magnitude with depth (Montgomery and Dietrich 1994). Hydraulic conductivity also changes dramatically with soil moisture content, becoming greatest when the regolith is fully saturated (Anderson and Anderson 2010). In a steady state hydraulic system, i.e. when the rainfall is long and has a low constant intensity slope stability models use equal rates for the vertical (in the z axis) and horizontal (in the x axis) motion of water (Montgomery and Dietrich 1994; Iverson 2000). Using an average saturated conductivity the flux of water passing through a cell in a slope parallel direction can be estimated by (Iverson 2000),

$$Q_x = b(z - z_w)K_x \sin\beta \qquad \text{Equation 4}$$

where Q_x (m^3/s) is the flow of water downslope and b is the width across which the flux is recorded. Close to the surface where the conductivity is greatest the water travels vertically but for most of the regolith profile water travels in a slope parallel direction (Figure 13). In a steady state system it is then possible to estimate the height of the water in a given cell (Dietrich and Montgomery 1998; Iverson 2000; D'Odorico and Fagherazzi 2003).

$$\frac{Z - Z_w}{Z} = \frac{Q_z}{k_x} * \frac{A}{b \sin \beta} \qquad \text{Equation 5}$$

Where A is the drainage area of the chosen point which is used as an estimate of the throughflow and Q_z is the steady state rainfall. Iverson, (2000) identifies a paradox in equation 5 where it can only be used when the conductivity of the water in the z direction is significantly larger than in the x direction. If the conductivities are similar, negative pore pressures are predicted below the water table. Therefore equation 5 can only be used in scenarios where the steady state rainfall rate or infiltration rate is significantly greater than the value used for the conductivity.

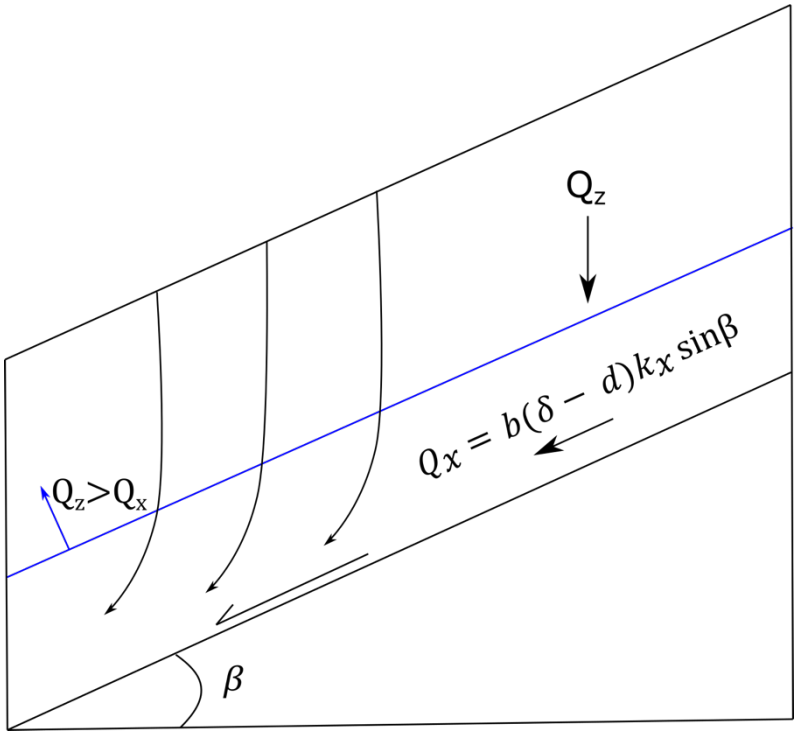

Figure 13 A conceptual model of subsurface water movement (Iverson 2000). Water infiltrates through the surface into the subsurface where it travels in the direction of gravity. Once it hits a less permeable surface (black line) it begins to move in a slope parallel direction (equation 3).

A high water table (low difference between z_w and z or low m) makes failure more likely due to the decrease in effective normal stress. However, a trigger is required to produce a failure. Failure occurs when above expected pore pressures due to hydrostatic forces are generated, commonly referred to as positive pore pressures (Iverson et al. 1997; Kaitna et al. 2016). Debris flows commonly occur in situ when the positive pore pressures become widespread producing liquefaction. Debris flows can also occur in transit when a landslide becomes disarticulated and entrains water during its runout. Positive pore pressures can be produced by a compression (or dilation) of the pores (Iverson et al. 1997; Gabet and Mudd 2006) or due to a groundwater pressure wave triggered by a rain storm (Iverson 2000).

As high pore pressures encourage failure the grains in the regolith begin to rotate. In a loose regolith this rotation causes a compression of the pore spaces dramatically increasing the pore pressure causing widespread failure (Iverson et al. 2000). The compression of the pore spaces can occur rapidly changing the failing soil into a debris flow. Dense regolith however is much slower to fail due to lower hydraulic conductivity and a stop start nature of failure (Iverson et al. 2000). The initial failure in dense regolith occurs in a similar way to loose soils but rather than pore spaces being compressed they dilate (Figure 14). This dilation causes failure to pause while pressure builds back up. Grain rotation initially occurs rapidly but as the porosity comes closer to the critical porosity they rotate less and less causing less pausing (Gabet and Mudd 2006). Once the grains reach their critical porosity widespread failure occurs. If the hydraulic conductivity of the dense regolith is too low the critical porosity cannot be reached and failure occurs as a slump rather than a debris flow (Iverson et al. 2000; Gabet and Mudd 2006).

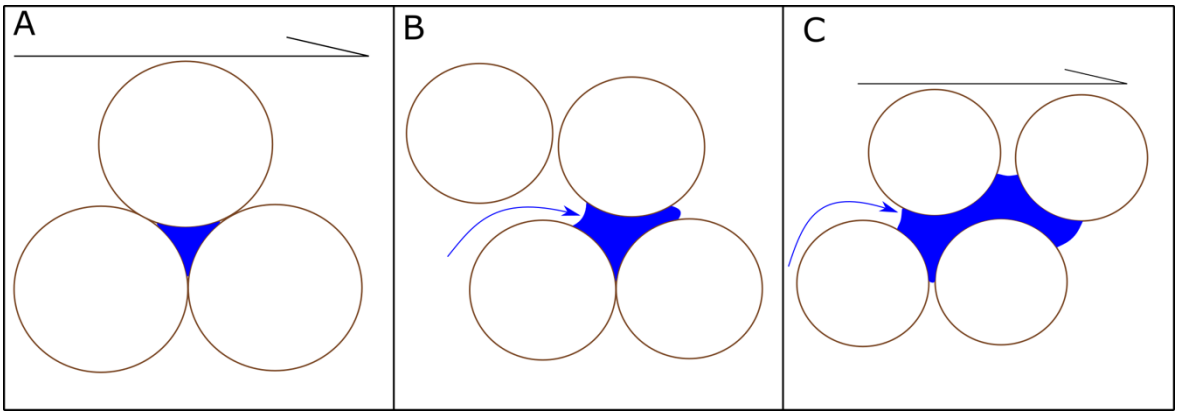

Figure 14 Grain movement during failure A) Shear stress is applied to a dense mass of grains, the shear pulls a layer of grains away from the other dilating the pore spaces and reducing the pressure preventing failure. B) If the conductivity of the sediment is high enough water can enter the new space and continue failure. C) The porosity of the sediment reaches a critical state and the failure becomes catastrophic and a landslide is triggered.

Debris flows do not just form due to saturation of regolith on hillslopes. Another common triggering process occurs in steep channels during intense rainstorms. While the triggering process of debris flows is hard to detect in imagery, Figure 15 shows evidence of debris flows passing through steep channels, possibly after triggering within them. Here rather than liquification of the deposit occurring, flow within the channel provides a shear stress which initiates failure. The rate at which this sediment can be removed is controlled by the steepness of the slope and frequency of intense rainstorms. Debris flows initiating in channels (hillslope triggered debris flows eventually end up in the channel as well) can be triggered by many different processes. Here I focus on two separate processes; debris flows can occur due to gradual entrainment of sediment or they can be triggered by the collapse

of a sediment dam or channel bed (Lamb et al. 2008; Prancevic et al. 2014). Prancevic et al (2014) identified a slope threshold between these two processes; channels with slopes above 22^0 are prone to channel bed collapse, while channels shallower than this threshold tend to be characterised by entrainment (Figure 16).

Figure 15 Debris flows triggered in coseismic sediment deposited into steep channels. Flow direction is indicated by the red arrows.

The initiation of debris flows in channels is commonly modelled by a combination of Shields critical shear stress and the factor of safety (Takahashi 1981; Prancevic et al. 2014). Flow passing over the regolith on the channel bed applies a shear stress to saturated sediment encouraging failure (Takahashi 1981; Iverson et al. 1997). The flow causes failure by increasing the driving forces on the sediment without liquefaction. It is typical to assume that the sediment within the channel has no cohesion so that failure simply occurs when the normal force holding the sediment into the slope is overcome. This triggering is described by Takahashi's channel bed failure equation (Takahashi 1981; Prancevic et al. 2014),

$$t_c^* = (1-\eta)(\tan\phi - \tan\beta) - \frac{\rho_w}{\rho_b}\tan\beta \qquad \text{Equation 6}$$

where the dimensionless shear stress required for failure (t^*_c) depends on the porosity of the failing sediment (η), the difference between the friction angle (ϕ) and slope angle (β) and the bulk density of the sediment (ρ_b). In this formulation of slope stability, at the point of triggering the "grain density" pulling the regolith downslope (first term) is equal to the normal force (second term) holding the sediment into the slope (Takahashi 1981). Due to

the non-dimensional nature of this model, neither of the term are defined as actual forces. This model can be used on open hillslopes along with channels, however the lack of cohesion, consideration of liquefaction, and vertical movement of groundwater suggests it is likely to severely underestimate the number of likely locations of failure on hillslopes (Takahashi 1981; Iverson et al. 1997).

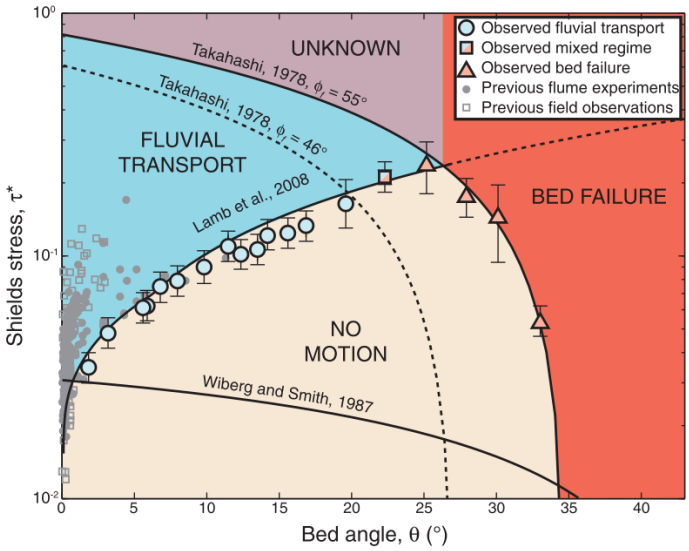

Figure 16 Entrainment of sediment in steep channels. Movement of grains in a channel can occur by 2 different processes, entrainment or debris flow (Prancevic et al. 2014). Any channel with a bed angle of greater than 22 can be susceptible to debris flows

Between 2008 and 2017 over 500 debris flows were recorded catchments affected by the Wenchuan earthquake (Fan et al. 2019c). 147 of these debris flows deposited into the Min Jiang, contributing millions of cubic meters of sediment. Debris flows can transport all sizes of sediment from the finest clay grains to meter scale boulders so are perfect for transporting sediment produced by landsliding (Iverson 1997; Dunning 2006). The largest debris flows are likely to be the largest single events to deposit sediment into the Min Jiang, however as with landslides the distribution of debris flow volumes is likely to be a power law (Bovis and Jakob 1999; Bennett et al. 2014). Typically only the debris flows which cause damage to infrastructure and endanger lives are recorded however, the smaller debris flows are also important to sediment transfer to mountainous streams (Figure 15) (Guo et al. 2016b; Zhang et al. 2016; Roback et al. 2018; Dahlquist and West 2019). These flows need to be quantified and compared to other processes to further our understanding of post-earthquake sediment budgets.

The enhanced debris flow frequency and suspended sediment loads have been shown to be very transient, though the timescale of the enhanced erosion rates is linked to the magnitude of the landslide event (Hovius et al. 2011; Wang et al. 2015; Guo et al. 2016b; Wang et al. 2017). The controls on the timespan of the enhanced erosion rates are unknown; plenty of sediment remains on the hillslope and in channels so a simple evacuation argument cannot be made. Instead, it is likely the coseismically generated sediment stabilises, to understand the stability of the sediment we need to be able to constrain the material parameters discussed in equations 1 – 5. The material properties of the deposits are difficult to constrain due to the size and heterogeneity of the deposits, both within the deposit and across the landscape (Dunning 2006; Weidinger et al. 2014; Roda-Boluda et al. 2018). The key controls on the stability of a deposit are its cohesion, degree of compaction, and its grain size distribution (Iverson et al. 2000; Gabet and Mudd 2006; Anderson and Anderson 2010).

Cohesion in regolith can either be physical produced by roots of vegetation binding grains together (Dietrich and Montgomery 1998; Wilkinson et al. 2002; Hales 2018) (vegetation also increases shear strength of regolith but is commonly attributed to cohesion) or chemically by cementation of grains via the precipitation of minerals or the electrostatic bonds between clay minerals (Anderson and Anderson 2010). However, in a landslide deposit cohesion is assumed to be low due to the lack of vegetation and the fracturing of larger blocks into smaller part via physical processes during a landslide's runout.

The degree of compaction affects slope stability in two ways. The first is by controlling the contact between grains which in turn sets the internal friction or angle of friction and the second is by controlling permeability and porosity (Selby 1983; Iverson et al. 2000; Iverson 2000). The permeability of a deposit is the main control on the hydraulic conductivity of the deposit (Anderson and Anderson 2010). The permeability is in turn controlled by the grain size distribution (Gabet and Mudd 2006) and hence the hydraulic conductivity (Figure 17). The presence of fine material can also increase the viscosity of the fluid passing through the deposit enhancing pore pressures (Iverson et al. 1997; Iverson 1997; Anderson and Anderson 2010; Kaitna et al. 2016). A fresh landslide deposit is likely to have a low degree of compaction with a wide range of grain sizes, from meter wide boulders to microscopic clay particles (Dunning 2006; Chang et al. 2011; Cui et al. 2014; Weidinger et al. 2014). Initially the deposit will be loose with larger grains being held within a loose matrix of smaller grains producing a high hydraulic conductivity (Dunning 2006).

In flume experiments water has been shown to flow through deposit sediment and entrain fine grained sediment (Cui et al. 2014; Hu et al. 2016; Hu et al. 2018). It is proposed the removal of fine sediment can increase the conductivity of the deposit while also encouraging compaction. However, this internal erosion and resulting compaction has not been documented in the field. I will discuss the evidence for this effect and its likely impacts on deposit stability further in chapter 4.

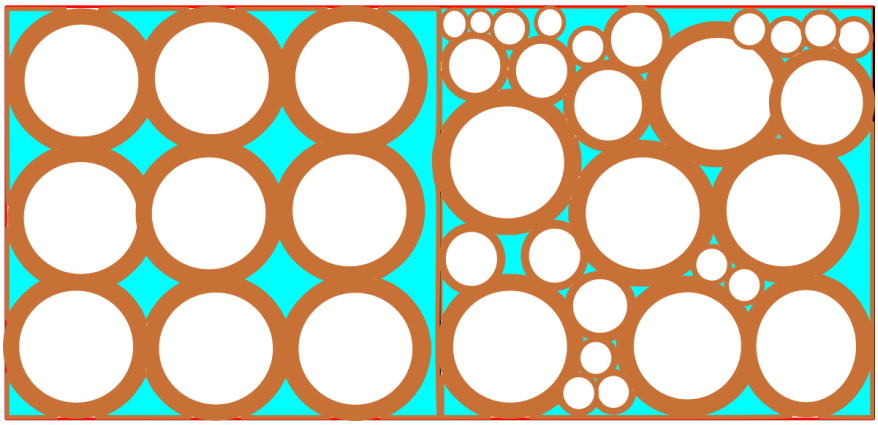

Figure 17 Permeability and grain size distribution. Grains are shown as circles with brown outline while water is blue. Deposits with uniform grain size distributions are more permeable than poorly sorted deposits. Poorly sorted deposits can have blocked hydraulic pathways which allows pore pressure to build producing failure.

Coseismic landslides associated with the Wenchuan earthquake occurred in several different lithologies, primarily occurring in interbedded sandstones and siltstones, granitic and carbonate rocks (Figure 10) (Dai et al. 2011; Gorum et al. 2011; Xu et al. 2014). The sedimentary rocks are highly weathered and jointed while the massive but weathered granites remain relatively intact. There has been some anecdotal evidence of a link between the size and type of the landslide with the rock type, with small rockfalls occurring in hard rocks and large deep seated slides in softer rocks (Gorum et al. 2011; Chen et al. 2012). The range of landslide type, lithology and weathering state suggests that variation in grain size distributions and other material properties should be expected.

Field observations and limited geotechnical studies of the Wenchuan region have indicated that coseismic landslide deposits are generally coarse in nature but with a significant (up to 20%) volume of fines (< 2mm) (Cui et al. 2014). The deposits have high porosity and permeability. The high permeability produces highly conductive deposits which water can easily pass through (Cui et al. 2014). Friction angles, estimated from field measurements of deposit surface slope, vary between 28.8 and 44.7 degrees with the smallest friction angle proposed to occur in the loosest deposits (Wang et al. 2013). A variety in grain size distributions, friction angles, and compaction is likely to exist across the landscape which

suggests that a wide range of responses to rainfall in the landslide deposits should be expected. Without a true understanding of the controls of landslide deposit stability, the residence time of sediment cannot be estimated. If the most mobile sediment is removed first, it is likely the remaining sediment will stay in catchments for similar time scales to earthquake return periods (Pearce and Watson 1986; Dadson et al. 2004; Hovius et al. 2011; Zhang et al. 2016; Croissant et al. 2019).

2.3.3 **Bedload transport**

While the volume transported by suspended load and debris flows may return to pre-earthquake levels within a decade of the earthquake, the sediment transported by the bedload does not. Bedload is normally moved slower than suspended load in rivers due to the large size of particles and its dependence on the discharge and topography of the channel network (Davy and Lague 2009; Yanites et al. 2010). Sediment moves through the landscape via a series of erosion and deposition steps, defined by a transport length of the channel. Channel sections with short transport lengths are transport limited and are typically characterised by deposition while those with long transport lengths are supply limited and characterised by erosion (Davy and Lague 2009). The transport length of the channel section is controlled by the discharge of the channel, the settling velocity of the sediment and the transport mechanism of the sediment in the flow. In general, the larger the river and the smaller the grains of the sediment, the more likely the channel is to be detachment limited. The relationship between channel size and transport length implies that the sediment from coarse landslide deposits is likely to travel slowly through the channel system.

Initially the river system will incise through the deposit in order to return to its base level (Croissant et al. 2017). The incision can occur rapidly and mobilise significant volumes of the sediment. The eroded sediment is then transported along the channel network via a series of deposition and erosion events (Davy and Lague 2009; Croissant et al. 2017).

As the channel erodes downwards through the loose sediment it produces steep bank walls which can collapse preventing further incision (Hu et al. 2016; Croissant et al. 2017; Major et al. 2019). The combination of mass wasting of the channel banks and removal of the bedload widens the river and encourages lateral erosion. The widening processes are much slower than the initial incision and will last until the remaining deposit is out of reach of the lateral movements of the channel (Major et al. 2019). The period of widening is greatly influenced by further disturbances: storms can cause incision and rapid widening while deposition requires further erosion or can divert the flow. Once the easily erodible

sediment is removed the sediment flux it carries will stabilise. In Taiwan widespread alluviated channels were observed 10 years after the Chi Chi earthquake suggesting the river systems were continuing to adjust to the sediment input from the earthquake (Yanites et al. 2010; Hovius et al. 2011). Large landslide deposits force river systems to laterally adjust due their significant volume and can remain in landscapes for thousands of years, potentially enhancing sedimentation rates for as long as they remain in the system (Korup 2005; Korup and Clague 2009; Korup et al. 2010). Incision into the bedrock by the channel can only reoccur once the sediment from the landslide has been removed from the channel reach (Davy and Lague 2009; Yanites et al. 2010; Egholm et al. 2013). The time for complete removal of landslide sediment from a particular reach is unknown but could be as long as 10,000 years (Korup 2005; Korup et al. 2010; Harrison et al. 2015; Croissant et al. 2017; Major et al. 2019).

2.3.4 **Estimates of the residence time of coseismic landslide sediment**

Storage in mountain ranges is assumed to be minimal in many studies of tectonic mass budgets and surface uplift (England and Molnar 1990; Parker et al. 2011; Li et al. 2014; Marc et al. 2016b). Tectonically active mountain ranges typically have hillslopes close to their threshold angles which prevent significant deposition while many channels are characterised as bedrock or mixed bedrock-alluvial for most of their lengths within an orogen (Montgomery and Brandon 2002; Whipple 2004; Ouimet et al. 2009). The characterisation of river systems as being primarily bedrock is used as evidence for low storage of sediment in many orogens. Despite this characterisation large volumes of sediment, in some cases over 1km^3, can be trapped and stored in terraces and valley fills (Pratt et al. 2002; Blöthe and Korup 2013; Stolle et al. 2017) and large landslide deposits (Korup and Clague 2009; Marc et al. 2019). Cosmogenic nuclide dating of sediment stores in mountain ranges suggest they are capable of storing sediment for over 1000 years, and in some extreme cases residence times of 100,000 years are possible (Korup and Clague 2009; Straumann and Korup 2009; Blöthe and Korup 2013) Large scale storage of sediment has implications for isostatic rebound (Densmore et al. 2012), channel incision (Ouimet et al. 2007; Yanites et al. 2010; Egholm et al. 2013) and the recording of erosion rates via geochemical methods (Niemi et al. 2005; Dingle et al. 2018) or sediment flux measurements (Korup et al. 2004; Major et al. 2019). Quantifying the storage of sediment and its reworking is important for understanding the long-term evolution of a mountain range.

Previous studies of post-earthquake sediment fluxes have offered some insight into the storage and evacuation times of coseismic landslide deposits. 50 years after the M_w7.7

Murchinson earthquake (South Island, New Zealand) 50-75% of the coseismic sediment remained within 10km of the source areas (Pearce and Watson 1986). Much of this sediment was still on the hillslope with one third of the landslide deposits undisturbed since the earthquake. Pearce and Watson (1986) found that coseismic landslide deposits in the channels had undergone limited reworking and there was evidence of the deposition of fine sediment behind landslides which dammed channels. The channel network affected by the earthquake was generally of a low stream order (<4) and had a low gradient suggesting a transport limited regime (Pearce and Watson 1986). The deposits would require large storms and floods before they could be mobilised and it is likely the transport length of the area is short, implying multiple large storms would be required to mobilise the sediment significant distances (Davy and Lague 2009).

Observations from the 1999 M_w7.6 Chi Chi Earthquake in Taiwan revealed that in the 12 years after the earthquake less than 5% of the coseismic material had been removed from the epicentral catchments (Hovius et al. 2011). Only 8% of landslides deposited sediment directly into the river network suggesting significant volumes of sediment remained on the hillslope (Dadson et al. 2004). The timescale for material entering the river network is unknown but due to the large volume of sediment on the hillslope and the stochastic and infrequent nature of remobilisation it could take longer than a seismic cycle to be evacuated (>10^3 years) (Hovius et al. 2011; Croissant et al. 2019). Once the sediment is deposited in the river system modelling of bedload capacity and rates suggest it could take a further 600 years for the sediment to be evacuated (Yanites et al. 2010). The Chi Chi earthquake was unusual due to the extensive post seismic landsliding which occurred during strong monsoons after the earthquake (Dadson et al. 2004; Hovius et al. 2011). The enhanced erosion following the earthquake has led to suggestions the Chi Chi earthquake contributed very little to the surface uplift of the orogen (Hovius et al. 2011).

In Wenchuan the mapping of coseismic landslide deposits reveals that most of the coseismic sediment is unconnected from the channel network (Li et al. 2016a; Zhang et al. 2016). Debris flows triggered in the loose sediment produced by the coseismic landslide deposits can move large volumes of sediment from catchments (Benda and Dunne 1997; Tang et al. 2009; Bennett et al. 2014). Enhanced debris flow activity is believed to have removed around 10% of the coseismic landslide sediment from catchments in the 8 years after the earthquake (Zhang et al. 2016; Fan et al. 2018a). There has not been a systemic study of sediment storage or long-term sediment fluxes in the Longmen Shan which makes estimates of residence time difficult. Many studies assume long term storage is uncommon (Ouimet et al. 2009; Parker et al. 2011; Li et al. 2014) but large landslide deposits and

temporary lakes along with alluvial terraces suggest that sediment can be stored sporadically across the mountain range (Densmore et al. 2007; Ouimet et al. 2007; Godard et al. 2009; Fan et al. 2019a). Measurements of suspended sediment from the Chinese Bureau of Hydrology collected and analysed and compared with landslide grain distributions by Wang et al (2015) suggest that sediment (<0.25mm) from coseismic landslides could take up to 100 years to be removed from the orogen. While Wang et al (2017) used a model comparing cosmogenic nuclide concentrations in rivers (0.25 – 1 mm sediment grains) and coseismic landslide deposits to estimate that some catchments may retain sediment for over 1000 years.

Modelling on catchments in New Zealand suggest similar residence times for sediment as indicated by preliminary results from the Wenchuan earthquake. A physically based model of fluvial erosion of landslide deposits suggests it could take 10s of years to completely erode them (Croissant et al. 2017). While an empirical model estimating hillslope transport from surface runoff records suggest deposits can remain on hillslopes for hundreds or thousands of years (Croissant et al. 2019).

All of these studies on post-earthquake sediment fluxes highlight the fact that landslide derived sediment is likely to remain in an orogen for a significant time, likely 100s or 1000s of years. Many of the studies estimate residence or transport timescales of sediment in very specific areas using large assumptions. For example, many modelling studies use a median grainsize and assume this number can characterise all of the sediment produced by the earthquake. However, the large variability of grainsize in landslides (from clay to boulders) suggests this is very likely to produce an underestimation of residence time. Equally they tend to assume a constant discharge of water in the channels moves the sediment which ignores the likely importance of the large infrequent events which can rapidly remove large volumes of sediment. Finally, there is a lack of long term studies of sediment transport in mountain ranges so it is not possible in most cases to significantly constrain the residence time of sediment or the importance of different processes beyond an order of magnitude.

2.4 Research themes

Identifying and quantifying the key processes exporting sediment from the orogen is important for understanding the long-term evolution of mountain ranges in response to earthquakes. If sediment from earthquakes remains on hillslopes for multiple earthquake cycles, erosion from earthquakes may be overestimated due to the remobilisation of old sediment rather than continuous bedrock erosion (Hovius et al. 2011; Li et al. 2017a).

Constraining the transport of sediment from hillslopes to channels remains complex but important to understand. The residence time of coseismic sediment is further complicated by the lack of understanding of its stabilisation in channel deposits and on hillslopes (Marc et al. 2015; Zhang and Zhang 2017; Hu et al. 2018). Understanding the continued stability of the sediment remaining in the epicentral areas of earthquakes is vital to building risk assessments for rebuilding communities in earthquake prone areas (Huang and Fan 2013; Zhang et al. 2016; Fan et al. 2019b).

The Wenchuan earthquake offers a unique opportunity to explore these questions. It occurred in a well-studied area with good coverage of high-resolution satellite imagery. Large debris flows are well recorded due to important infrastructure in the area and suspended sediment load is tracked daily by local gauging stations. The huge number of landslides and volume of sediment produced by the earthquake means that the wide range of processes that occur can be identified, mapped, and quantified. The mechanisms of the earthquake and the ruptured faults are well understood which helps to provide constraints on long term modelling of the impact of earthquakes on long term landscape dynamics.

Chapter 3 The sediment budget of the Wenchuan earthquake

3.1 Introduction

3.1.1 Author contributions

This chapter is adapted from a manuscript submitted to Nature Communications. The Manuscript is authored by myself, Xuanmei Fan, TC Hales, Daniel Hobley, Qiang Xu and Runqiu Huang. The multitemporal landslide inventory described here and in the manuscript was designed and constructed by myself, XF and TH with additional help from students based at the Chengdu University of Technology. I conducted the analysis and construction of the sediment budget with input and discussion from TH and DH. XF, TH, QX and RH obtained the necessary funding and contributed to the overall project aims. I rewrote the manuscript into this chapter with minimal input from my supervisory team.

3.1.2 Context

A sediment budget is the simplest form of modelling a landscape and forms the basis of our understanding of landscape evolution (Dietrich et al. 1982). A sediment budget is the quantification of the sediment production, erosion and deposition in one or several catchments (Dietrich et al. 1982; Brardinoni et al. 2009; Straumann and Korup 2009; Gran and Czuba 2017). Modelling of a landscape requires understanding the processes by which sediment is produced, transported and, deposited and how they are affected by climate and tectonics. Sediment budgets help inform these studies and supply constraints to enable accurate modelling.

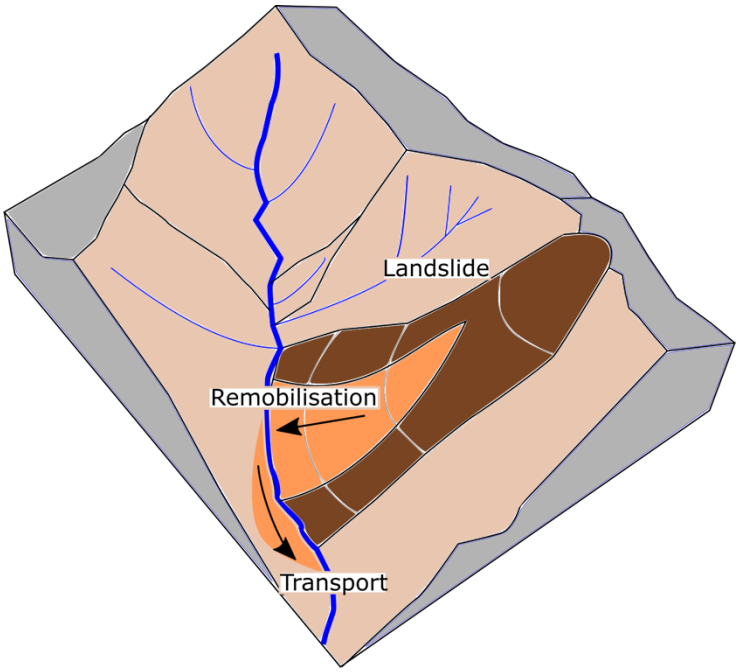

Figure 18. A model catchment with landsliding. The landslide deposit (shown in brown) is reactivated (shown in orange) which erodes the sediment within the deposit and deposits it into the stream network where it can be eroded further. Not all the sediment will be eroded in a single movement so storage must be account for when calculating a full sediment budget.

Sediment budgets are also important for hazard modelling, many sediment production and transport processes can be hazardous to local communities. Understanding the timing and spatial relationships of the processes are the basis of many hazard models. Sediment production is dominated by landsliding in steep catchments (Dunne 1991; Hovius et al. 1997; Bennett et al. 2013; Marc et al. 2019); landsliding in itself is a hazard but the mass increase in sediment produced by a landslide can also create a cascading effect of hazards and sediment transport (Figure 18) (Huang and Fan 2013; Bennett et al. 2014; Zhang et al. 2016). Landslide sediment is loose and easily remobilised during intense rainstorms, producing debris flows on hillslopes and in channels (Lin et al. 2004; Ma et al. 2017). Fine grained sediment can also be mobilised by overland flow by rilling which can alter the ecosystem of downstream habitats and affect water quality (McGuire et al. 2013). Increased sediment transport and deposition in the channel network could enhance the risk of flooding by reducing channel space (Zhang et al. 2016).

Earthquakes produce significant volumes of sediment through coseismic landsliding (Keefer 1994; Malamud et al. 2004b; Marc et al. 2016a). Through empirical relationships between landslide area and volume we can quantify the sediment produced by an earthquake (Hovius et al. 2011; Parker et al. 2011; Li et al. 2014). This estimate of sediment production can be used as the basis of a sediment budget to understand the

erosion of coseismically produced sediment and sediment transport in mountain ranges. The 2008 Wenchuan earthquake is the one of the first earthquakes to occur in the era of freely available high spatial and temporal resolution satellite imagery and offers an excellent opportunity to complete a sediment budget of an earthquake.

Previous studies have provided some estimates of the processes and their potential importance to the sediment budget of the Wenchuan earthquake. However, these have only quantified a part of the budget. Measurements of suspended load (maximum diameter 0.25 mm) have shown an increase in sedimentation rates after the earthquake linked to landslide density in catchments (Wang et al. 2015). Using the grain size of several landslides, Wang et al (2015) estimates that between 10 and 72% (mean 19.3%) of the mass of the finest material (<0.25mm) was evacuated by 2012. These estimates are from a small number of landslide deposits and ignored the largest of grains (boulders) which could severely overestimate the fine proportion of the landslide deposits. The volume and density of the landslide deposits are significant sources of uncertainty while the study also assumes that all sediment can be mobilised by runoff and stream power, an assumption which is unlikely to be true. Bearing these caveats in mind, between 0.66 – 4.7% of the total landslide sediment produced by the earthquake could be transported as suspended sediment. Wang et al (2017) estimated the residence time of slightly coarser sediment (0.25 - 1mm) to be between 4 and 1500 years with an average of 370, suggesting that by 2012 between less than 1% (6 – 0.02%) of the total sediment was removed. Here a model was used to estimate the volume of sediment being removed from the catchments via the change in cosmogenic nuclide concentrations at the outlets of catchments. There are several assumptions made about the composition of the landslides, the concentration of cosmogenic nuclides in the deposits and whether the rates of removal will change through time. These assumptions, while justifiable could mean the removal is significantly slower than estimated. The combination of the Wang et al (2015) and Wang et al (2017) estimates suggest that a maximum of 10.7% (1.33% average) of the total sediment has evacuated the orogen in the first 4 years after the earthquake. Along with only recording the movement of fine sediment, these studies cannot identify any processes responsible for sediment transport.

Using repeated landslide mapping and field campaigns in 16 catchments, Zhang et al (2016) used measurements of debris flow deposit volumes to estimate that 10% of the coseismic sediment had been remobilised and deposited into the Min Jiang by 2013. The study identified the small tributary channels of the Min Jiang as important sediment stores as some channels were alluviated by 10 meters in those five years. Zhang and Zhang

(2017) delved slightly deeper into the sediment budget and demonstrated that sediment transport decreased through time after the earthquake long before the deposits in the catchment was significantly exhausted.

Combining these 4 studies produces an incomplete sediment budget but provide an estimate of up to 20% of the coseismic sediment has been mobilised into the Min Jiang by 2013. While 20% may seem rapid, sediment transport rates decrease through time suggesting that the remaining sediment may remain in the Longmen Shan for 1000s of years (Wang et al. 2015; Wang et al. 2017; Zhang and Zhang 2017).

Constraining the residence time and transport mechanisms of landslide sediment in mountain ranges is key to understanding how mountain ranges contribute to global sediment and carbon budgets (Larsen et al. 2014; Hilton and West 2020), how mountain ranges grow and erode (Hovius et al. 2011; Densmore et al. 2012) and how landscapes react to significant perturbations. If sediment remains in a mountain range for 100s or 1000s of years our recording of extreme events from stratigraphy is likely to underestimate their importance and frequency due to signal shredding (Jerolmack and Paola 2010). Landslide deposits provide fresh material for weathering which can release or drawdown carbon and can potentially have a significant effect on climate change (Hilton and West 2020). These deposits also alter the concentration of cosmogenic nuclides in the river system, potentially changing how erosion rates are recorded (Niemi et al. 2005; Yanites et al. 2009; Dingle et al. 2018). If the sediment is stored on hillslopes it is possible they can be recycled raising questions on how sediment is produced and eroded in mountain ranges. Landslide sediment, and their transport processes also significantly increase the likelihood of natural hazards altering the living conditions of mountain communities significantly, potentially for generations (Fan et al. 2019b). Therefore, in depth study of the sediment transport dynamics after an earthquake is required.

3.1.3 **Research questions**

In this chapter I look to answer the following research questions:

1) How are landslide deposits transported around and out of catchments after the Wenchuan earthquake?
2) How do the remobilising processes change through time?
3) What are the timescales of coseismic landslide deposit erosion after the earthquake?

3.2 Methodology

3.2.1 The sediment budget of an earthquake

All sediment generated by an earthquake starts on the hillslope, either as bedrock, soil, or regolith. The hillslope fails by landsliding both during the earthquake and afterwards during rainstorms. Depending on the runout length of the landslide the sediment produced by the earthquake can be deposited either on the hillslope or at its base. If the channels at the bases of the hillslope have the transport capacity, they can begin to rework any sediment deposited directly into them. Landslides on the hillslope or in small tributary channels need to be further reworked by internal or hillslope processes before it can enter into channels and be eroded out of the catchment. Many small catchments also struggle to evacuate sediment on the valley floor due to their low drainage area and discharges. Here sediment can pile up until it is gradually eroded by reoccurring debris flows or floods. Eventually the sediment will enter the major trunk of the orogen draining river and be exported out of the orogen at some rate.

After the Wenchuan earthquake many of the smaller coseismic landslides are disconnected from the channel network, while many that are connected show little evidence of fluvial undercutting. Deposits on the hillslope, termed hillslope deposits, are the first major store of sediment in the Longmen Shan. The second is at the base of the hillslopes in the tributary channels. These are termed as tributary channel deposits (Figure 19). For my sediment budget the end point for the sediment is the Min Jiang as all sediment must pass through the main river trunk before it exits the mountain range.

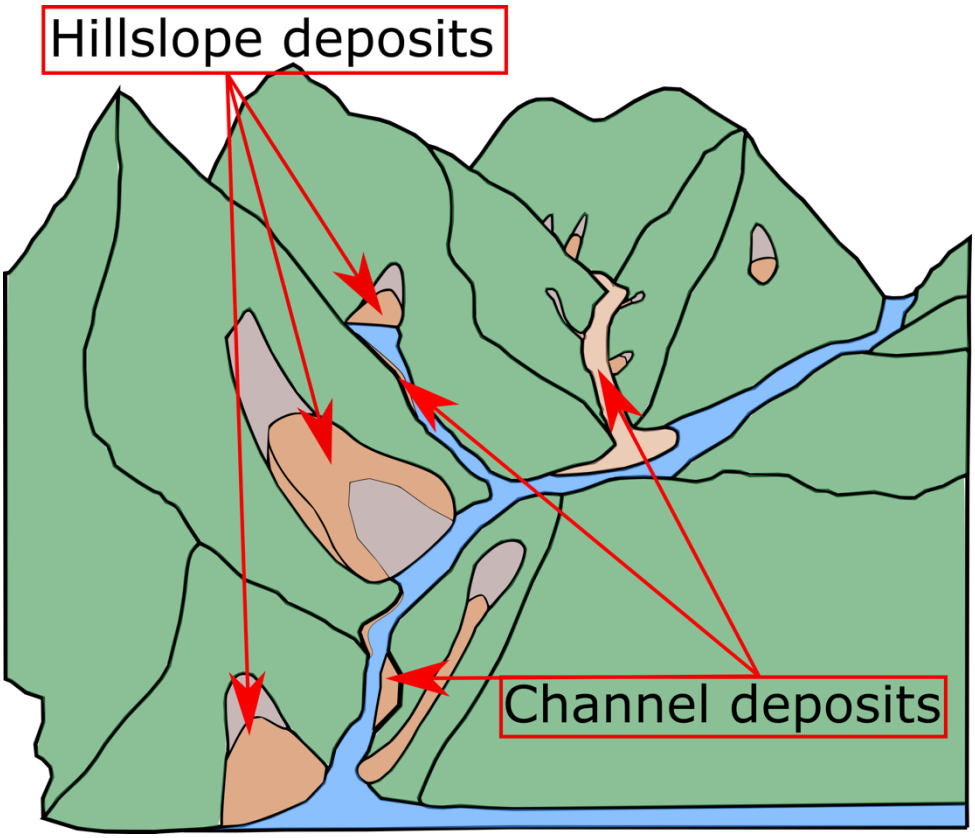

Figure 19 A conceptual cartoon of the main sediment stores after the Wenchuan earthquake. Sediment (orange) is stored either on the hillslope in the form of landslide deposits or in tributary channel deposits before being eroded into the Min Jiang. The sediment can be eroded by processes each with their own recognisable form.

I constrain the sediment budget and the processes linking the sediment stores through a combination of a multitemporal landslide inventory and previously published data for processes which could not be quantified from imagery.

3.2.2 **Constructing the multitemporal landslide inventory**

To construct the sediment budget of the Wenchuan earthquake I used a multitemporal landslide inventory. The inventory I used and discuss throughout this thesis was an adapted version of the inventory discussed in (Fan et al. 2018a) and (Fan et al. 2019c). While these published inventories focus on the areas of the mapped landslides, I focus on their volumes and the processes which erode their deposits. Fan et al (2018) used an activity level to identify where reactivation of coseismic landslides is occurring while I explicitly mapped the reactivation to estimate the change in the deposit volume. I also used these mapped polygons to define the processes by which coseismically produced sediment is transported through and out of catchments. Here I discuss both the creation of the original inventory and my adaption of it.

Landslide inventories are maps of landslides triggered by an event or an in-depth investigation of landsliding over a period of time. They identify areas of the landscape that

are susceptible to landsliding to validate susceptibility models (Guzzetti et al. 2012; Reichenbach et al. 2018). Typically, inventories are either simple points or polygons which mark the deposit or scar of the landslide (Guzzetti et al. 2012). Point inventories are quick to produce and offer a rapid methodology to map a large number of landslides (Gorum et al. 2011; Kargel et al. 2016). While being relatively quick to produce, point inventories only indicate the position of the landslide and offers no information on the area or location of the deposit, which is crucial for understanding the volume of sediment produced and how it is connected to the channel network (Malamud et al. 2004b; Larsen et al. 2010; Williams et al. 2018). Therefore, for sediment budgets, landslide inventories with polygons are required.

Fan et al (2018) mapped the coseismic landslides by identifying the landslides as new white (rather than green vegetation) shapes on the hillslope. They did not distinguish between the scar and deposit of the landslide. In the subsequent images they remapped the catchments to identify any new post seismic landslides and which landslide deposits remain active. Activity was mapped as non-vegetated parts of the coseismic landslide deposits in which a change, typically movement of boulders or formation of levees within the deposit, was observed. This identified activity was then used to identify which deposits stabilise and which reactivate in each time step (Fan et al. 2018a). I used the mapped activity separately from the coseismic landslide deposits to identify first the area and then volume of the reactivated movements.

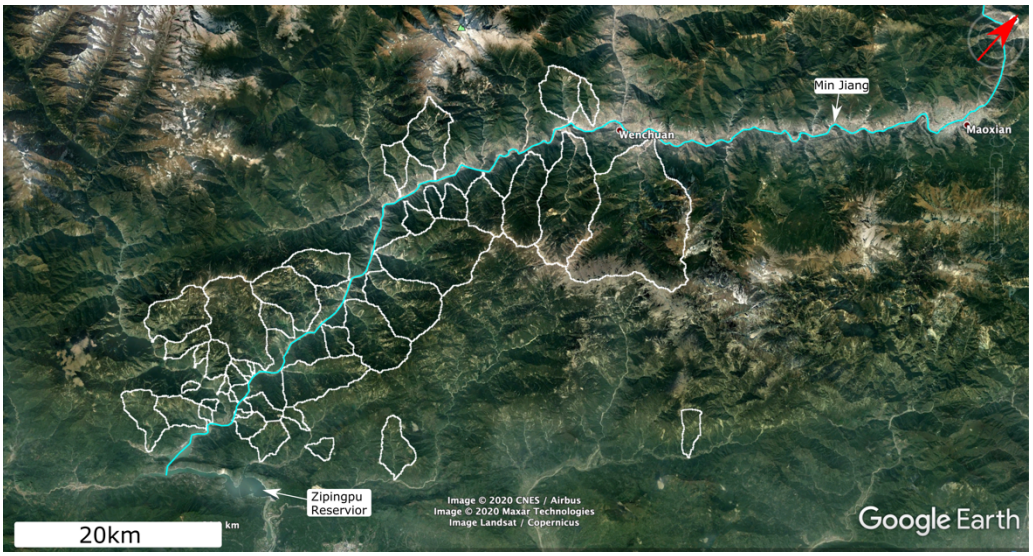

Figure 20 The basins in which landslides were mapped during this study are outlined in white over satellite imagery taken from Google Earth. Most of the basins drain directly into the Min Jiang (highlighted in light blue) between Wenchuan and Yingxiu.

The inventory covers 42 sub-catchments along the Min Jiang between Yingxiu and Wenchuan (Figure 20). This area is close to the surface rupture of the earthquake and as a result has high landslide densities. Due to the wide availability of satellite imagery the inventory covers a 10 year period (2008 – 2018) at 6 different time steps (2008, 2011, 2013, 2015, 2017, 2018), I combined 2017 and 2018 into a single year due to the low (single figures) numbers of new remobilised landslides. The 2008 inventory was mapped exclusively from aerial imagery while the rest use satellite imagery (Table 1). The 2011 Worldview satellite image is orthorectified by Pix4D and used as a base for the rectification of all others to ensure errors are minimal (Williams et al. 2018). No rectification errors between images or inventories were detected during the making of the inventory.

Table 1 The images used in the development of the inventory with their source and resolution. Coverage describes the percentage of the study area covered by the imagery at each time step.

Date of image	Source of Image	Resolution	Coverage
May – July 2008	Aerial photography	1 – 2.5m	97%
April 2011	Aerial photography and Worldview satellite	0.5 – 1m	99%
April 2013	Aerial photography and Pleiades satellite	0.5 -2m	95%
April 2015	Spot 6 satellite	1.5m	99%
April 2017	Spot 6 satellite	3m	93%
April 2018	Spot 6 satellite	3m	93%

The 2008 image was used to map coseismic landslides while the rest were used to record new post-seismic landslides and remobilisation of coseismic deposits. A pre-earthquake image was also used to ensure all landslides recorded in 2008 are coseismic (Figure 21A&B). The landslides were mapped as a single polygon which includes both the deposit and scar to ensure consistency in the mapping. Visual interpretation by trained mappers was chosen as the mapping method as it is more reliable than semi and automatic mapping algorithms (Guzzetti et al. 2012). Algorithmically mapped inventories can require significant data cleaning before they can be used for volume estimation (Li et al. 2014;

Marc and Hovius 2015). Humans are also better at mapping the change in activity of the landslide deposits due to the slight differences of brightness which denotes remobilisation of deposits (Figure 21C). The uncertainty between different mappers needs to be quantified to ensure consistency in the mapping of landslides and their remobilisation.

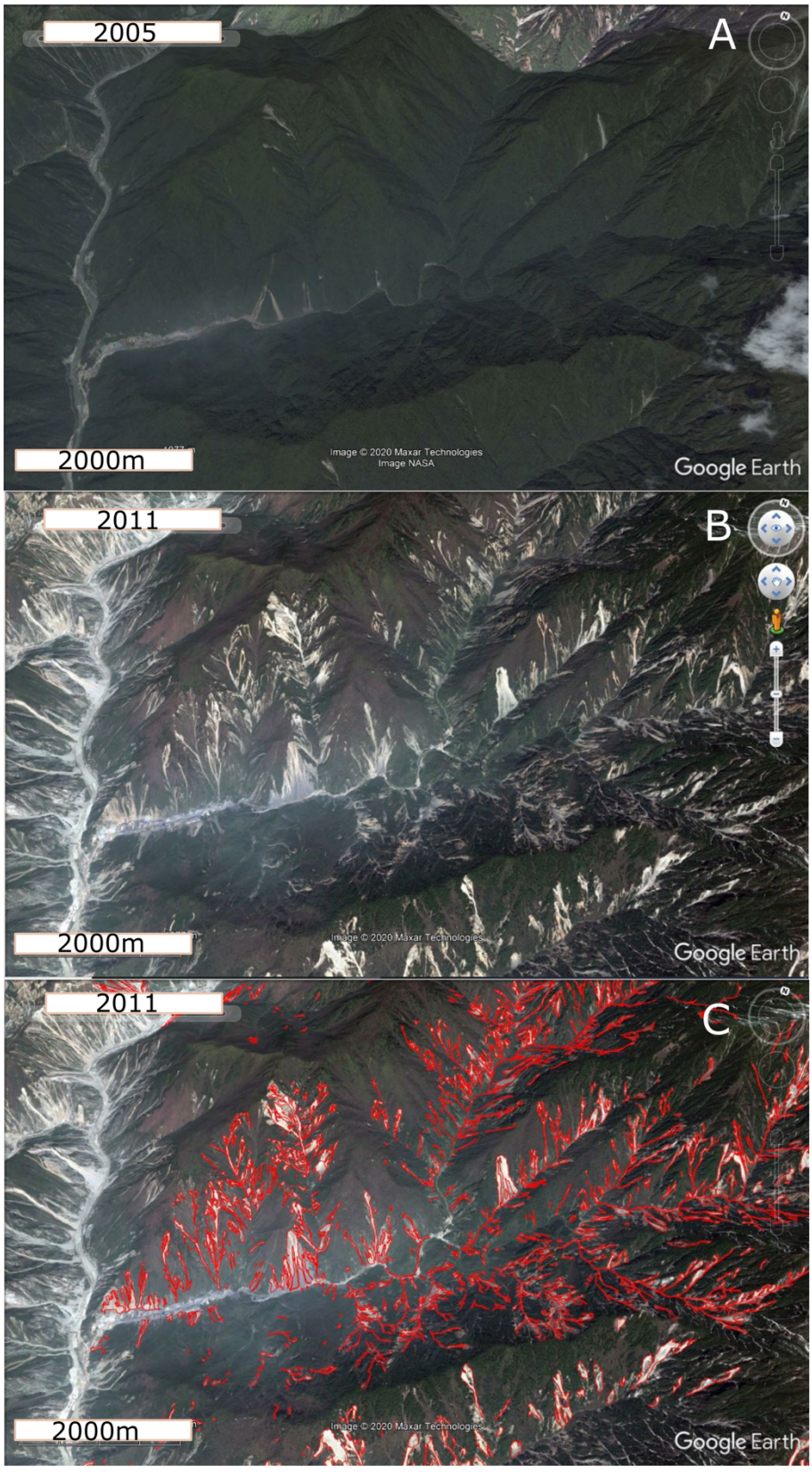

Figure 21 A sample of the inventory displayed on Google Earth imagery. A) A pre-earthquake image used to identify coseismic earthquakes in the 2008 image. B) the 2011 image before mapping. C) The final landslide inventory of 2011 with all mass movements mapped in red.

In the 2008 image 2 types of deposit are mapped, slides and flows. Slides are classic landslides with wide deposits and generally short runouts (Figure 22). They are likely to be

a combination of debris and rock slides and debris and rock falls, though no attempt is made to categorise them further (Hungr et al. 2014). Flows are long thin mass movements with clear flow patterns and are typically identified as debris flows. In the post-earthquake images a further 2 types of movement was recorded. Channelised remobilisations are flows that initiate within landslide deposits. Unchannelised remobilisations are remobilisation with no clear flow like features, these are a combination of shallow landslides and or possible rills with spacings too small to mapped separately (Figure 22).

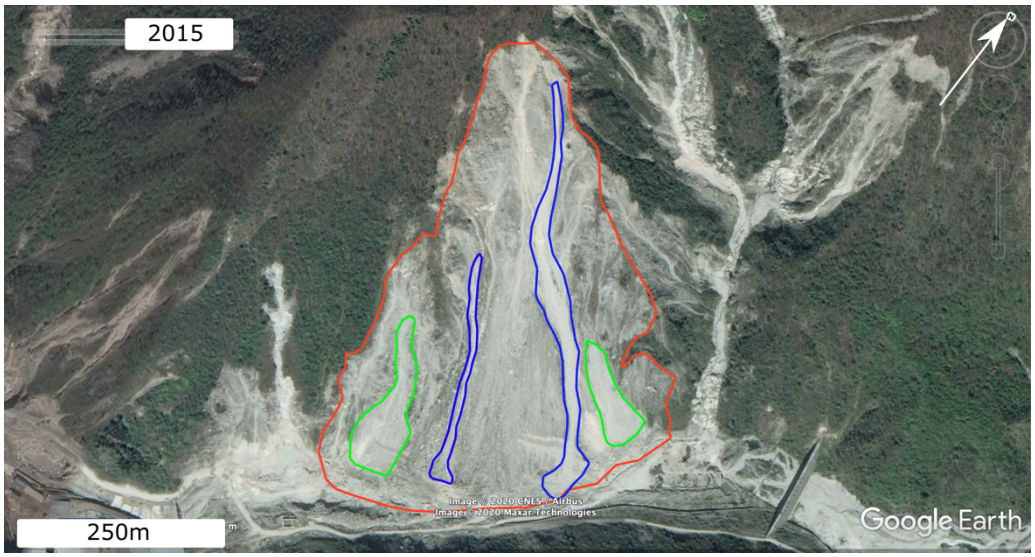

Figure 22 A subsection of a mapped catchment with the key mass movement types highlighted in different colours. Red highlights a coseismic slide which has then been remobilised several types in the years since. Green highlights a unchannelised remobilisation and blue highlights the channelised remobilisation. Sediment mobilised as a flow is mapped in the same way as the channelised remobilisation.

The majority of the mapping was undertaken by a group of masters students based at our project partner university, Chengdu University of Technology. The mapping area was divided between the team of 6 mappers, who remained in contact with each other throughout the exercise to ensure consistency. All mappers were trained on a small sub catchment to further ensure consistent mapping (Figure 23). The training maps of the mappers also allow for a comparative study between the mappers to quantify the uncertainty of the inventory. The uncertainty was estimated in a pair like fashion, comparing one inventory to each other mapper in turn (Galli et al. 2008).

$$M_n = \frac{A_n \cap A_r}{A_r} \qquad \text{Equation 7}$$

The matching degree M_n of a mapper is simply the area of the intersection (overlap) between the 2 mappers divided by the total polygon area of the reference mapper A_r. The individual scores are then averaged to give a total matching score (M) of the mapping.

$$M = \frac{1}{N}\sum_{n=1}^{N} M_n \qquad \text{Equation 8}$$

The average matching score of all inventories is 76% which gives an uncertainty of ± 19% in the area of the landsliding (Figure 23). A mapping score above 70% is deemed accurate and comparable to other studies of inventory similarity (Ardizzone et al. 2002; Galli et al. 2008; Guzzetti et al. 2012).

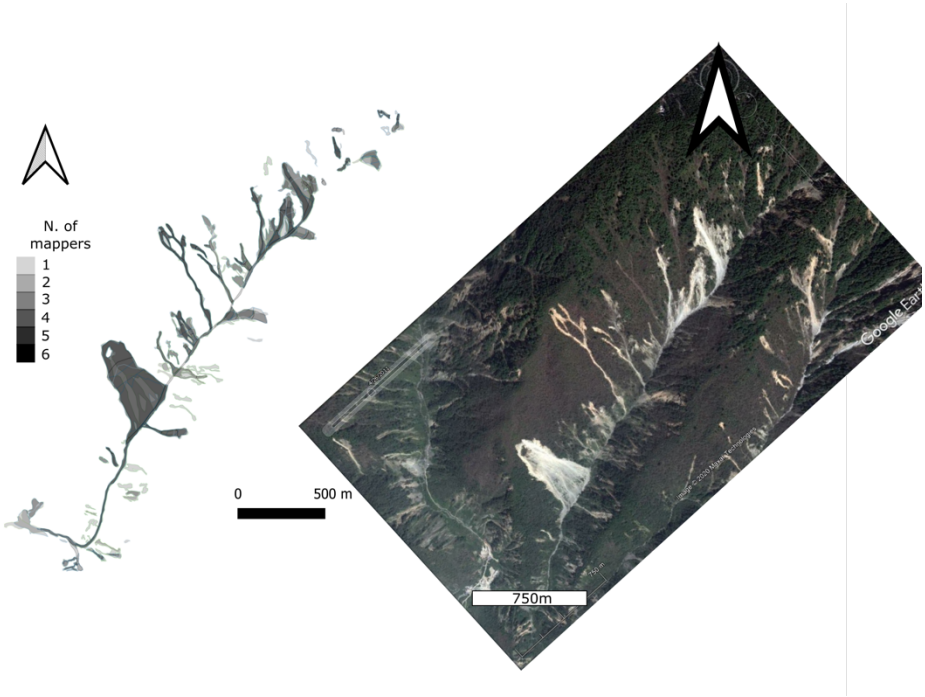

Figure 23 The training basin was mapped by each of the 6 mappers who contributed to the multitemporal inventory. Here they mapped the original landslides rather than the remobisations within them. The landslides or debris flows which are mapped by the most mappers are darker in the map while those which are less frequently mapped are white.

For every image after 2008 all mass movements that occur on the hillslope were recorded, including active movement within coseismic landslide deposits (See appendix figures). The area of the smallest mapped landslide in each time step ranged from 30 – 553m^2, this range is in part due to the increase in resolution (from 0.5 - 6m) but was most likely due to an actual increase in the minimum landslide area (See appendix table 1) (Fan et al. 2018a; Fan et al. 2019c). The mapping of erosion within the deposits is different from previous multitemporal inventories (Tang et al. 2016) including the one presented in Fan et al. 2018 and Fan et al. 2019. These inventories only mapped new post seismic mass movements and estimated the "activity level" of the coseismic landslide deposits. Activity level is a measure of how active the surface of the deposit is; for example if 1/3 of the deposit has clear activity the deposit has an activity level of 1 (Tang et al. 2016) (Figure 24). This

method is useful for quick identification of how and where landslide deposits are stabilising, but it tells us very little about how much sediment is being eroded from the deposits. By recording the area of remobilisation directly I used empirical area – volume scaling relationships to estimate the volume of sediment removed and the volume that remains in the deposits.

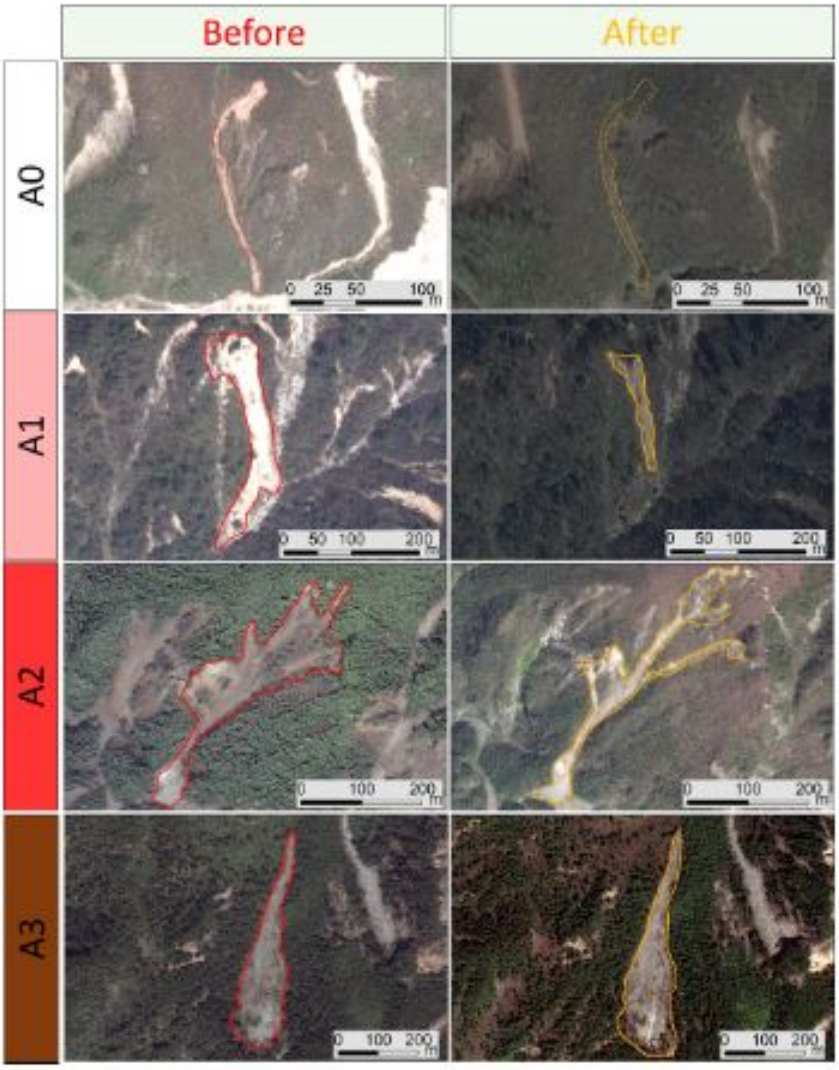

Figure 24 Activity levels with examples , taken from (Fan et al. 2019c). A0 are deposits which have completely revegetated while A3 are fresh deposits, A2 have surfaces which are two thirds active and A1 are one third active.

3.2.3 **Channel deposits**

As demonstrated by Zhang et al. (2016) and Zhang and Zhang (2017) the tributary channels of the Min Jiang can store large volumes of sediment, and therefore the volume stored within them should be estimated. Producing an estimate of the volume of sediment stored in tributary channel deposits separately from the hillslopes and how it may change

through time is also useful as a constraint on the discharge of sediment from the hillslope into the channel.

I mapped the channel deposits of the main valley floor of the 17 largest catchments on Google Earth (Figure 25). These catchments have at least 2 clear post seismic images which I used to monitor how the storage changed through time (

Table 2). All the catchments with mapped channel deposits had significant debris flow events so are active contributors to the Min Jiang. The unmapped catchments are smaller and as a result are less likely to have large storage on their valley floors. Despite this, without mapping all the catchments my estimates will be an underestimation of the sediment stored in the catchments, and possibly the input into the Min Jiang.

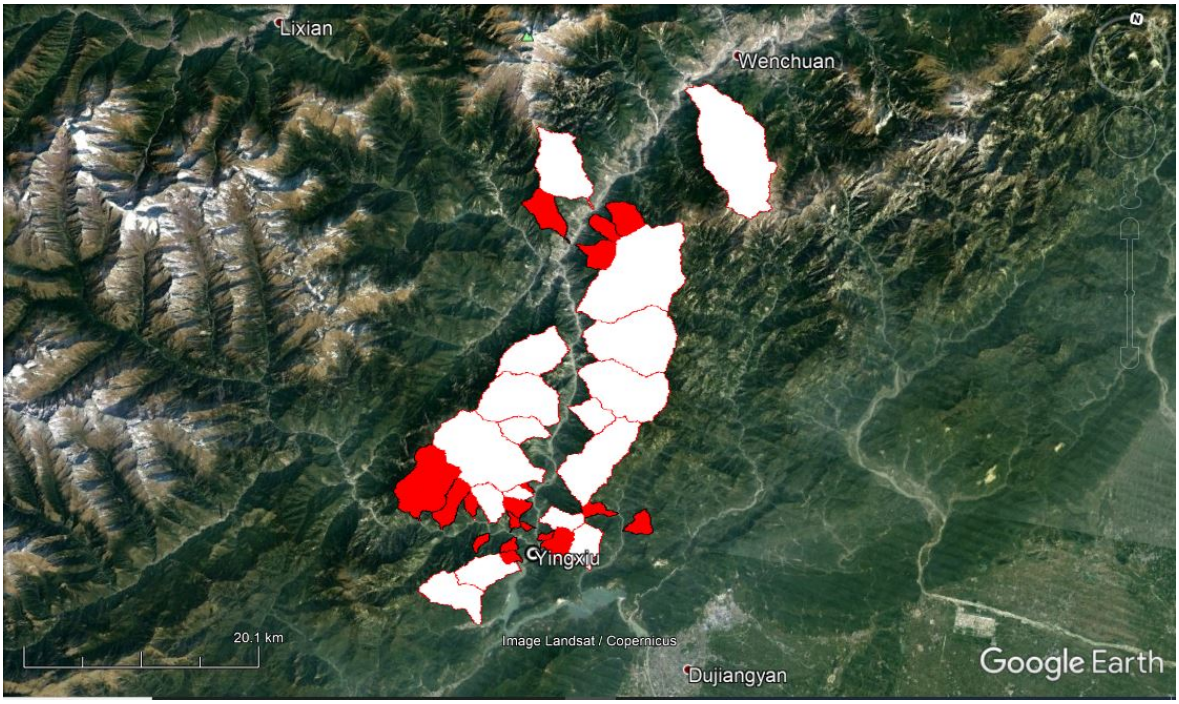

Figure 25 Catchments with measured channel deposits are shown in white while those in red are not mapped.

Table 2 Table of catchments with mapped channel deposits and the years mapped. Red boxes denote a mapped year.

Catchment number	2005	2008	2010	2011	2014	2015	2017	2018
0	■			■		■		
1	■			■		■		■
2			■	■		■	■	
3				■		■	■	
4	■			■		■		■
5			■	■		■		
6						■	■	
7				■	■			
8				■		■	■	■
9			■	■			■	
10		■	■		■			
11				■		■	■	
12			■		■		■	
13				■		■	■	
14	■			■		■		
15	■			■	■			■
16				■	■			■

Rather than map the extensive deposits as polygons I chose to map the deposits as a series of cross sections on the channel floor (Figure 26). These were converted into volumes by assuming a triangular cross section shape and multiplying it by the distance between each cross section. The dip angle of the valleys is varied between 20 and 40º, a typical range of hillslope steepness in the landscape (Figure 27). Channel deposits are on the valley floor and are reworked by fluvial action, hillslope deposits on the other hand are fan shaped and are relatively undisturbed by the channels. To measure the cross-section length, I drew a line from one side of the deposit to the other. This line extends during times of deposition on the valley floor and decreases due to incision and stabilisation via growth of vegetation.

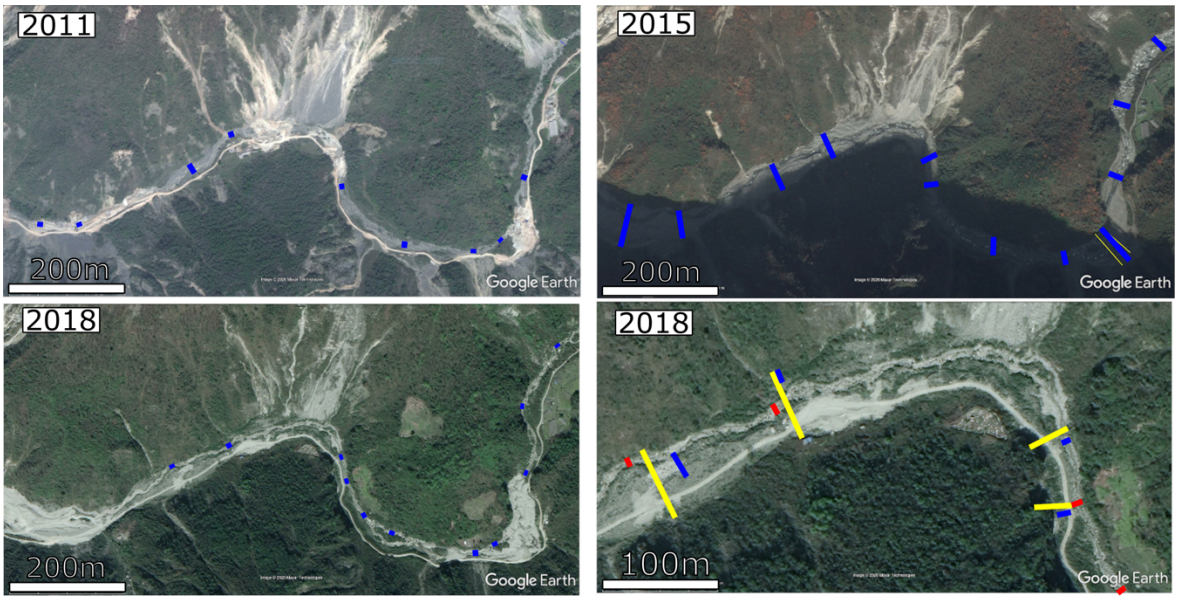

Figure 26 Examples of the channel deposit mapping and how they change through time. The blue lines depict the cross-section length, between 2011 and 2015 there is an increase in the length of the cross sections due to a deposition event while between 2018 and 2015 there is a stabilisation and incision. The final image (bottom right) shows a satellite image in 2018 with the changes in deposit width shown in different colours. Blue 2011, yellow 2015 and red 2018, within Google Earth images can change location through time but I took care to ensure the same location was mapped in each image.

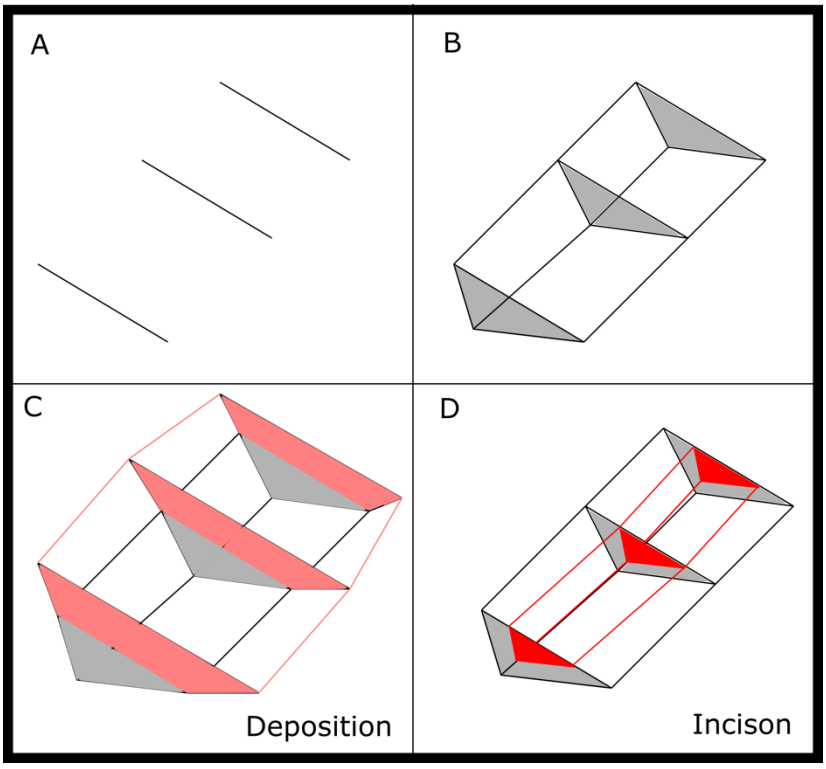

Figure 27 A cartoon illustrating the estimation of channel deposit volumes from cross sectional lines. A) Cross sections are drawn. B) A triangular channel shape is assumed and an under the curve algorithm uses the areas and distances between the cross sections to estimate a volume C) If the next cross sections are longer deposition (pink) is likely to have occurred. D) If a later cross section is smaller incision (again triangular in shape) occurred.

3.2.4 **Estimating the volume of co and post-seismic landsliding**

Mapped landslide areas were converted into volumes using empirical area – volume scaling relationships. The total mapped area of each landslide polygon was converted to a volume by using the equation

$$V = \alpha A^{\gamma} \quad \text{Equation 9}$$

This scaling has been shown to vary with local conditions, mainly soil depth and weathering condition of the bedrock and landsliding mechanism, which adds significant uncertainty to the estimated volumes (Larsen et al. 2010; Koyanagi et al. 2020). Neither landslide inventories nor the satellite imagery upon which they are based on provide much information about the relevant local conditions of the landscape. Therefore, I used a variety of possible coefficients (α and γ) to quantify the uncertainty in landslide volume. I used a relationship produced from 41 measurements of coseismic landslide deposits (and the stated uncertainty) (α = 0.1±0.096, γ = 1.392±0.087) (Parker et al. 2011; Li et al. 2014) and a global shallow soil relationship (α = 0.14±0.005, γ = 1.145±0.008) (Larsen et al. 2010). These relationships gave 2 orders of magnitude difference in volume estimations (Table 3). I assumed the scaling relationships are based upon local conditions and thus use the same constants for both coseismic and new (non-remobilising) post-seismic landslides.

Table 3 Different area – volume scaling relationships for landsliding.

Scaling relationship reference	Co-seismic landslide volume (km^3)	Post-seismic landslide volume (km^3)
Li et al. (2014)	7.45×10^{-1} (- 6.17×10^{-1}/+ 3.765)	3.74×10^{-3} (- 2.87×10^{-3}/+ 1.38×10^{-2})
Larsen et al. (2010) shallow soil landslides	7.71×10^{-2}	7.70×10^{-4}

Equation 9 is only constrained for landslides and a separate but unknown scaling relationship is required to estimate the volume of debris flow deposits. The volume of debris flows is reliant on their initial failure volume and any sediment they are able to entrain along their runout (Iverson et al. 1997; Bovis and Jakob 1999; Wang et al. 2003; Iverson et al. 2011; Schürch et al. 2011; Ouyang et al. 2015; Horton et al. 2019). To

convert the mapped debris flow areas into volumes I tested several relationships and constrain them within the sediment budget using the channel deposit volume estimates.

3.2.5 **Estimating the sediment discharge between the hillslope and tributary channel deposits.**

I used the different time steps of the multitemporal landslide inventory to constrain the volumes of sediment moving during a particular time period. By doing this separately for the hillslope and tributary channel deposits I compared the two estimates and test the area – volume scaling relationships of the mapped mass wasting.

In a particular time step I recognised whether a mass movement deposits sediment from the hillslope into the tributary channel deposit by comparing the drainage area at its lowest point to that of the average channel head. The drainage area of a mass movement is calculated from the ALOS World 30m DEM provided by JAXA (Tadono et al. 2016) using a D-Infinity Contributing Area algorithm within the LSDTopoTools software package (Mudd et al. 2020). The drainage area of the channel heads was estimated from mapping their likely locations in Google Earth from satellite imagery. The lack of a high resolution DEM prevented the use of topographic analysis to automatically map channel heads (Grieve et al. 2016). Despite this, my estimate of the drainage area of channel heads is similar to other studies (Li et al. 2016a). If the mapped polygon of a post seismic mass movement has a drainage area greater than that of the channel heads it was assumed to have deposited sediment into the channel network.

I compared the volumes of the tributary channel deposits with various estimates of discharge from the hillslope to constrain the likely range of volumes entering the channel deposits.

$$V_{cd} = V_{in}(HS) - V_{out}(cd) \qquad \text{Equation 10}$$

Here V_{cd} is estimated sediment volume stored in the tributary channel deposits, $V_{in}(HS)$ is the volume of sediment entering into the channel for a given time period and $V_{out}(cd)$ is the sediment that is removed from the channel deposits. $V_{out}(cd)$ was estimated through the calculation of the volume removed by incision into the channel deposits (Figure 27) with the assumption that all "missing" sediment is removed from the channel into the Min Jiang. With estimates of V_{cd} and $V_{out}(cd)$ I identified likely scaling relationships for the mapped remobilisation polygons. All volumes were divided by the timestep of the inventory to produce a sediment discharge.

3.2.6 **Other processes – literature derived values**

While the major processes generating and remobilising sediment in the Longmen Shan were identified from satellite imagery, some operate on scales smaller than the resolution of satellite imagery and as a result cannot be quantified. The presence of these processes was inferred from a literature review and field observations of sediment mobilisation. These processes included erosion by overland flow (small rills and gullies) (Fusun et al. 2013; McGuire et al. 2013; McGuire et al. 2017a) and preferential erosion of fine-grained sediment from deposits (Zhang and Zhang 2017; Hu et al. 2018). Large catchment clearing debris flows are debris flows which enter directly into the Min Jiang and their deposit volumes are reported much more accurately in the literature than can be estimated from remote sensing (Tang et al. 2011; Tang et al. 2012; Fan et al. 2019c). I used the literature and reports to produce estimates of the volume mobilised by each.

Overland flow was estimated by extrapolating the data recorded by Fusun et al. (2013). Fusun et al. (2013) recorded the removal of fine grained sediment from the surfaces of 5 landslide deposits using sediment traps in 2010 in the epicentral area of the Wenchuan earthquake. They recorded the mass removed from the deposits over the monsoon period. Using a recorded bulk density of 1.54 kg m^{-3} I estimated the lowering of each deposit for a monsoon season. I assumed 50% of the yearly lowering took place in the monsoon and thus doubled it and extrapolated the lowering across the bare active landslide surface to produce a yearly lowering rate.

Suspended sediment load is recorded at gauging sites along the Min Jiang at daily intervals both before and after the earthquake (Wang et al. 2015). An increase in suspended sediment discharge was recognised and assumed to be connected to the input of loose sediment created by coseismic landsliding. Wang et al (2015) used Chinese Bureau of Hydrology records of suspended sediment concentration and discharge to estimate an increase of 92.5 ±9.3 Mt traveling downstream of 2.7km^3 of coseismic sediment between 2008 and 2012. I assumed the increase in suspended sediment load was related to the volume of sediment upstream of it and used this relationship (Mt/km^3) to estimate how much suspended sediment had been removed from my mapped landslide polygons. While the rate of suspended sediment transport decreases through time (Wang et al. 2015; Wang et al. 2017) I kept it constant as the controls of the suspended load are not clear, therefore my estimate is likely to be an over estimation.

Catchment clearing debris flows are those that are recorded as depositing sediment directly into the Min Jiang. Due to their large size they are well documented case studies with

field-based recordings of volume. The impact of these events can be identified from satellite imagery, but their volumes cannot as their deposits are rapidly eroded and altered by the Min Jiang. Instead I used the compilation of debris flow volumes produced by Fan et al. (2019) to estimate the volume of sediment deposited into the Min Jiang by these events. Fan et al (2019) collected estimates of debris flow deposit volumes from a review of the literature and surveyor reports. All estimates of deposit volume in the compilation where made after rapid field visits after the event took place. As no uncertainty levels are supplied with the volume records, I simply used ± 50% of the recorded volume.

3.2.7 **Constructing the sediment budget**

I identified 2 stores of sediment and 6 processes which remobilise sediment from one store into another (Figure 28). Here I will discuss how I have conceptualised the linkages between the stores and how sediment is evacuated into the Min Jiang.

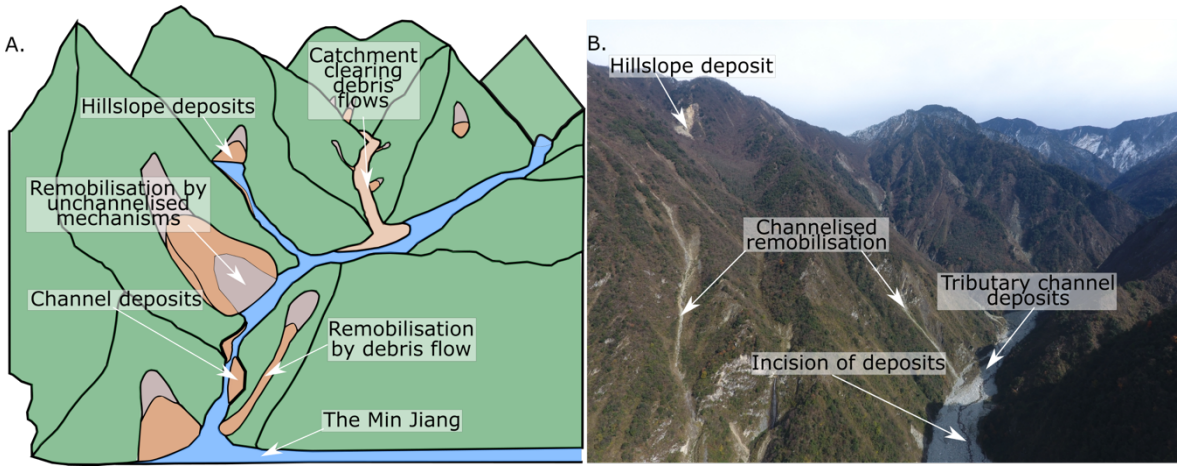

Figure 28 A.) A conceptual diagram of the key stores and sediment transport processes identified after the earthquake. B) A drone image of a catchment in the epicentral area of the earthquake with the key stores and some of the erosion highlighted.

Hillslope deposits are all landslide deposits (including those connected to the channel) and debris flow deposits which do not deposit on the channel floor. Landslide deposits remained relatively untouched by tributary channels but can be mobilised by hillslope processes suggesting they remain in the hillslope domain. Landslide which deposited into the Min Jiang were not counted as hillslope deposits, rather their volume is directly added to the Min Jiang as it is assumed the river rapidly eroded the sediment away.

Tributary channel deposits are made up of debris flow deposits and remobilised landslide deposits. Any mapped remobilisation of a landslide deposit with a drainage area greater than the channel head threshold is added directly to the channel deposit store. The stream order of the channels was calculated via the Strahler methodology and the Min Jiang was identified as a 5th order channel. Any coseismic landslide or remobilisation with a

maximum drainage area greater than that of the 5th order channel was added directly into the Min Jiang.

Erosion by overland flow occurs on hillslope deposits and transports its load into the tributary channel deposits. Suspended sediment transport and incision mobilises fine sediment within the channel deposits into the Min Jiang. Catchment clearing debris flows mobilise both hillslope and channel deposits and thus I assumed equal volumes of the deposit volume originated in the hillslope and channel deposits.

3.3 Results

3.3.1 **Volume of remobilising processes**

Through the methodology described above I have estimated the volume of sediment stored in hillslope and channel deposits. I have also calculated the area of the polygons which signify the movement of sediment from the hillslope into the channel. To estimate the volume of the remobilising processes from their polygons I tested several different relationships and identified which are possible by comparing their total volume to the channel deposits (Table 4). I used a combination of the relationships in Li et al. (2014) and Larsen et al. (2010) and an average depth between 1 and 3m to estimate the volume of sediment being transported by unchannelised remobilisations and debris flows, including channelised remobilisations, into the channel deposits. If the total volume estimated to enter the channel deposits by a particular scaling is greater than the range of volumes recorded in the channel deposits it is discarded. This analysis suggests that the debris flows, unchannelised and channelised remobilisations are likely to be thin and their volumes can be estimated with either an average depth (<3m) or the soil landslide scaling relationship from Larsen et al. (2010). From these I estimate unchannelised remobilisations account for 7×10^{-3} - 2×10^{-2} km^3 of the sediment deposited into the channel deposits. Channelised remobilisations account for 1-3×10^{-2} km^3, the range of values is the difference between the volumes of the Larsen et al. (2010) scaling and a 3m average erosion depth.

Table 4 Comparison of different combinations area – volume scaling relationships for mapped polygons entering the channel network (V_{in}(HS)) and the mapped channel deposits (V_{cd}). The different relationships used for unchannelised and channelised remobilisations are noted in the column headings. Any combinations which are outside the range of the channel deposits are marked with a red cross. All others are marked with a green tick.

		Li et al. (2014)	Larsen et al. (2010)	Larsen et al. (2010), 1m	Larsen et al. (2010), 2m	Larsen et al. (2010), 3m	2m, Larsen et al. (2010)
	V_{in}(HS) (km^3)	2×10^{-1}	2×10^{-2}	2×10^{-2}	4×10^{-2}	5×10^{-2}	4×10^{-2}
V_{cd} (km^3)	$2\text{-}5\times10^{-2}$	✗	✓	✓	✓	✗	✓

3.3.2 **The full budget**

A total area of 0.12 km^2 of coseismic landslide and debris flow polygons were mapped in the 2008 imagery. Using the Li et al. (2014) area – volume scaling relationship I estimate the total volume of the coseismic landslide deposits in the mapping area to be $1 – 7\times10^{-1}$ km^3. Of that between 5×10^{-3} and 3×10^{-2} km^3 was deposited directly into the Min Jiang.

Between 2008 and 2018, $2 - 5\times10^{-2}$ km^3 of sediment is stored in the tributary channel deposits. With the volumes of the major stores, mapped remobilisations and literature derived processes I can compile the sediment budget (Figure 29).

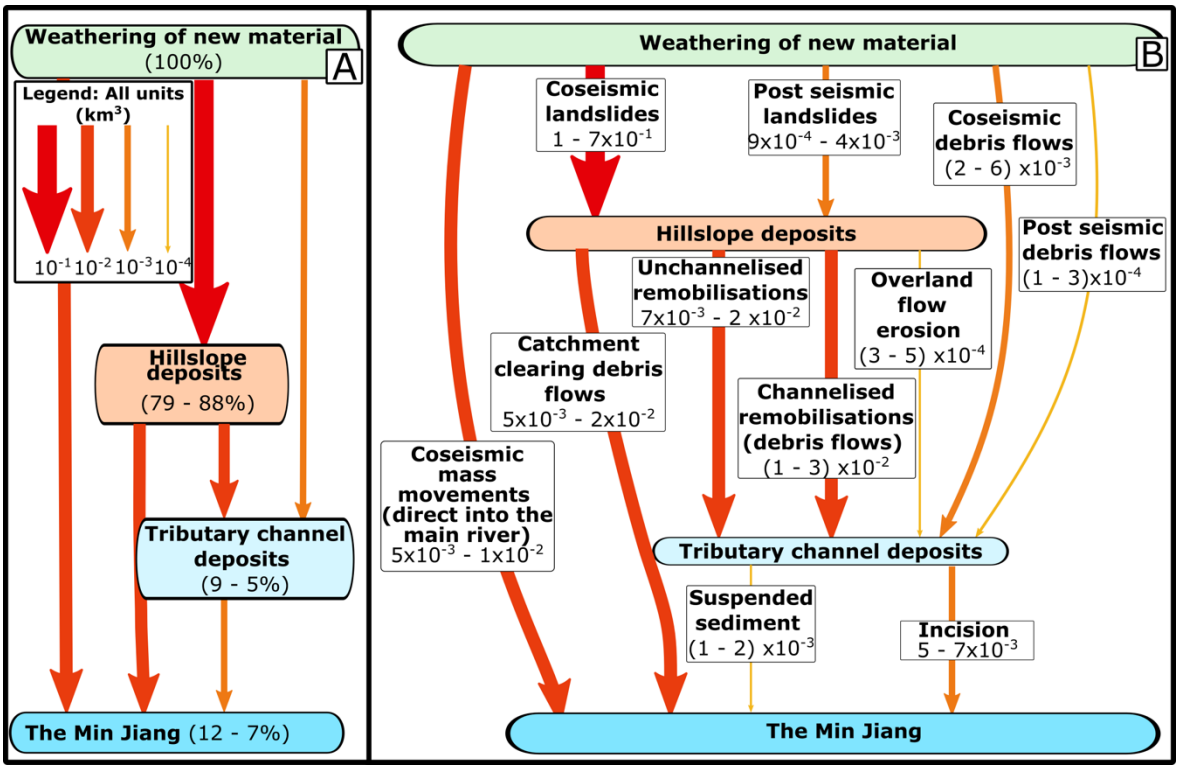

Figure 29 The complete sediment budget of the 2008 Wenchuan earthquake. A) A flow chart indicating the stores of sediment with the percentage of the total volume of sediment mapped in each bin. All sediment is formed on the hillslope and resides in a combination of the stores before being eroded into the Min Jiang river. The arrows are scaled and coloured to show the magnitude of the discharges between each store. B) The sediment budget but focusing on the volume of sediment mobilised and the processes driving the movement of sediment rather than the storage. Each arrow is scaled and coloured to the magnitude of the volume moved; this is the same scheme as on A. The processed move sediment from any store they are connected to and deposit it into the lowest store at their end. The range in each box represents the constrained minimum and maximum value for each process or store based upon the scaling relationships and uncertainty in each process.

The sediment budget is dominated by coseismic landsliding, accounting for approximately 94% of the total sediment production, with post seismic landslides and debris flows accounting for the other 6% (Table 5). Of this sediment, the majority (79 – 88%) remains on the hillslope with the remainder in tributary channel deposits (9 – 5%) and the Min Jiang (13 – 7%). Of the sediment that is remobilised between 54 and 58% is mobilised by debris flows (catchment clearing debris flows and channelised remobilisations). Debris flows are clearly the single most important process in mobilising sediment from the hillslope into the channel network. Catchment clearing debris flows also contribute the largest volumes of sediment into the Min Jiang (5×10^{-3} – 2×10^{-2} km^3) which is between 28 and 32% of the total volume entering the Min Jiang by 2018. Unchannelised remobilisation is the second largest contributor to remobilising sediment while incision into tributrary channel deposits is third. The processes that primarily erode fine sediment (overland flow

and suspended sediment load) account for less than 1% of sediment mobilised during my study period.

Table 5 The sediment budget in table form. All values are rounded to 1 significant figure. The percentages refer to all of the sediment produced, both coseismic and post seismic.

Coseismic sediment budget	**Min (km^3)**	**Max (km^3)**	**Min %**	**Max %**
Coseismic hillslope deposits	1×10^{-1}	7×10^{-1}	94	94
Coseismic debris flows	2×10^{-3}	6×10^{-3}	2	1
Coseismic mass movements deposited into the Min Jiang	5×10^{-3}	3×10^{-2}	4	4
Post-seismic new landslides and debris flows				
Post seismic landslides	9×10^{-4}	4×10^{-3}	1	1
Post seismic debris flows	1×10^{-4}	3×10^{-4}	~0	~0
Total sediment generated	1×10^{-1}	8×10^{-1}	100	100
Remobilisation of hillslope deposits				
Channelised remobilisation	1×10^{-2}	3×10^{-2}	8	4
Unchannelised remobilisation	7×10^{-3}	2×10^{-2}	5	3
Overland flow erosion	3×10^{-4}	5×10^{-4}	~0	~0
Remobilisation of channel deposits				
Catchment clearing debris flows	5×10^{-3}	2×10^{-2}	4	2
Suspended sediment	1×10^{-3}	2×10^{-3}	1	~0
Incision	5×10^{-3}	7×10^{-3}	4	1
Stores				
Hillslope deposits	1×10^{-1}	7×10^{-1}	79	88
Tributary channel deposits	1×10^{-2}	4×10^{-2}	9	5
Min Jiang	2×10^{-2}	6×10^{-2}	13	7

3.3.3 **The sediment budget through time**

Separating the budget into 3 time steps (2008-2011, 2011-2015, 2015-2018) reveals the transient nature of the remobilisation (Figure 30). After the earthquake, 59% of the sediment remobilised by all processes occurred by 2011 and 93 – 95% by 2015. The remobilisation of hillslope deposits is also transient with 64 – 66% occurring by 2011 and 89 – 91% occurring by 2015. This transience is primarily driven by the rapid reduction in debris flow activity: after 2015 there is no catchment clearing activity and a large reduction (by 2 orders of magnitude) in channelised remobilisations. By 2018 the channel deposits were eroding at a greater rate than the hillslopes shown as an increase in the incision into the channel deposits.

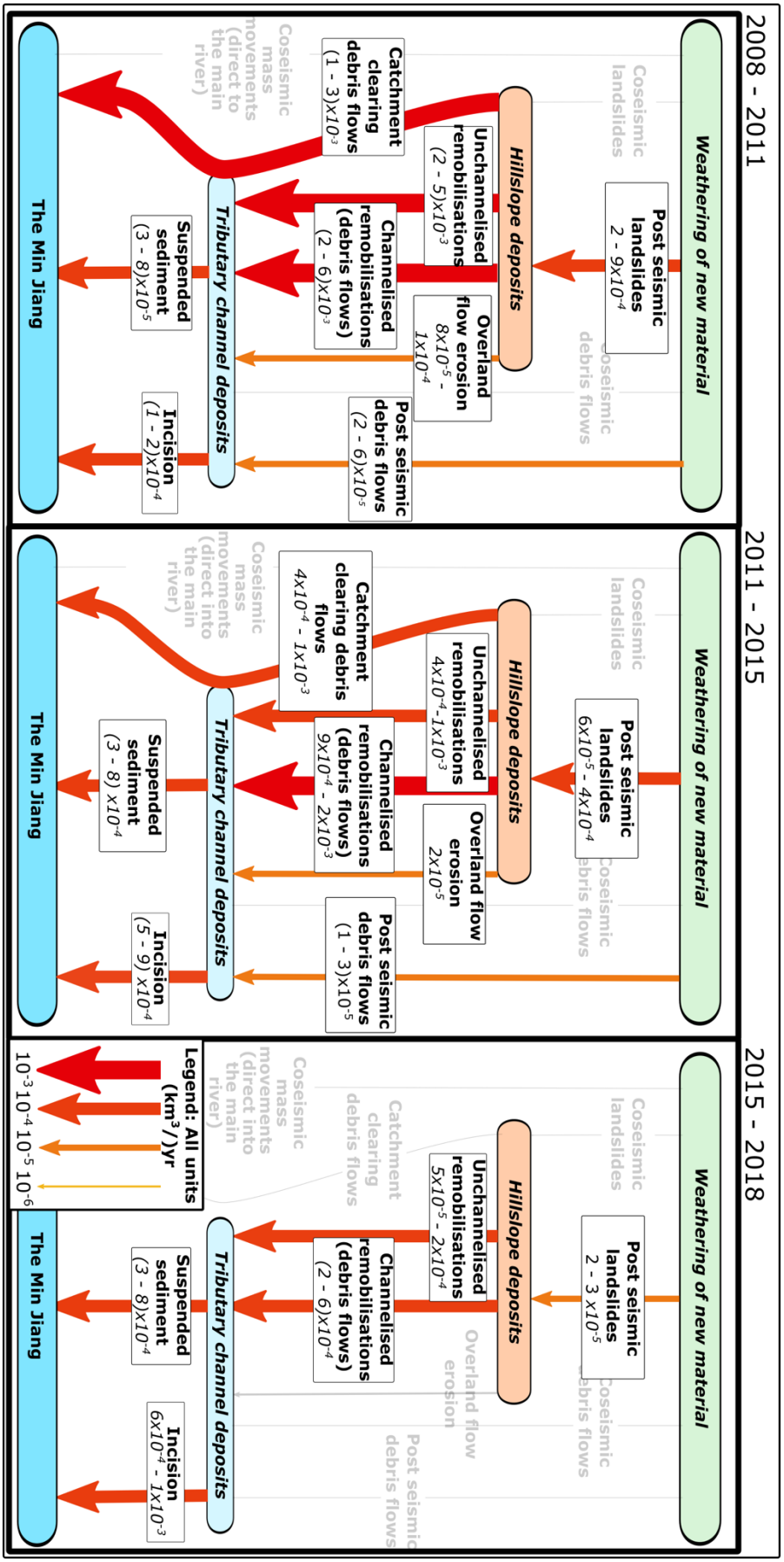

Figure 30 The sediment budget separated into 3 timesteps. The values here are discharges with units of Km^3/year, averaged across the time step.

Table 6 The sediment budget through time in table form. All figures are in km^3/year

km^3/year	2011		2015		2018	
Post-seismic new landslides and debris flows	Min	Max	Min	Max	Min	Max
Post seismic landslides	2×10^{-4}	9×10^{-4}	6×10^{-5}	4×10^{-4}	2×10^{-5}	3×10^{-5}
Post seismic debris flows	2×10^{-5}	6×10^{-5}	1×10^{-5}	3×10^{-5}	~0	1×10^{-5}
Total sediment generated	2×10^{-4}	4×10^{-3}	7×10^{-5}	1×10^{-3}	2×10^{-5}	4×10^{-4}
Remobilisation of hillslope deposits						
Channelised remobilisation	2×10^{-3}	6×10^{-3}	9×10^{-4}	2×10^{-3}	2×10^{-4}	6×10^{-4}
Unchannelised remobilisation	2×10^{-3}	5×10^{-3}	4×10^{-4}	1×10^{-3}	5×10^{-5}	2×10^{-4}
Overland Flow erosion	8×10^{-5}	1×10^{-4}	2×10^{-5}	2×10^{-5}	~0	~0
Remobilisation of Channel deposits						
Catchment clearing debris flows	1×10^{-3}	3×10^{-3}	4×10^{-4}	1×10^{-3}	0	0
Suspended sediment	3×10^{-5}	8×10^{-5}	3×10^{-5}	8×10^{-5}	3×10^{-5}	8×10^{-5}
Incision	1×10^{-4}	2×10^{-4}	5×10^{-4}	9×10^{-4}	6×10^{-4}	1×10^{-3}
Stores						
Hillslope Deposits	-4×10^{-3}	-9×10^{-3}	-1×10^{-3}	-3×10^{-3}	-2×10^{-4}	-3×10^{-4}
Tributary Channel Deposits	3×10^{-3}	1×10^{-2}	6×10^{-4}	2×10^{-3}	-4×10^{-4}	-4×10^{-4}
Min Jiang	1×10^{-3}	3×10^{-3}	9×10^{-4}	2×10^{-3}	6×10^{-4}	1×10^{-3}

3.4 Discussion

3.4.1 The fate of sediment after the 2008 Wenchuan earthquake

The sediment budget clearly shows that most of sediment produced by the earthquake remains on the hillslope or in channel deposits in the low order tributaries of the Min Jiang. This result is similar to that found after the 1999 Chi-Chi earthquake (Yanites et al. 2010; Hovius et al. 2011) and the 1929 Murchinson earthquake (Pearce and Watson 1986). My results are also similar to those found in previous studies of the Wenchuan earthquake which found an estimated 20% of the coseismic sediment was mobilised into Min Jiang during the first 5 years after the earthquake (Wang et al. 2015; Wang et al. 2017; Zhang and Zhang 2017).

Erosion of the hillslope deposits is primarily by channelised processes, typically debris flows rather than further landsliding (unchannelised remobilisation) (Figure 29). Channelised remobilisations erode more sediment than unchannelised highlighting debris flows as a key process in post-earthquake landscapes. The long runout of channelised remobilisations from hillslope deposits can enable any deposit to contribute sediment into the channel network. As any hillslope deposit can contribute sediment into the channel, connectivity is not likely to be a good indicator of how sediment fluxes may be affected by an earthquake (Li et al. 2016a; Tolorza et al. 2019). Where and how landslides are remobilised by debris flows will be looked at in more detail in chapter 4. Field observations and inspection of satellite imagery revealed little evidence of fluvial undercutting of landslide deposits. Due to the lack of this type of erosion I did not include it in the sediment budget. Erosion by overland flow is minimal demonstrating the erosive power of the largest events over smaller more frequent processes (Table 5). Overland flow erosion is also heavily controlled by the availability of unvegetated deposits so the decrease through time highlights the rapid recolonisation of the surfaces of landslide deposits by vegetation (Shen et al. 2020; Yunus et al. 2020). Post-seismic landsliding, despite likely being enhanced by the earthquake, was a minor contributor to the total sediment budget. This result agrees with the work of others that the remobilisation of coseismic landslide deposits is a key component of post-earthquake hazard and risk assessments (Ma et al. 2017; Dahlquist and West 2019).

After the Wenchuan earthquake debris flows are the major way by which sediment is eroded out of catchments rather than fluvial processes. Catchment clearing debris flows account for between 46 – 62% of the sediment deposited into the Min Jiang after the earthquake: incision accounts for 29 - 46%. Debris flows are therefore likely, considering incision also includes debris flow activity, to be the most significant process for depositing sediment into the Min Jiang after the earthquake. The build up of large channel deposits in many of the tributary channels suggests that the input of sediment from the hillslopes is more than can be rapidly removed from the channels. If the channel deposits remain in the landscape for extended periods of time it is possible the frequency of debris flows could limit the removal of sediment from catchments in the Longmen Shan.

3.4.2 **The budget through time 2008 – 2018**

The post-earthquake sediment discharges follow an almost exponential decrease (Figure 30) in my study period suggesting they rapidly return to a (unknown) pre-earthquake rate. As the background rate for most of the processes, other than for suspended sediment, is unknown it is unclear whether the response to the earthquake is continuing. The rapid

decrease found in this study in post-earthquake sediment fluxes however is very similar to results from other earthquakes (Hovius et al. 2011) and from other studies of the Wenchuan earthquake (Zhang and Zhang 2017).

The decrease in sediment discharge is most clearly seen in the reduction of sediment moving from the hillslope into channel deposits. A reduction in the rate at which material is removed from the hillslope is due to a stabilisation of the hillslope deposits, similar to that seen in studies investigating the enhanced post seismic landsliding rates (Marc et al. 2015). There are several theories to explain the stabilisation of the landslide deposits including; increasing cohesion due to vegetation growth (Shen et al. 2020; Yunus et al. 2020) and hydrological changes resulting from preferential removal of fine grained material from the deposits (Zhang and Zhang 2017; Hu et al. 2018). I discuss the stabilisation of hillslope deposits in depth in chapter 4. Throughout the 10 years after the earthquake I surveyed, the rate at which new sediment was generated by landsliding was always lower than the discharge of sediment related to the remobilisation of coseismic landslides. As the discharge of sediment from coseismic landslides remains higher than the surrounding landscape it is likely sediment discharges are still higher than the long-term average.

As I have not measured the discharge of suspended sediment in my study area, I used previously published reports, I assumed the discharge remains constant. However the suspended sediment discharge actually decreases through time returning to its pre-earthquake rate by 2013 (Wang et al. 2015; Wang et al. 2017), a similar time to that of the peak of hillslope – channel remobilisation activity. This could suggest that the suspended sediment flux is closely linked to the rate of sediment being deposited into the channel network, highlighting a supply limited system as seen in the Himalayas (Andermann et al. 2012; Wang et al. 2015; Zhang et al. 2019). Equally it could also suggest that the stabilisation of landslide deposits could be a result of the easily mobilised fine sediment being removed from the hillslope deposits. Whether the stabilisation of hillslope deposits drives the reduction in suspended sediment load in river or vice versa is unclear.

The rate at which material was deposited into the Min Jiang decreased by a factor of 3 between 2011 and 2018. This decline was mainly driven by the decrease of channel clearing debris flows from 2013 (Fan et al. 2019c) onwards but is mitigated by the increase in measured incision through time. The decrease in channel clearing debris flows could be linked to the material properties of the coseismic material (preferential erosion of fine material) (Zhang et al. 2014b; Zhang and Zhang 2017), removal of landslide dams by previous events (Cui et al. 2013) or exhaustion of accessible sediment. The increase in the

incision of the channel deposits is likely due to the decrease in the frequency of widespread deposition events. Without deposition into the channels, the fluvial system will be able to rework the sediment within it rather than the new sediment. Deposition would also obscure the evidence of incision of the channel deposits preventing them from being recorded in the budget. If the channel must continually adjust to large inputs of sediment very little incision into the existing deposits can occur. Incision is the result of the channel and debris flows passing through the channel network and entraining sediment. As long as the channels are steep enough and there is sediment within the channels debris flows are likely to occur (Lin et al. 2004; Zhang and Zhang 2017; Tang et al. 2019). These flows would not be tracked in my inventories, but signs of their activity would be.

3.4.3 **Residence of coseismic landslide material**

Two to three times more sediment ($2– 6\times10^{-2}$ km^3) is removed from the hillslope than the channel deposits ($9\times10^{-3} – 2\times10^{-2}$ km^3) indicating a disequilibrium exists between the sediment discharge of the hillslope and the channel. The timescale at which this disequilibrium lasts for depends on the long term transport capacity of the channel system. As the catchments are small and the streams that exit them are seemingly incapable of moving all but the smallest of grain sizes: it is likely the sediment will remain in the landscape for an extended period of time. Equally the transport length of the average mass movement is similar to or less than the length of the hillslope indicating most sediment will need to be remobilised multiple times before it can be evacuated from a catchment.

On long timescales the sediment deposited into the channels by landslides can enhance incision rates by increasing abrasion or it can armour the bedrock bed preventing incision (Yanites et al. 2010; Egholm et al. 2013). If the sediment from the Wenchuan earthquake remains in the channels for an extended period, the channels will be prevented from incising in response to the uplift from earthquakes. As much of the sediment remains on the hillslopes there is a possibility it could be recycled by landsliding caused by future earthquakes and affect how erosion rates are recorded, an idea that I will explore in chapter 5.

Our current understanding of the erosion and stabilisation of landslide deposits does not allow us to estimate the complete residence time of the coseismic sediment produced by the Wenchuan earthquake. Understanding the magnitude and frequency relationship of debris flows is vital to constraining the residence time, particularly if they continue to be the most significant sediment transport process in the Longmen Shan. The sediment discharges I have measured and their decline through time suggest residence times of 100s

– 1000s of years is not unlikely, a time period similar to the recurrence of earthquakes in the Longmen Shan.

Chapter 4 Reactivation and stabilisation of landslide deposits

4.1 Introduction

4.1.1 Context

The enhanced sediment fluxes that occur after an earthquake are short lived (Dadson et al. 2003; Hovius et al. 2011; Wang et al. 2015). This pattern of large increases in flux followed by rapid return to background levels is seen after many earthquakes and at several different scales (Hovius et al. 2011; Wang et al. 2015). In chapter 3, I showed that debris flows are a key process by which coseismic landslide sediment is remobilised into the channel network after the Wenchuan earthquake. The frequency of debris flows decreases through time, despite 85 - 92% of the coseismic sediment (not including post seismic landsliding) remaining on the hillslope in 2018. The large volumes of sediment remaining on the hillslopes suggests that rather than exhaustion, the reduction of the frequency of debris flows is due to the stabilisation of hillslope deposits or the lack of available sediment for triggering debris flows. Understanding why the frequency of debris flows decrease through time is important for hazard modelling and the mobilisation of coseismic sediment within and out of catchments.

4.1.2 Research questions

In this chapter I address the following research questions:

1) What are the patterns of remobilisation of coseismic landslide deposits and how do these change through time?
2) What are the mechanisms driving post-earthquake landslide and debris flow triggering and how well do current slope stability models explain them?

4.2 Methods

4.2.1 Spatial and temporal distribution of debris flow triggering

Debris flows that trigger within coseismic landslides can be identified from the multi-temporal landslide inventory discussed in chapter 3. For this analysis I only focused on the coseismic landslide polygons and the channelised remobilisations within them. Rather than the landscape-based analysis of the previous chapter, here I focus on individual landslide deposits and the intersecting post-seismic inventories. To analyse the influence of topography on the stability and remobilisation of coseismic landslides I calculated minimum and maximum values of drainage area, elevation, and slope to identify the topographic location of the landslide polygon. For this analysis I used the JAXA ALOS

30m DEM as described in chapter 3. In all results the drainage area quoted is the maximum drainage area, the likely location of the deposit.

Along with the topographic factors I also investigated whether the volume of the landslide has an impact on its stability. I ranked the landslide polygons by volume and separated them into equal quintiles. The first quintile has the 62 largest deposits in it while the last contains the 7323 smallest. By comparing the frequency and magnitude of debris flows occurring in each quintile through time I determined whether deposit size is a factor in the stability of a deposit. This analysis was not process based, as a result cannot determine any mechanisms behind any preferential erosion that occurs. To investigate the impact of deposit volume on the triggering of channelised remobilisation in landslide deposits I used the slope stability model proposed by D'Odorico and Fagherazzi (2003). This model uses topographic parameters and the depth of sediment, in this case a landslide deposit, to determine the likely height of water within a deposit required to produce a failure.

$$Z_w = \frac{\gamma_{sat}}{\gamma_w} h \left(1 - \frac{\tan\beta}{\tan\phi}\right) + \frac{c}{\gamma_w \tan\phi \cos\beta} \qquad \text{Equation 11}$$

Z_w is the height of water (m) above the base of the landslide deposit, γ_{sat}(kN m^{-3}) is the weight of the sediment when saturated, γ_w (kN m^{-3}) is the unit weight of water, h is the thickness of the deposit (m), β is the local slope angle (radians), ϕ is the internal friction angle (radians) and C is the cohesion of the deposit (kPa). Within this model I set cohesion to zero due to the loose nature of the deposits, other values for these parameters can be found in Table 7. This model predicts that deeper soils on high slopes are more susceptible to failure than shallow deposits but on shallow slopes the opposite is true (D'Odorico and Fagherazzi 2003). Using this model helped to separate the influence of deposit volume from its topographic position.

4.2.2 **Modelling triggering mechanisms**

There are several different ways by which a debris flow can be triggered. They can initiate during the runout of a landslide if it becomes disarticulated (Iverson et al. 1997), through the collapse of a channel bed (Takahashi 1981; Prancevic et al. 2014) or by reaching a high sediment concentration via the gradual entrainment of channel sediment (Lamb et al. 2008; McGuire et al. 2017b). Using physically based models of sediment stability I identified the possible mechanisms by which debris flows could occur. There is little geotechnical data of landslide deposits or precipitation data available for calibrating slope stability models in Wenchuan County, so I have used simple models which require minimal parameterisation.

To model triggering of debris flows by landsliding I used the SHALSTAB model presented by Montgomery and Dietrich (1994) (Figure 31).

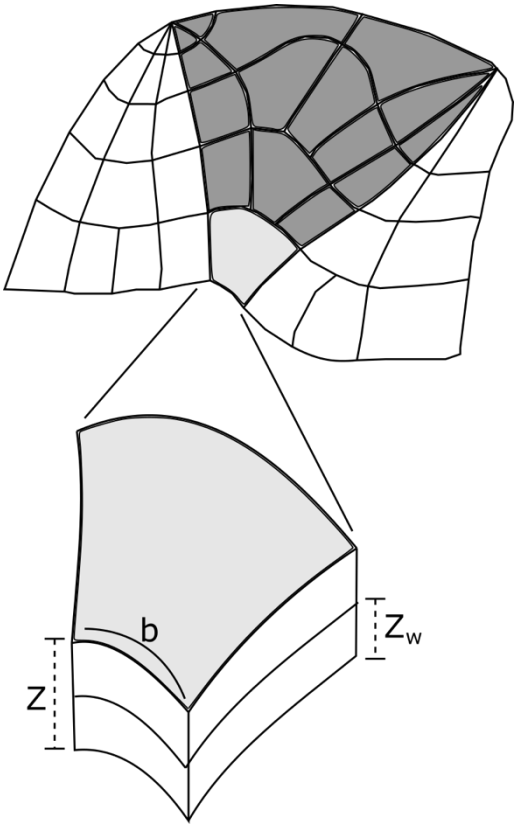

Figure 31 A conceptual diagram of the Shalstab model showing how water moves through the subsurface, figure adapted from (Montgomery and Dietrich 1994). Z is the soil depth Z_w is the height of the water table above an impermeable layer and b is the cell width.

SHALSTAB (Shallow Landslide Stability) is a model for identifying potential areas of shallow landsliding in soil mantled landscapes based on a combination of a simple hydrology and slope stability models (Montgomery and Dietrich 1994; Dietrich and Montgomery 1998; Michel et al. 2014) (Figure 31). The model estimates how stable cells (or pixels of a DEM) are on a hillslope for a given precipitation amount based upon the transmissivity and friction angle of the soil and the convergence (or drainage area) and steepness of the landscape.

$$\frac{q}{T} = \frac{\rho_s}{\rho_w}\left(1 - \frac{\tan\beta}{\tan\phi}\right)\frac{b}{A}\sin\beta \qquad \text{Equation 12}$$

In this formulation q is the 24-hour steady state rainfall (m d^{-1}) and T is the saturated soil transmissivity (m^2 d^{-1}), b is the width of a cell of the DEM (m) and A is the maximum drainage area of the deposit (m^2), q/T is typically logged rather than being left as very small numbers. *Log(q/T)* is greatest in areas of shallow slope, which are much shallower than the friction angle of the soil, where even if the soil is saturated the slope does not fail.

These areas, most commonly channels or ridge tops, are unconditionally stable. *Log(q/T)* is smallest in areas of steep slope where the hillslopes is steeper than the friction angle of the soil. These areas can fail without the presence of water and thus are unconditionally unstable (Dietrich and Montgomery 1998). The relationship between q and T is mapped out for a subbasin of the Pacific Coast Range in (Figure 32) taken from Dietrich and Montgomery, (1998). The saturation state of the soil is crucial for the pixels close to the friction angle but are in areas which are convergent enough for saturation to occur in intense rainstorms.

Equation 12 requires 6 parameters, 3 are derived from topographic analysis (A, b and β) and 3 material parameters, which are often estimated, depending on data availability. In this model I assumed several things; the first is that there is no cohesion, the next is that the landscape has little to no variation (either in space or time) in its physical properties, and the final is that sediment thickness is equal across the entire landscape and for each landslide deposit (Montgomery and Dietrich 1994; Dietrich and Montgomery 1998). These assumptions are significant but cannot be tested due to the lack of constraints on the variability of the properties in the deposits. The assumption of equality applies over the entirety of the landscape so that there is no difference between the transmissivity of the landslide deposits and the surrounding ground. A difference between the transmissivity in deposits and the surrounding landscape would reduce the flow of water passing into the landslide deposits compared to the modelled results. Finally, as indicated in section 4.2.1 the depths of deposits are likely to be an important variable for stability. By assuming zero cohesion and equal soil depth, I could not test the control of soil depth here so instead focus on the topographic and hydrological properties of landslide triggering.

I used Equation 12 to generate a map of $\log \frac{q}{T}$ for my study area. I used the GPM IMERG Final Precipitation L3 Half Hourly 0.1-degree V06 product from NASAs Multi-Satellite precipitation program to derive a steady state precipitation for the study area (Huffman et al. 2019). This precipitation data was obtained from the Giovanni platform (https://giovanni.gsfc.nasa.gov/giovanni/). The steady state precipitation was used to estimate the transmissivity of coseismic landslide deposits which were recognised to have failed from the multi-temporal landslide inventory. This estimated transmissivity allows the model to highlight coseismic landslides which are likely reactivate during a given precipitation event. The modelled stability of these landslides was then compared to the multitemporal landslide inventory for validation.

To estimate the transmissivity, I simply took the $\log \frac{q}{T}$ of a failed landslide, rearranged Equation 12 to solve for T using the 24-hour summed rainfall of a storm known to cause debris flows. I identified storms which caused widespread debris flow activity from the literature and used the IMERG precipitation data to estimate the steady state rainfall of the storm across the study area. I estimated the transmissivity of 10% of the failed landslides in the 2011 landslide inventory (~300 polygons) using the precipitation of the 14 August 2010 storm (Tang et al. 2012). As debris flow activity was reported across the whole study area during this storm it is likely many of the observed failures between 2008 and 2011 occurred at this time. The calculated 2011 transmissivity was then used as an input for the future runs of the model. To identify whether the model accurately identifies landslide susceptible to failure I rearrange Equation 12 to identify a drainage area threshold for failure. Any landslide deposit with a drainage area greater than the value modelled will be susceptible to fail in the chosen storm event.

$$\frac{A}{b} = \frac{p_s}{p_w}\left(1 - \frac{\tan\beta}{\tan\phi}\right)\frac{T}{q}\sin\beta. \qquad \text{Equation 13}$$

To identify the number of debris flows that can be described by the SHALSTAB model for a storm I simply compared the number of landslides predicted to be susceptible to failure with the number which are observed to fail in the multi-temporal landslide inventory. I ran the SHALSTAB model for 3 time steps (2008 – 2011, 2011 – 2013, and 2013 – 2015). To identify debris flow triggering storms I used database of large debris flows presented by Fan et al. (2019). This database presents the dates of all major debris flows in the study area following the earthquake. For each time step of the inventory I identified a date on which a major debris flow occurred and summed the total precipitation of the previous 24 hours and used this as q for the model run. As no significant debris flow activity was recorded after 2015, I did not model any time steps after this date. For each of these 3 time steps I kept the SHALSTAB model parameters (Table 7) the same as it is not known how these parameters vary through time. Any change in the number of failed landslides predicted by SHALSTAB could suggest the parameters do change through time.

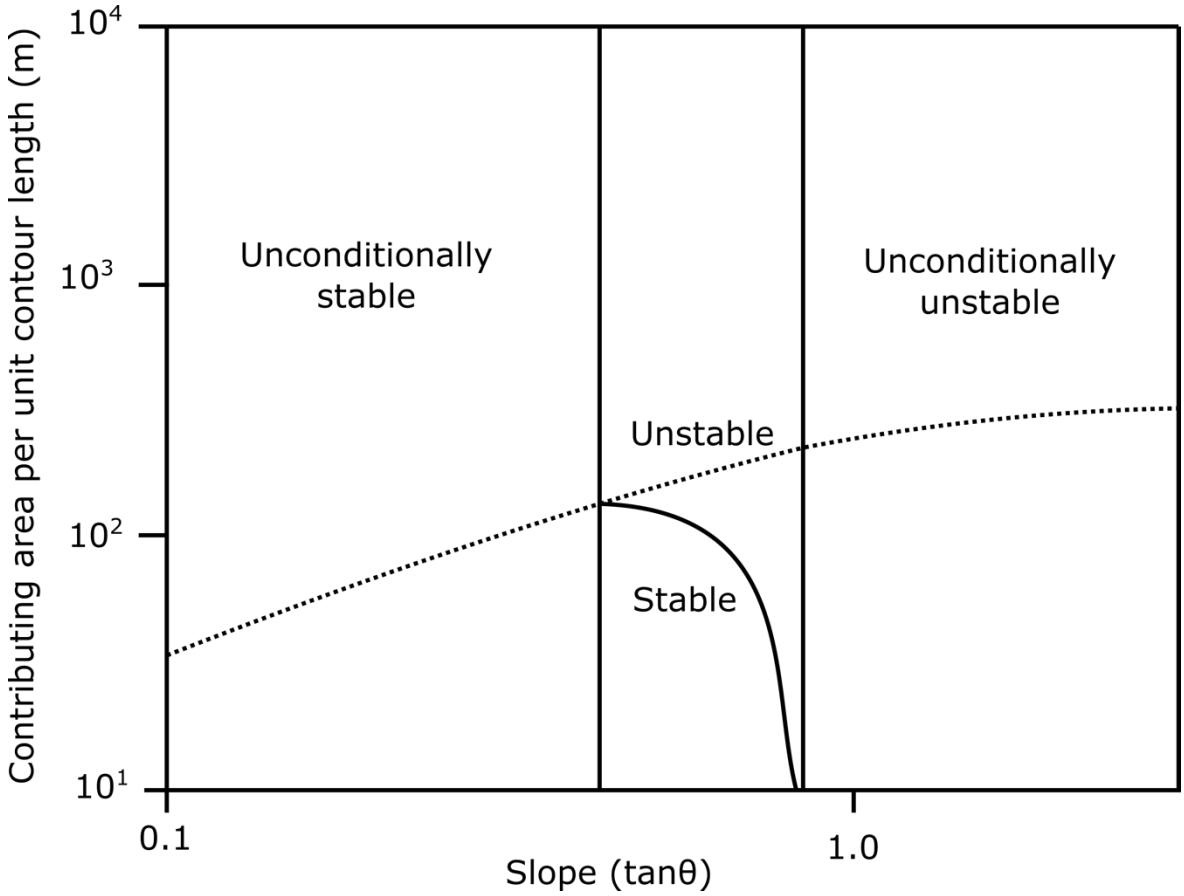

Figure 32 Equation 13 plotted for an example landscape with a friction angle of 40°, bulk density ratio of 2 and a T/q of 350m (Dietrich and Montgomery 1998). The dashed line is the threshold of saturation, any point above the line is saturated. The 2 vertical lines on the figure separate the landscape into 3 sections. Left of the first line is unconditionally stable as the landscape in this section can be completely saturated without failing. Right of the second line is unconditionally unstable as landscape in this section is always unstable, regardless of how wet the landscape is. The section between the two vertical lines is conditionally stable depending on the saturation of the landscape and its steepness. Hillslopes close to the friction angle only require a small amount of water to fail while shallower slopes need to be nearly completely saturated before they can fail.

Debris flows triggered by channel bed collapse was estimated using Takahashi's channel bed collapse equation, the concept of which I described in Chapter 2. Channel bed collapse can only occur in the channel network so only coseismic landslide with maximum drainage areas greater than the channel head threshold are considered in this experiment. For drainage areas greater than the channel head threshold a sampling routing algorithm was run to determine the runoff height above the channel bed (Adams et al. 2017).

$$d = \frac{qA}{b} \qquad \text{Equation 14}$$

d is the flow height; q is the average steady state precipitation (m s^{-1}) across the study area and b is the width of a cell of the DEM. I assumed all the precipitation was converted into runoff. The flow height is then used to calculate the bed shear stress (Lamb et al. 2008)

$$\tau_b = \rho_w g d \sin\beta \qquad \text{Equation 15}$$

before calculating the critical dimensionless shear stress τ^*c (Lamb et al. 2008).

$$\tau^*_c = \frac{\tau_b}{\rho_b - \rho_w} g D_{50} \qquad \text{Equation 16}$$

g is the acceleration due to gravity, ρ_b is the bulk density of the sediment, ρ_w is the density of the water and D_{50} is the median grain size. The simulated τ^*_c is then compared to the critical stress required for channel bed collapse to occur.

Along with channel bed collapse, debris flows can also occur due to entrainment. If the sediment concentration of run off reaches a critical threshold (normally around 40%) it will begin to act as a debris flow (McGuire et al. 2017a). I used the relationship between slope and τ^*_c derived experimentally by Lamb et al. (2008) to identify deposits which rather than failing catastrophically may fail by simple entrainment (Prancevic et al. 2014). I am only interested in the initial triggering of movement, so I do not use a more complex model to identify whether a debris flow is formed. I used the model of Lamb et al (2008) to separate the landscape into process zones similar to Prancevic et al. (2014) using empirical rather than parameter heavy models. The entrainment model of Lamb et al (2008) works best on slopes up to 30 degrees after which channel bed collapse is more common (Prancevic et al. 2014). The Lamb et al (2008) model is based upon a fitting algorithm from a series of physical experiments as such there are no parameters other than slope,

$$\tau^*_c = \exp[P_4X^4 + P_3X^3 + P_2X^2 + P_1X + P_0] \qquad \text{Equation 17}$$

X is 0.407ln(142tan(β)), P4, P3, P2, P1 and P0 are -3.57, 0.476, 0.199, 0.107, and 2.49×10^2 respectively. As with the channel bed collapse model I compared the τ^*_c produced by the model with the simulated τ^*_c from the flow routing. The predictions of each model (SHALSTAB, Channel collapse and Entrainment) were compared to each other to identify the dominant debris flow triggering process in the landscape.

Table 7 Input model parameters. All other parameters are calculated within the model itself

Parameter and units	Value	Reference
η, porosity, unitless	0.4	(Fan et al. 2012a)
ϕ, friction angle, unitless	35	(Wang et al. 2013)
β, slope angle	Derived from the DEM	(Mudd et al. 2020)
ρ_w, Density of water, kg/m^3	1000	-
ρ_b, Bulk density of sediment, kg/m^3	1800	(Fusun et al. 2013)
g_{sat}, Weight of saturated sediment, N/m^3	17083-18783	(Chang et al. 2011; Fan et al. 2012a; Fusun et al. 2013)
g_w, Weight of water, N/m^3	9800	-
h, Depth of landslide deposit (m)	Volume/Area of a landslide polygon	-
C, Cohesion	0	-
D_{50}	0.01m	(Cui et al. 2014)
q, Steady state precipitation (m/day)	Taken from IMERG data	(Huffman et al. 2019)
T, Transmissivity (m^2/day)	Estimated from model	(Montgomery and Dietrich 1994)
b, Width of cell, (m)	28.9m	-
A, Drainage area (m^2)	Calculated from DEM	-

4.2.3 **Triggering model performance**

The 3 models all highlight landslide deposits which are susceptible to failure in the chosen rainstorms. I calibrated the SHALSTAB model by calculating *T* using the storm of 2010 (Tang et al. 2012) on the failures of 2008 - 2011, therefore an initial good fit between the model and observations is expected. However, the good fit for this time step does not mean that the model can be used for predicting failure in other years, particularly if parameters change but are not accounted for (Reichenbach et al. 2018). A key indicator of a landslide susceptibility model's performance is the number of false positives the model produces. A model can be well fitted for an event, accurately identifying the areas of susceptibility by overestimating the susceptibility across the whole landscape. If a model has an excessive number of false positives it is likely it does not include the key drivers of failure in the landscape. If a model is well fitted to one event but not to another, shown by producing false positives, the triggering process or input parameters could have changed. I used the Threat Score to test each model's performance through time (Murphy et al. 2019),

$$TS = \frac{TP}{(TP + FP + FN)} \qquad \text{Equation 18}$$

where TP is true positives, FP is false positives and FN is false negatives. Each false prediction, whether it is a stable landslide deposit predicted to fail (FP) or a landslide deposit which fails but is not predicted (FN) reduces the performance score of the model analysed. The higher the Threat Score of the model, the more accurate it is, suggesting it closely captures the triggering mechanisms.

4.3 Results

4.3.1 **Spatial and temporal analysis of channelised remobilisation.**

Reactivations are most common in the first 3 years after the earthquake. From 2008 to 2011 3357 landslides are reactivated (Figure 33). The number of landslide deposits reactivated rapidly decreases with just 50 deposits being reactivated between 2015 and 2018.

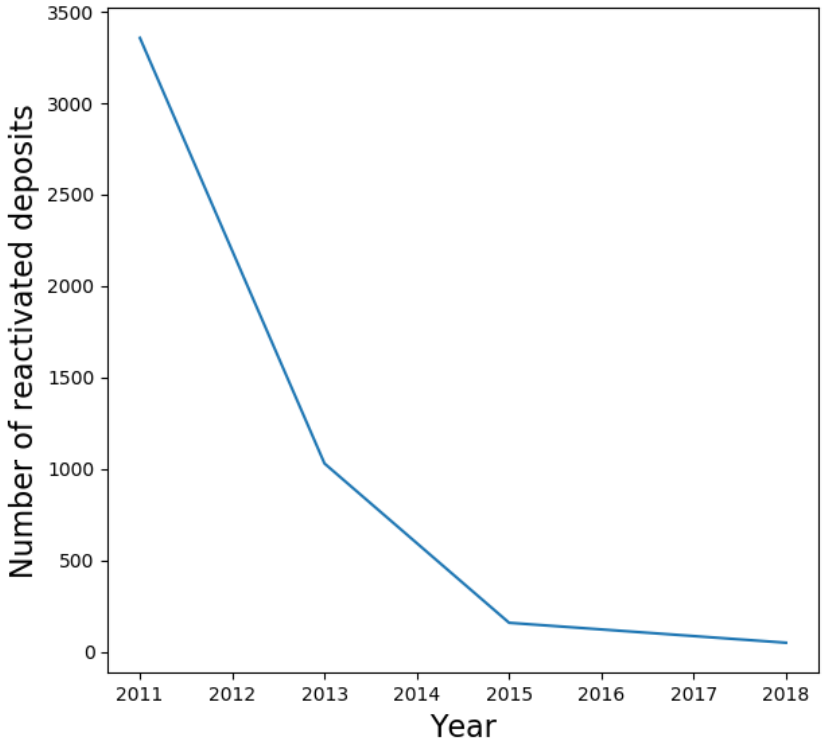

Figure 33 The number of reactivated coseismic landslide deposits through time , including deposits which remobilise multiple times. These numbers include reactivations which do not contribute to the channel deposits.

Of the 8830 coseismic landslide deposits mapped in this study, 5041 (up to 38% of the total volume) were not remobilised during the observation period. 3042 were remobilised once, and the remaining 747 were recorded being remobilised up to 3 times (Table 8). Despite the majority (80%) of reactivated deposits only being remobilised once, after 2011 a landslide deposit with a history of remobilisation is more likely to be reactivated than a deposit with no history of failure (Table 8). In 2013 close to two thirds of the deposits that are remobilised by a debris flow were also remobilised by a debris flow in 2011.

Table 8 Number of landslide deposits being reactivated through time and the number of times they have been previously reactivated.

Reactivation	**2011**	**2013**	**2015**	**2018**	**Total**
First	2636	338	45	23	3042
Second	0	608	60	19	687
Third	0	0	52	8	60

The most stable landslides, those which have no recorded channelised remobilisation within them, are on slopes with lower drainage areas than the less stable landslides. Through time, the median drainage area of reactivation increases, and the median slope remains the same until decreasing in 2018 (Figure 34). Landslides that remobilise multiple times are also in higher drainage areas but with similar or shallower slopes (Figure 35).

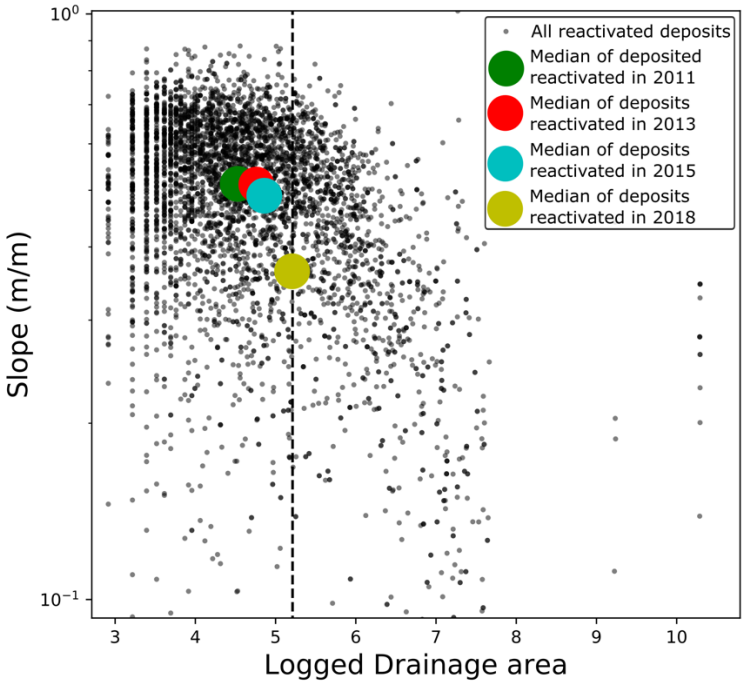

Figure 34 The median locations of reactivated landslide deposits through time. The small points are the locations of any landslide deposit which reactivated during the observation period. The median locations of failed deposits in a given time interval are highlighted as larger points. The dashed line marks the threshold drainage area between hillslope and channels.

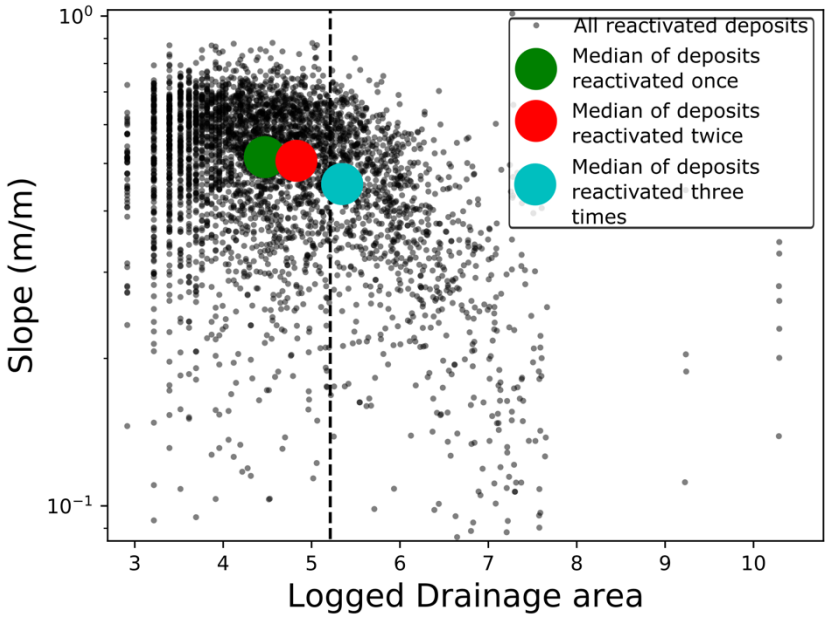

Figure 35 Location of landslide deposits with the number of times they are reactivated during the study period. All landslide deposits which reactivate are plotted as small black points with the median locations of different reactivation classes as much larger points.

4.3.2 **Deposit volume controls on stability**

The landslides in the first quintile (the largest landslides) are in higher drainage areas than those of the landslides in the last (the smallest landslides). Despite being in higher drainage areas, the landslides in the largest quintile were the least likely to be reactivated (Figure 36). Per km^2 of landslide surface for the first time period (2008 – 2011), the first quintile has 900 remobilisations while the last has 18,445 (Figure 37). This preference for reactivating the smallest over the largest landslides decreased through time from 30x more remobilisations in 2011 to 4x in 2018 (Figure 37A).

The volume of channelised remobilisations is calculated using an average 2m depth. I chose this depth as a result of the work described in chapter 3. The sediment discharge from each quintile into the channel network decreases through time, due to the frequency of remobilisations decreasing (Figure 37A & B). Interestingly the rate of the decrease in the frequency of remobilisations was greater than the rate of decrease in the discharge of sediment into the channel network. As not all channelised remobilisations reach the channel network, the decrease in sediment discharge from the landslides is due to both a decrease in the overall frequency of remobilisations and an increase in the number of remobilisations which do not reach the channel network. The smallest landslides are furthest from the channel network consistently reactivate more than the largest landslides but in 2018 were not the largest contributors to the channel network (Figure 37B). The

decrease in mobility, implied by the increase of the proportion of channelised remobilisations, is demonstrated by the lack of correlation between volume deposited in the channel and number of remobilisations between 2015 and 2018 (Figure 38A). Prior to 2015 most channelised remobilisations reach the channel network but after 2015 the distance to channel network becomes a much more important factor in determining whether sediment enters the channel. Finally, comparing the number of remobilisations to the volume deposited into the channels suggests that while the larger deposits are less likely to be remobilised, each remobilisation delivers more sediment to the channel (Figure 38B).

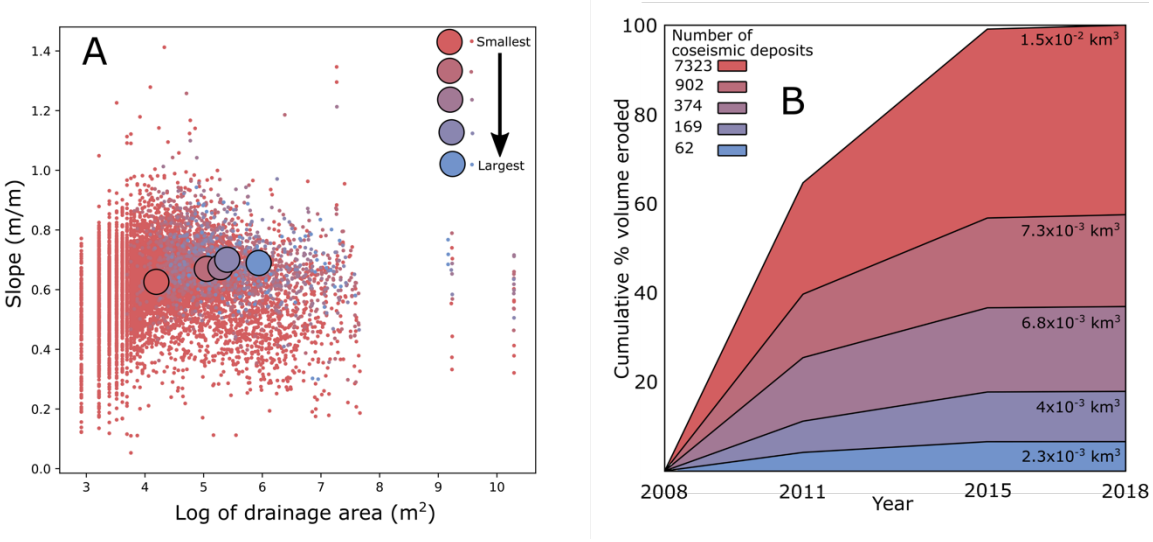

Figure 36 The location of the binned landslide deposits and the volume eroded from them A) The location of the landslide deposits in each volume quintile. Small dots represent the toe of each deposit while the large circles indicate the median location of the landslides in each quintile. B) The volume of sediment deposited into the channel from each volume quintile normalised by the total volume which enters the channel for the entire study period. Over 60% of the sediment entering the channel had done so by 2011. Close to 50% of the sediment in the channel network originated from the quintile with the smallest landslides (red).

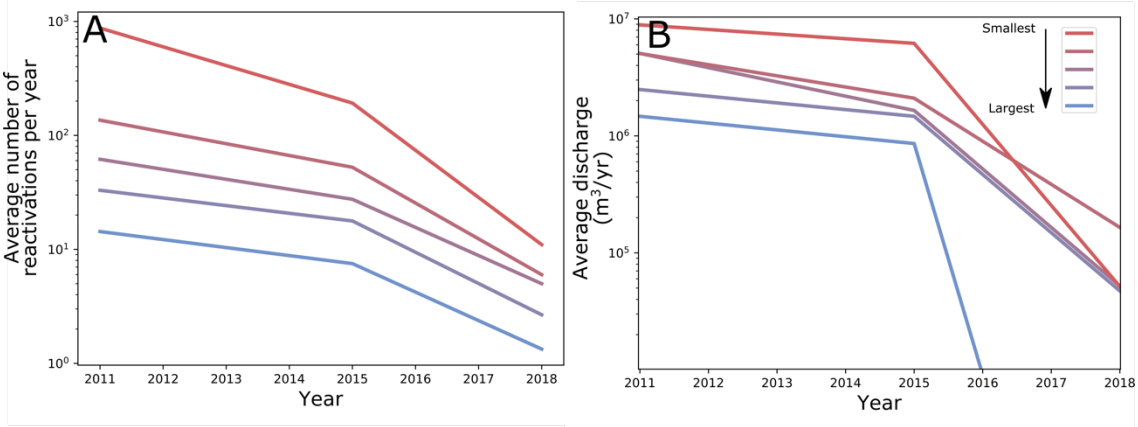

Figure 37 A) The number of channelised remobilisations within the landslides of each quintile per year. B) The discharge of sediment deposited into the channel from each quintile. No sediment leaving the largest deposits enters into the channel between 2015 and 2018.

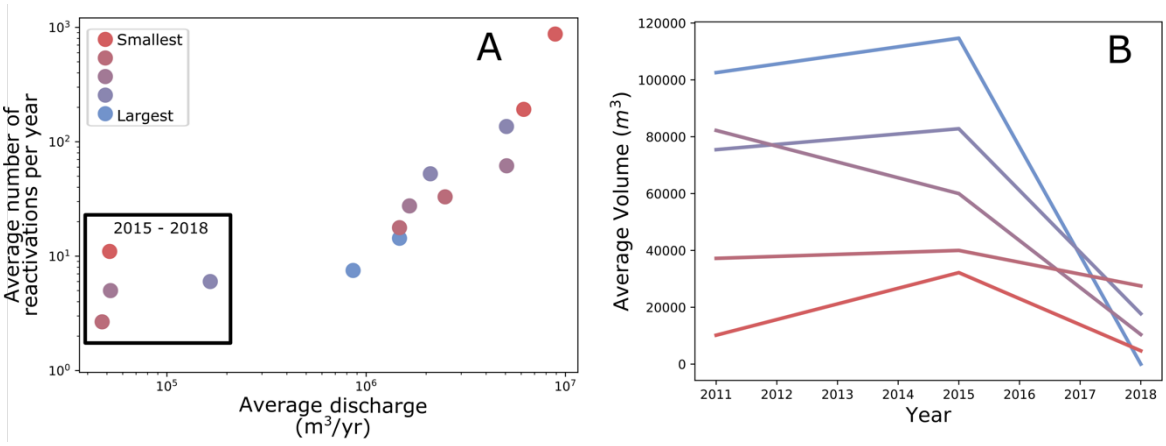

Figure 38 A) The discharge of sediment from the landslides into the channel compared to the number of remobilisations occurring per year. The period of 2015 – 2018 is highlighted due to the lack of correlation. In this final period the largest landslides (blue) do not contribute sediment to the channel deposits. B) The average volume (total volume/total number of channelised remobilisations) of sediment deposited into the channel from each quintile through time.

Modelling the height of water required in a landslide deposit for failure to occur (Equation 11) reveals that the smallest landslide deposits, on average, require lower water tables (Figure 39). Many of the predicted heights of water are significantly larger than the thicknesses of the deposits suggesting these deposits require substantial pore pressures to fail, likely more than can be achieved via simple throughflow. Equation 11 suggests that many of the smallest deposits do not require water to fail as they are on slopes greater than the friction angle. In all quintiles, landslide deposits on lower slopes are more stable than those on steep slopes. Despite this, the smallest deposits on the steep slopes become much less prone to reactivations through time which shifts the median triggering location downslope (Figure 40). This behaviour is not easily explained by Equation 11.

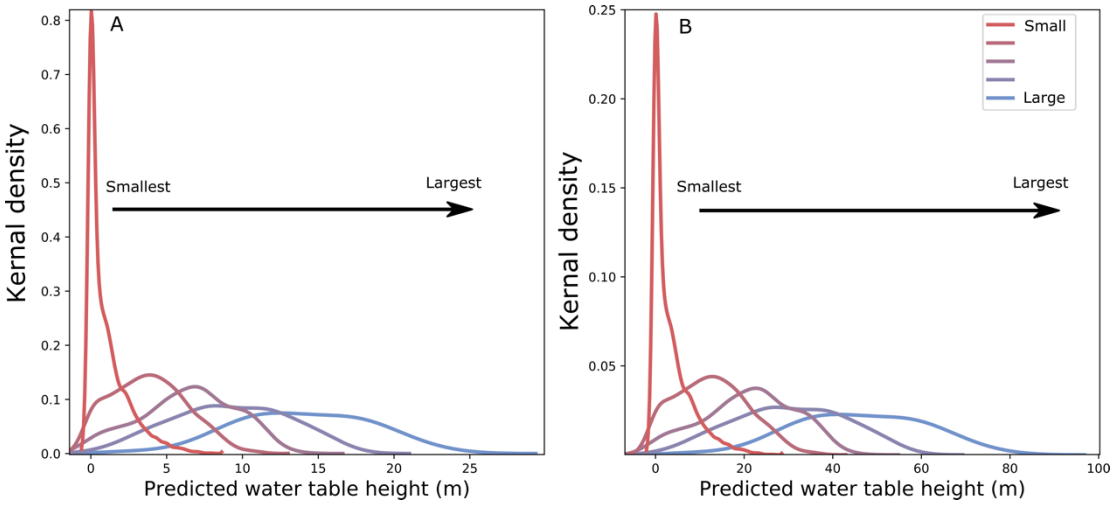

Figure 39 The predicted water table height required to produce a failure in different sized landslides. A uses the minimum depths of the landslide (landslide volume/area) while B uses the maximum depth (landslide volume/(area/3)). Large landslides require significantly higher water tables to fail due to their thickness and their position on lower slopes. Many of the deposits require heights of water much higher than the maximum depth suggesting they could be unconditionally stable. Negative values are an artifact of the smoothing of the plotting.

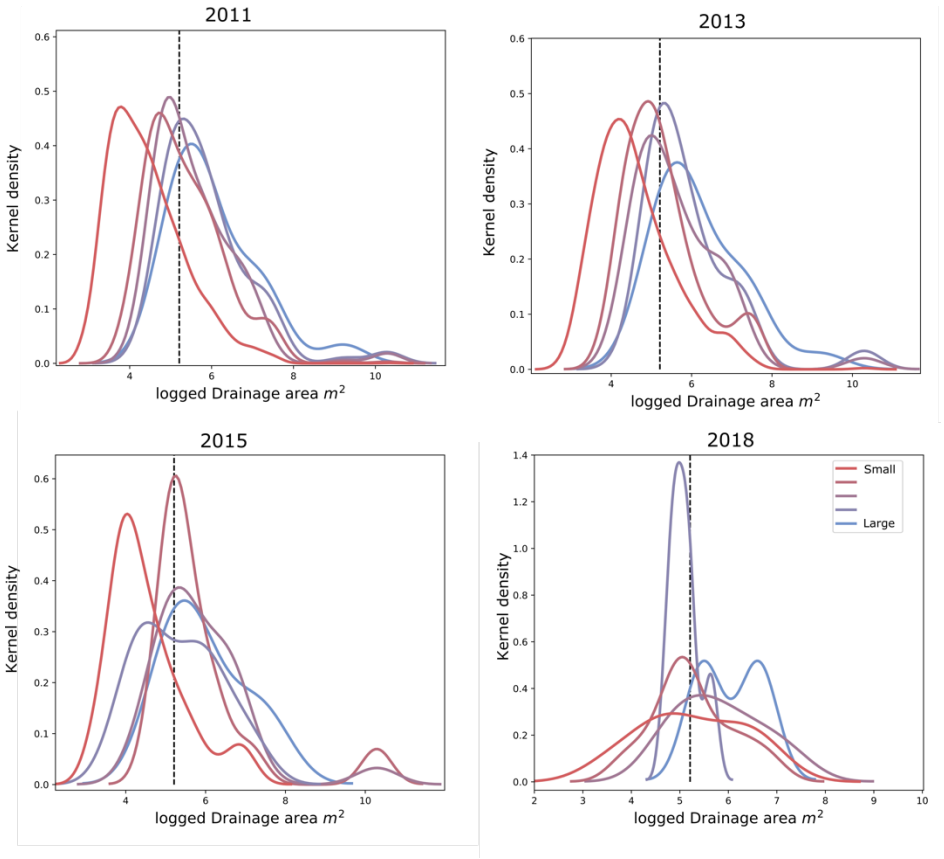

Figure 40. Kernel density plots of the log (base 10) of the drainage area of the reactivated landslides of each quintile in each timestep. In each timestep the smallest reactivating landslides are located at the lowest drainage areas until 2015-2018. In 2018 all reactivated landslides are close to the channel network (channel heads threshold highlighted by black dashed line), highlighting a shift of reactivation towards the channel network.

In summary, for the first 7 years after the earthquake, landslide deposits across the entire landscape are prone to being reactivated. The smallest deposits are preferentially eroded for most of this time, potentially due to resting on slopes greater than or close to the recorded friction angle. These deposits, despite being predicted to be the most unstable, stabilise the fastest, driving reactivation activity downslope. Alongside this stabilisation activity the channelised remobilisations become less mobile through time decreasing the volume of sediment deposited into the channels. These activities are not adequately described by a simple slope stability model.

4.3.3 **Triggering mechanisms of channelised remobilisation**

By comparing the drainage area of instability computed by SHALSTAB and the drainage area of the coseismic landslides I identified reactivations which could have been triggered by landsliding. Depending on the intensity of the storm being modelled and the number of reactivated landslides, between 95 and 98% of the channelised remobilisation polygons can be described by saturation driven landsliding. The models of entrainment and channel bed collapse are less successful in describing the failure of landslide deposits with just 6-17% of the failing deposits predicted by the runoff driven failure mechanisms (Figure 41). The poor performance of the runoff driven models is most likely due to the small number of deposits in channels. 85% of the landslides are in areas highlighted as susceptible to landsliding by SHALSTAB while just 19% are in channels which can generate shear stress great enough to cause failure by entrainment or channel bed collapse.

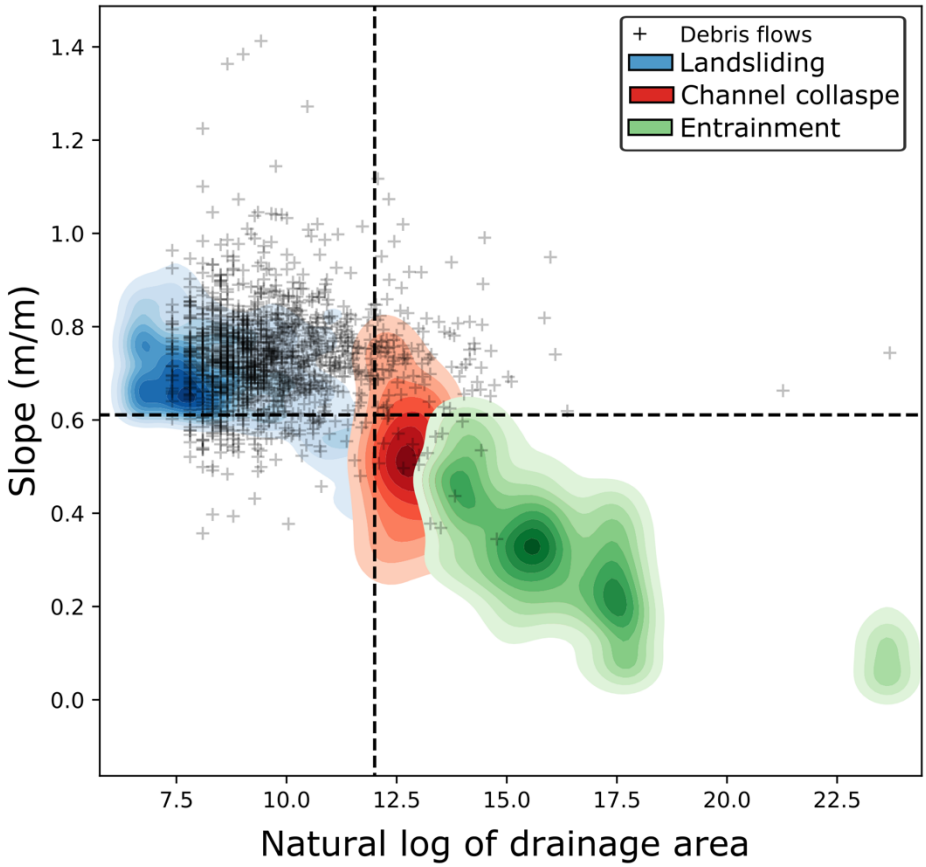

Figure 41 The slope and drainage area of the landslides which have been predicted to be susceptible to failure by the different tested models are shown in the different coloured contours. Dark colours indicate high densities of failing landslides while lighter indicate lower numbers of landslides. This figure shows how the landslides can be separated into debris flow initiation or sediment transport zones. The vertical dashed line is the channel heads threshold while the horizontal is the friction angle. Most debris flows in 2011 occur on the hillslope and can be predicted by the SHALSTAB model.

The number of landslide deposits predicted to fail is significantly greater than the actual number of failures for each storm modelled, producing high numbers of false positives. The performance of the models decreases through time, suggesting the model parameters change through time. Initially the entrainment model has the highest threat score, 0.53, followed by the channel bed collapse model, 0.49, and finally the landsliding model with a score of 0.39 (Figure 42). The differences in scores are most likely to be due to the numbers of deposits being modelled by each process: the larger the number of deposits highlighted as susceptible to failure, the higher the number of false positives. By 2015 all the models perform equally poorly with scores of 0.03, 0.03 and 0.02 (Figure 42). The low performance scores of the models highlight that susceptibility models cannot be used as predictive models, particularly using static parameters.

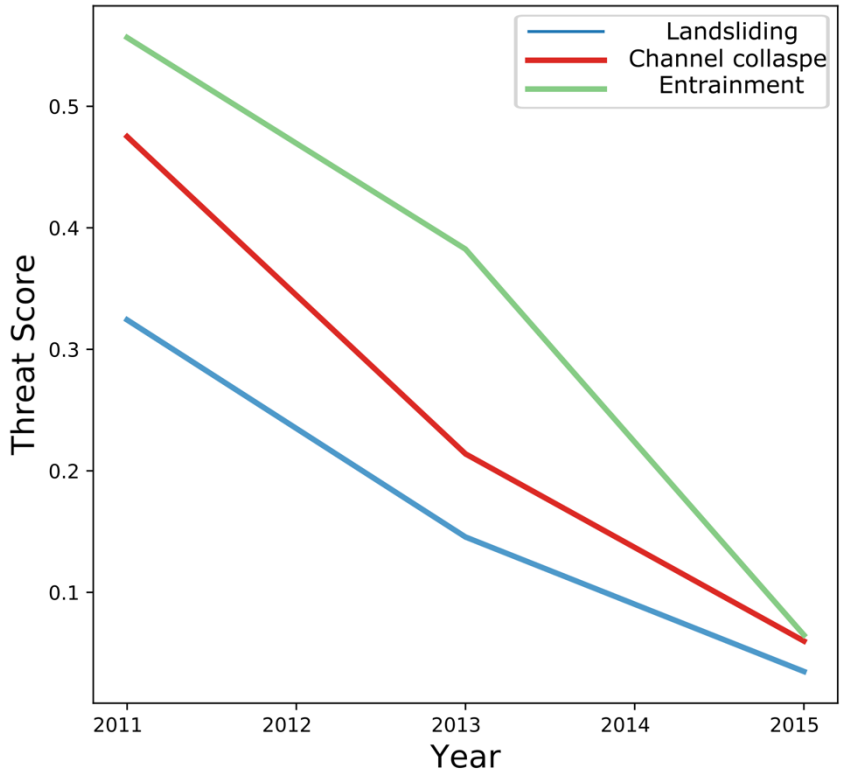

Figure 42 The threat score or performance of each model through time. Decrease in performance is primarily driven by increase in false positives through time.

Many of the hillslopes in the Longmen Shan are above the estimated friction angle of the coseismic landslides. The landslides that have come to rest upon these slopes are classified as unconditionally unstable by SHALSTAB. Figure 41 shows that the majority of the landslides have maximum slopes above this value and so could fail at any point in the future.

4.4 Discussion

4.4.1 **Triggering debris flows**

All the models significantly overestimated the number of landslide deposits susceptible to failure. The landsliding model, Shalstab, was the best performing model, as it correctly predicted the most failures, but overestimated the susceptibility of many of the landslide deposits producing many false positives. The channel-based models, channel bed collapse and entrainment, produced lower numbers of false positives but on a much smaller number of landslide deposits. Here I will examine three possible reasons for why these models poorly represent the triggering of debris flows: (1) the internal friction angle parameter was

wrong, (2) the hydrology of the deposits is not properly represented or (3) the triggering process is not as simple as described in the chosen models.

(1) The friction angle is a key parameter in the landsliding model and the channel collapse model, and if this parameter is too low it will overestimate the susceptibility of landslides on shallow slopes. The friction angle is also a highly sensitive parameter and slight changes can drastically change the outcome of the model. When comparing the slope of landslides that are falsely highlighted as susceptible to those that actually failed there is no clear difference in the slopes (Figure 43A). Having no clear difference between the landslides which fail and those that are predicted to but do not could suggest that using the maximum slope of a landslide polygon may not be representative of the deposit's stability. The surface slope of the deposit could be different from the landscape and so I could have prescribed a higher slope than the actual to the deposit. Another possibility is that rather than a friction angle which describes all the stability of all landslides it varies based upon the conditions of each deposit. If the friction angle varies from landslide to landslide some will be more prone to failure than others on similar slopes. This variation could help to explain why there is minimal difference in slope between those landslides which fail multiple times and those that do not (Figure 35). Between 2015 and 2018, a period I was unable to include in my modelling, the slope of failing landslides is lower than the deposits which do not fail (Figure 34). As the decrease in slope of failing landslides is not matched with an increase in the number of failures (the frequency decreases rapidly through time) this could be evidence for hydrology rather than slope being the driving factor for failure.

(2) A key assumption of SHALSTAB is that the transmissivity of the landslide deposits does not vary significantly from the surrounding landscape. The model transmissivity is parameterised based upon the failures that occur in coseismic landslide deposits during the first time step. Therefore, implicitly I assume the surrounding landscape has a similar transmissivity: if the landslide deposits are more conductive than the surrounding landscape the model will overestimate the throughflow traveling through the deposits. If this is the case, the model will produce more false positives in lower drainage areas. False positives are found in lower drainage areas than true positives for all the years modelled (Figure 43B). Although if hydrology is the main factor in controlling failure, and the importance of slope is overestimated, it is expected that more failures would occur in higher drainage areas (Figure 32).

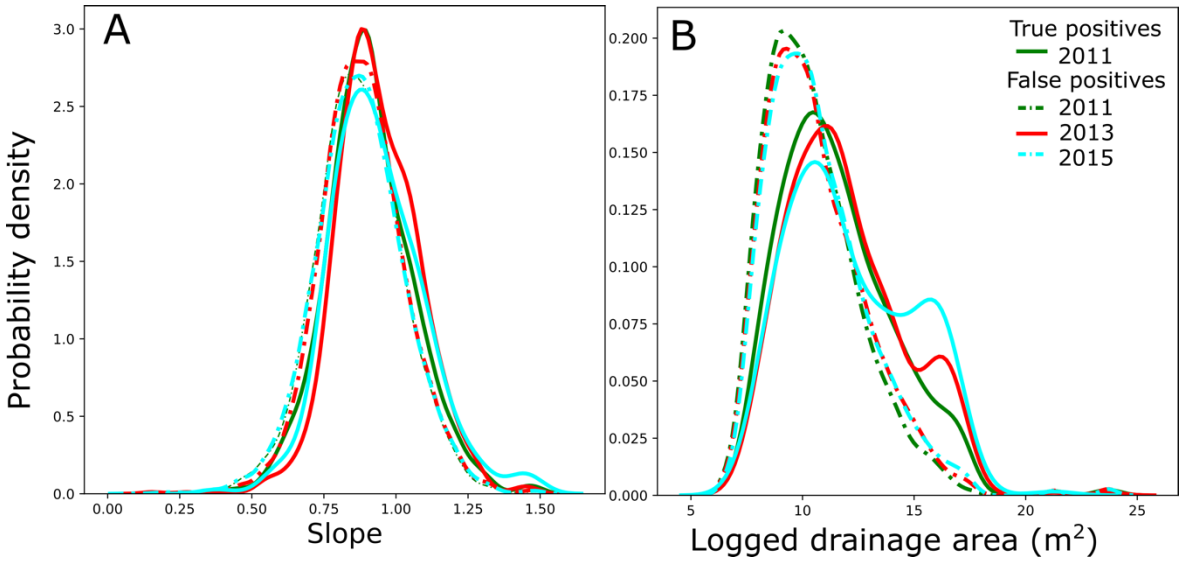

Figure 43 The location of simulated true (full line) and false positives (dashed line), colours indicate the different years modelled. A) The kernel density plot of the slope values of true and false positives of all models. B) The kernel density plot of logged drainage areas of false and true positives.

(3) Finally, it is possible that none of these models capture the complexity of the mechanisms involved in triggering debris flows in landslide deposits. These models are susceptibility models so can only suggest areas where failure can occur, none are based upon the actual conditions of the landslide deposits. SHALSTAB does not model the triggering of landslides, only the susceptibility. Another process such as infiltration driven pressure waves (Iverson 2000), pore collapse (Iverson 2000; Gabet and Mudd 2006) or pore space blocking resulting from mobile fine sediment (Cui et al. 2014; Hu et al. 2018) may be required before failure can occur. The models I chose to use for initiation in channels may also be too simple for debris flows. The channel bed collapse and entrainment models only identify where sediment transport occur and do not distinguish between floods and debris flows unlike more sophisticated models (McGuire et al. 2017 and Tang et al. 2019). Floods can move sediment but the sediment concentration is not great enough to produce a debris flow. Finally, I used a static coseismic landslide inventory to identify areas where debris flows occur. In reality sediment will move through the system and increase the susceptibility of debris flow triggering in some areas and decrease it in others. This section identifies the need to better understand the controls on the friction angle of landslide deposits, the hydrological relationships between landslide deposits and the surrounding landscape and testing of more complex models to identify possible locations of post-earthquake debris flow triggering.

4.4.2 **Stabilising landslide deposits**

In this study I have shown that the number of landslide deposits transforming into debris flows decreases rapidly through time. The decrease in reactivations can occur due to (1) weaker rainstorms since 2011, (2) colonisation of the landslide deposits by vegetation, (3) changes to the compaction and grain size distribution of the landslide deposits. I will examine each of these mechanisms individually.

(1) I examined the distribution of monsoonal strength for each year of the study period and the known debris flow causing storms used in the modelling experiments. Monson strength is defined as the sum of the precipitation which fell between April and October divided by the time period to get an average intensity (mm/hr). This was done for each year of the study to compare how the monsoon varied from year to year. While this analysis does not capture the impact of the largest storms during each time period other studies have successfully correlated annual landslide frequency and monsoon strength (Marc et al. 2015; Marc et al. 2019). I use the average monsoon intensity due to the lack of in situ rainstorm intensity records which can accurately record the maximum intensity of the rainstorms in a given time period. There is no correlation between monsoon strength and the number of failures that occur (Figure 44, Figure 45). The most intense channelised remobilisation activity occurs between 2011 and 2013 yet from the literature it is noted the most intense rainstorms (and monsoons) occur in the next timestep, 2011 – 2013 (Fan et al. 2019c). 2011 – 2013 has significantly less debris flow events than 2008 – 2011 despite the intense rainstorms. Both 2016 and 2018 have similar monsoon intensities to 2011 but again produce less failures. The lack of correlation between the monsoon strength and mass failures could be due to several factors. The first is the data used to estimate the monsoon strength has a low spatial resolution (0.1 degrees ≈ 11km). In mountain ranges rainfall can vary significantly over a single kilometre due the effects of relief on rainfall. Typically, the ridges are rained upon at greater intensities than valleys, the IMERG data is not able to pick up these effects and as a result will under estimate the rainfall in some areas while overestimating it in others. Further the averaging of the precipitation over a multi-month period cannot resolve the rain storms which actually trigger landslides. A monsoon season with a series of large intense storms could produce the same amount of rain as a more constant gentle monsoon season but significantly more landslides. Without in situ measurements of precipitation it is not possible to identify how variable rainfall is over time or space in the study area or how it may affect landsliding. Therefore the lack of correlation could be due to a change in precipitation parameters which I cannot record in my chosen data set.

Some in-situ records of precipitation do exist in the Longmen Shan and these reveal a similar story to my finding of a lack of correlation between precipitation and debris flows or landsliding through time. After the earthquake the rainfall – intensity threshold required for debris flow triggering has increased through time (Guo et al. 2016a; Ma et al. 2017). These thresholds are derived from rainfall data and debris flows inventories for catchments across the Wenchuan epicentre and represent an empirical estimate of the minimum rainfall required to produce a debris flow. An increase in the rainfall required to trigger debris flows could agree with the lack of correlation I see in my analysis of monsoon strength. An increase in the intensity-duration threshold of debris flow triggering could suggest that a change in the material properties or location of the landslide sediment occurs preventing the triggering of debris flows (Guo et al. 2016a; Ma et al. 2017).

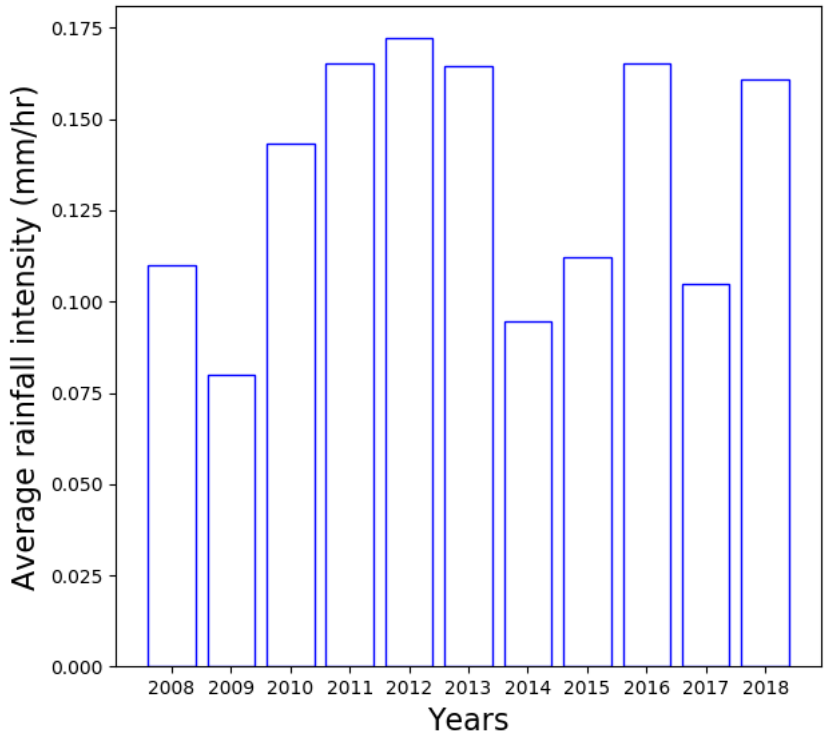

Figure 44 Average monsoon intensity through time derived from IMERG precipitation modelling. The total rainfall that occurred during the monsoon is estimated from IMERG data and divided by the length of the monsoon season to give an average intensity.

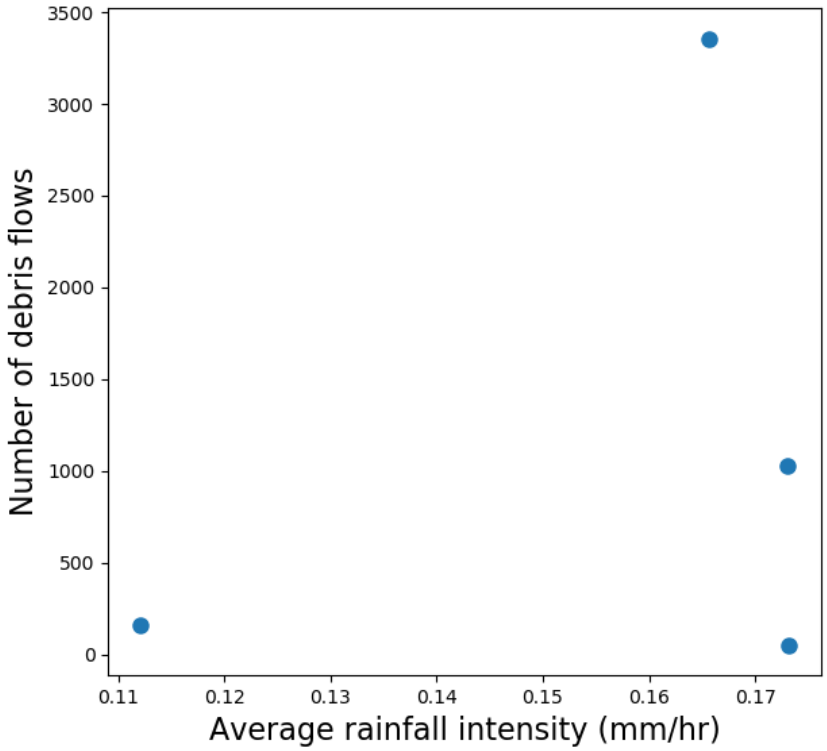

Figure 45 Number of debris flows triggered channelised remobilisations, vs the average monsoon intensity. There is no correlation between the frequency of debris flows and monsoon intensity suggesting the conditions of the deposits change through time.

(2) Vegetation can increase the stability of soil in many ways, it adds cohesion and shear strength to soil (Montgomery and Dietrich 1994; Wilkinson et al. 2002; Hales 2018), reduces the volume of sediment infiltrating the soil via transpiration and uptake in the roots (Wilkinson et al. 2002; Koyanagi et al. 2020) and, reduces the impact of raindrops and runoff on the bare surface (Cannon et al. 2001; Fusun et al. 2013; McGuire et al. 2016; Tolorza et al. 2019). Vegetation can therefore reduce the likelihood of failure by both runoff and saturation suggesting recolonisation of landslide deposits could be a significant factor in the stabilisation of the post-earthquake landscape. Vegetation has rapidly regrown following the earthquake, with the 'active' area of every deposit decreasing through time (Figure 46) (Zhang et al. 2014a; Fan et al. 2018a; Yunus et al. 2020). The active area of a landslide deposit is the location of fresh movement, therefore a decrease in the active area demonstrates some stabilisation has occurred. Once the sediment has stabilised vegetation can grow on it which can stabilise the sediment further. Correlating vegetation cover and decrease in remobilisation does not identify causation, remote sensing does not have the capability to identify whether vegetation grows on stable surfaces or they become stable afterward. Remote sensing also cannot be used for prediction or forecasting

as the imagery reveals little about the root network of the vegetation, the most important factor for stabilising sediment. In the Longmen Shan the first vegetation to colonise the landslides have been grasses and shrubs, a similar pattern to recovery after deforestation across the world (Fusun et al. 2013; Hales 2018; Shen et al. 2020). These short vegetation types have shallow root systems which do not add much strength to the soil but they can produce a dense cover significantly reducing the chance of significant runoff forming (Shen et al. 2020). The impact of vegetation on landslide deposits needs further investigation in order to constrain whether it stabilises the sediment.

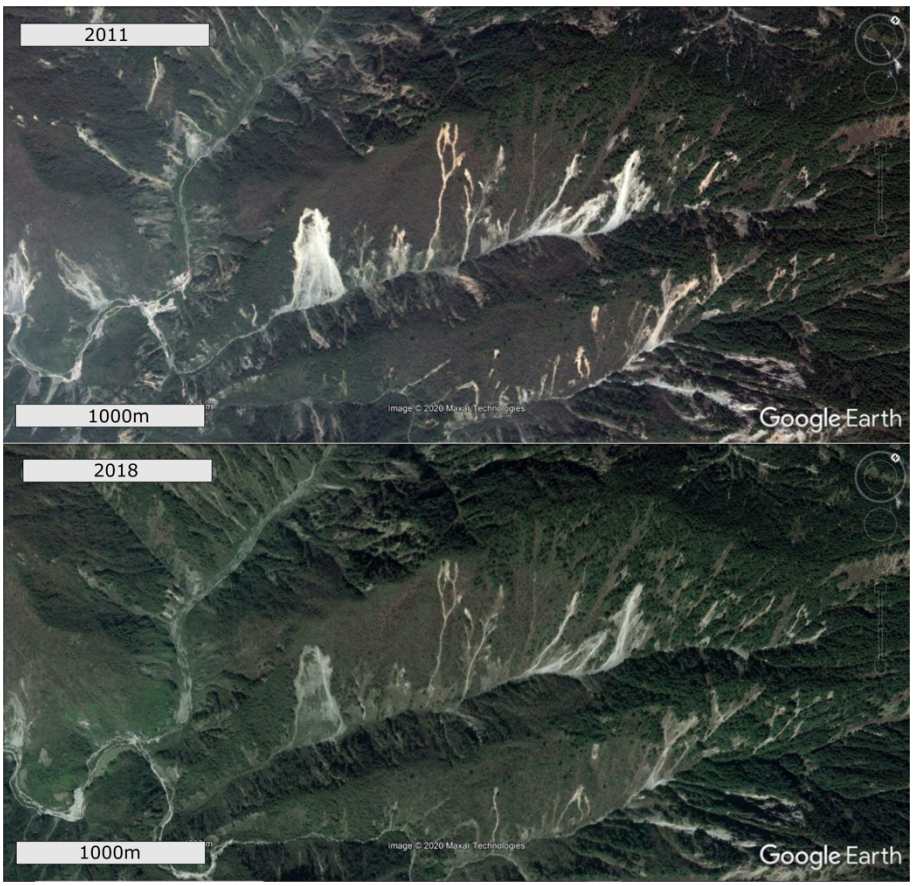

Figure 46 Satellite imagery of vegetation colonisation of areas affected by landsliding. Vegetation rapidly recolonises the bare sediment (white patches in the satellite image) following the earthquake. Growth of vegetation is a sign of stabilisation but remote sensing by itself cannot determine the root structure of the colonising vegetation which prevents estimation of any increase in cohesion.

(3) The internal and surface structure of the landslide deposit can greatly affect its stability, any change in the structure could enhance or decrease its sensitivity to rainfall. The structure of landslide deposits is not well understood however changes to the grain size distribution of landslide deposits have been inferred from field observations (Zhang et al. 2014b; Zhang et al. 2016; Zhang and Zhang 2017) and flume experiments (Cui et al. 2014; Hu et al. 2018). Compaction of the deposits is also expected through time due to

settling of the deposit (Hu et al. 2017; Hu et al. 2018). These changes are likely to alter the permeability of the deposits and the internal friction angle making failure less likely.

Landslide deposits in Wenchuan are extremely poorly sorted with grain size distributions ranging from meter scale boulders to microscopic clay particles (Cui et al. 2014; Wang et al. 2015). Fine grain sediment (<2mm) has been recorded to be up to 20% of a landslide deposits mass demonstrating it makes up a substantial proportion of a deposit (Cui et al. 2014; Wang et al. 2015). These fine grains make up the matrix of the deposit which the larger deposits are held within. This produces a structure through which water is expected to pass through easily, though the permeability or conductivity hasn't been calculated in the field. It is hypothesised from flume experiments the flow of water through landslide deposits erodes fine sediment out of the sediment (Cui et al. 2014; Hu et al. 2016; Hu et al. 2017). As fine sediment is moving through the sediment it could block pores causing local increases in pore pressures or collapses as the matrix supporting the larger grains is removed (Cui et al. 2014; Guo and Cui 2020). After a critical amount of fine sediment is removed failure could become much less likely due to the increase in porosity and decrease in fine sediment blocking pore spaces. However, only limited evidence of these effects has been seen in the field.

Evidence of the migration of fine-grained sediment from landslide deposits is indirect and based upon observations of debris flow deposits. In the Pubugou Ravine the deposits of 3 debris flows (occurring in 2008, 2010 and 2011) were identified and the grain size distributions were derived for each deposit (Chen et al. 2014; Zhang et al. 2014b) (Figure 47). Through time the deposits get coarser which has been used as evidence that the source material (coseismic landslide deposits) of flows has become coarser due to the loss of fine-grained material. However, these observations are based upon 3 flows in a small basin without direct analysis of the source area of the debris flows. This pattern of coarsening may be within the natural variability of debris flow deposits and therefore not representative of any changes occurring further up the catchment. These 3 flows are also unlikely to be representative of all the catchments affected by the earthquake. Other than this observation the main source of observations of the preferential erosion of fine grained sediment is from flume experiments. Cui et al. (2014) placed sediment from coseismic landslide deposits into a specially designed flume and recorded the changes that occurred in the deposit as a response to artificial rainfall. Fine grained sediment (< 2mm) was recorded leaving the deposit because of seepage and runoff without significant failure of the deposit. The grain size distribution of the deposit was measured at several depth

intervals and was found to be depleted of fine grained sediment at the surface and enhanced at the base (Cui et al. 2014).

These observations suggest that if the fine-grained sediment is mobilised from the landslide deposits, we would expect it to be either in the channel network or concentrated in the base of the coseismic landslide deposits. Recordings of suspended sediment discharge in the Min Jiang show an increase in the volume of fine sediment being eroded from the earthquake impacted catchments after the earthquake (Wang et al. 2015). However, the enhanced rate returns to its pre-earthquake rate with 5 years after the earthquake, long before all the fine-grained sediment is removed. Field observations of the landslide deposits reveal that significant fine-grained sediment remain, confirming widespread remobilisation of fine sediment is unlikely. Debris flow deposits coarsening through time is also not convincing evidence of fine-grained material seeping from landslide deposits. Through time debris flows have begun to trigger more commonly in channel deposits rather than on hillslopes (Zhang and Zhang 2017). The channel deposits are much more likely to coarsen through time than landslide deposits as water of greater and more consistent discharges pass through these deposits.

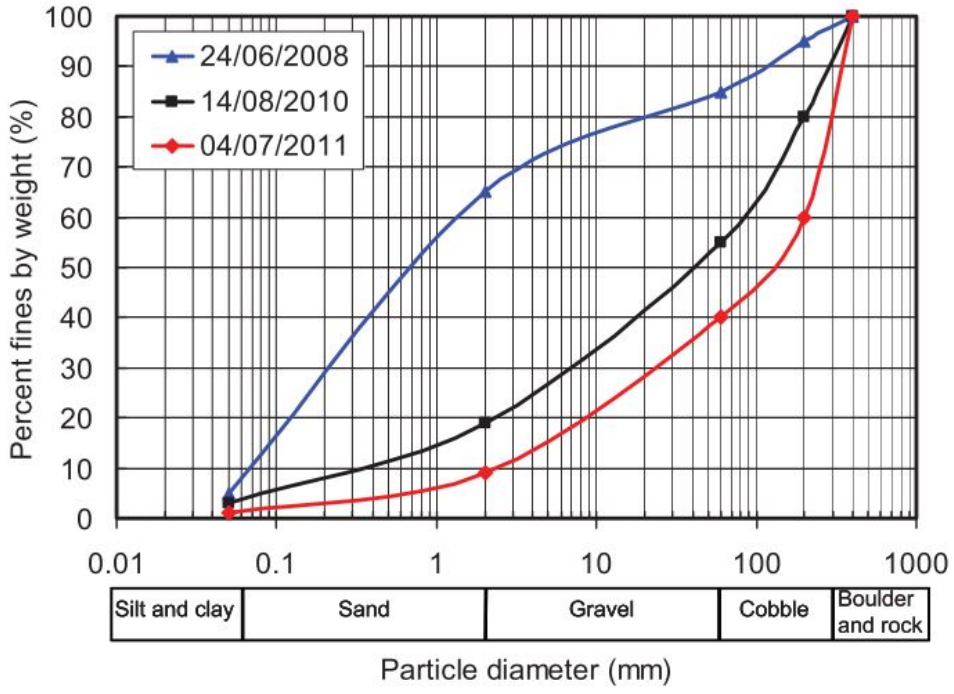

Figure 47 Grain size distributions of dated debris flows deposits. Three debris flows in the same catchment left deposits that became progressively coarser, this has been used as evidence for a coarsening of source material through time. Figure taken from (Zhang et al. 2014b). It is important to note that the coarsest material is not included in these distributions, so the apparent coarsening may be exaggerated.

Along with the remobilisation of fine sediment, producing a change in the hydrology of the deposits, an increase in the internal friction of the deposits is also expected. The internal

angle of friction is a measure of the sediment's resistance to shear stress and is controlled by how the individual grains within the sediment interact with each other. If the grains are close together with complex interlocking grain shapes and sizes a high friction angle would be expected (Bareither et al. 2008). Increasing the friction angle of a deposit would therefore require an increase in the degree of compaction.

It is not clear whether any compaction has occurred in coseismic landslide deposits due to the inability to compare current conditions to those in the past. However, some degree of compaction would be expected as the sediment settles into its most stable configuration after being disturbed (Marc et al. 2015; Parker et al. 2015). The amount of compaction that can occur is controlled by the volume and distribution of pore space in the deposits. If the space between large grains is full of fine sediment they cannot collapse together (Hu et al. 2018). The rearrangement of fine-grained sediment within deposits would therefore allow compaction to occur. As fine-grained sediment is removed from some spaces the larger grains are unsupported and collapse onto each other. In a flume experiment Hu et al. (2018) measured the impact of proportions of fine grained sediment on pore pressure and internal displacements prior to any induced failure. They demonstrated that as fine-grained sediment is removed from the deposit, the deposit compacts via many small movements of the larger grains rotating towards each other. This compaction occurs prior to failure and does not occur in tests where no widespread failure occurred. This suggests the mobilisation of fine sediment is crucial for failure (Figure 48). Failure in these loose deposits could be a multistage process where the remobilisation of fine sediment from the matrix between large grains encourages small scale movements of grains which could trigger wide spread positive pore pressures and failure (Hu et al. 2017; Hu et al. 2018). If the rainfall event is too short for a complete failure to occur the deposit is left in a more compact state with a higher internal friction angle, due to greater contact between grains, and a higher hydraulic conductivity which helps to prevent the build-up of pore pressures (Figure 49).

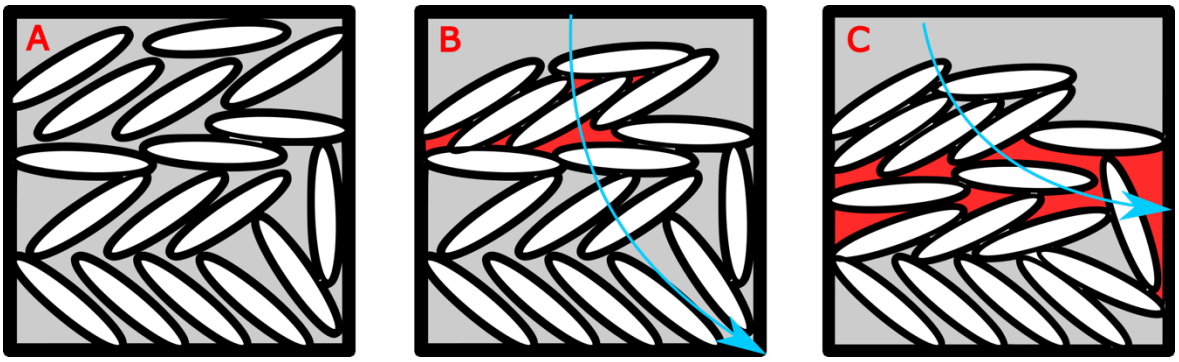

Figure 48 A conceptualisation of the collapse of grains in a deposit. A) grains are held up by fine grained sediment. As the fines are removed the grains collapse the pore space causing positive pore pressures (shown in red) (B). Initially these positive pore pressures cannot spread through the deposit so failure is localised, however as more fine sediment is mobilised the positive pore pressures can spread throughout the deposit (C). Infiltration of water driving the migration of fine material is shown with the blue arrows.

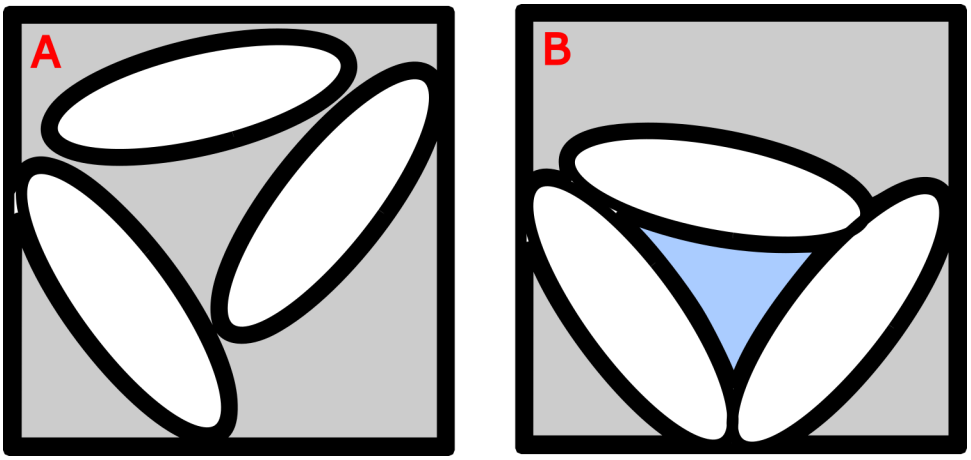

Figure 49 A concept of interaction between grains prior to and after compaction. In A) fine material (light grey) prevents large grain to grain contact decreasing the internal friction angle while the conductivity is also reduced. After compaction (B) the large grains are in contact producing a more stable structure which allows greater permeability (pore space in blue).

My modelling results and observations suggest that through time landslide deposits become harder to reactivate. Initially the smallest landslide deposits are preferentially reactivated, but these become progressively more difficult to remobilise (Figure 37) and the median location of reactivation is forced downslope towards the channel network (Figure 34). The move downslope rather than upslope suggests that a greater degree of saturation was required to cause failure (Montgomery and Dietrich 1994; Dietrich and Montgomery 1998). In the theory proposed by Hu et al. (2018) a critical permeability must be reached before failure can be widespread, similar to dense sediment (Figure 48) (Iverson et al. 2000; Gabet and Mudd 2006). Initially small deposits erode preferentially as the compaction can occur easiest and evenly in these deposits. Fine grained sediment

moves from the surface of the deposit to the base in response to rainwater moving through the deposit (Figure 48). In a small deposit this process will occur faster as there is less deposit to travel through. Once the fine-grained sediment has moved and a certain amount of compaction has occurred failure becomes too difficult to occur again (Figure 49). This suggests that deposits which have previously failed will be the most difficult to remobilise. This decrease in preference for previously failed deposits is likely driven by the smallest deposits. In fact, the smallest deposits are least likely to fail more than once with just 19.5% of the deposits which failed failing more than once, compared to 75% of the largest deposits (Table 9).

Table 9 The frequency of the reactivation of previously reactivated coseismic landslide deposits separated by landslide volume quintile.

	% Deposits reactivated 1x	% Deposits reactivated 2x	% Deposits reactivated 3x
1 (Largest deposits)	25	57.1	17.9
2	29.0	58.0	13.0
3	47.6	44.8	7.7
4	65.2	32.3	2.5
5 (Smallest deposits)	80.5	18.4	1.1

4.5 Conclusions

To conclude, landslides become progressively harder to reactivate via channelised remobilisation through time. Initially the smallest landslides are the most likely to be reactivated but the preference for small landslides decreases as time goes by. Modelling studies and spatial analysis of the channelised remobilisations suggest that the landslides most likely to fail are found further downslope through time, possibly due to an increase in the friction angle or an increase in hydraulic conductivity or a combination of the two. These could be related to compaction of the landslide deposits, though this compaction has not been recorded in the field. Any compaction and resulting stabilisation could be greatest in the smallest deposits as they are the least likely to fail repeatedly. Larger deposits require more reorganisation, and hence a longer time scale, before they stabilise.

Chapter 5 The impact of earthquakes on orogen-scale exhumation

5.1 Author Contributions

Much of this chapter is a reproduction of a collaborative paper between Myself, TC Hales, DEJ Hobley, X Fan, AJ Horton, G Scaringi and R Huang, (*Francis, O. R., Hales, T. C., Hobley, D. E. J., Fan, X., Horton, A. J., Scaringi, G., and Huang, R.: The impact of earthquakes on orogen-scale exhumation, Earth Surf. Dynam., 8, 579–593, https://doi.org/10.5194/esurf-8-579-2020, 2020).* While each author contributed to the drafting of the text and discussion of the ideas or funding, I am solely responsible for the design and writing of the model and experiments and the analysis of the results.

5.2 Introduction

5.2.1 **Research questions**

As I have shown in the previous two chapters, coseismic landslide debris produced by the Wenchuan earthquake has the potential to remain in the landscape, and on the hillslope for extended periods of time. It is commonly assumed that landslide derived sediment is rapidly evacuated from catchments, hence the long-term impact of this storage on the landscape has not been widely investigated. If significant volumes of sediment remain within the orogen on the timescales of seismic cycles the sediment may have impacts on erosion and the recording of erosion rates in tectonically active landscapes. Any effect the sediment has will likely also be affected by the magnitude and frequency of earthquakes.

In this chapter I look to answer the following research questions:

1) How does the storage of coseismic landslide sediment affect exhumation and surface uplift rates?
2) How are earthquakes recorded in exhumation records?

5.2.2 **Context**

Surface uplift of a mountain range is controlled by the balance of additive uplift processes and removal of material by surface, typically fluvial, processes. Earthquakes produce rock uplift and equally importantly generate exhumation via landsliding (Keefer 1994; Avouac 2007; Marc et al. 2016a). Landsliding events can scour deeply into bedrock, causing many hundreds or thousands of years of exhumation of the bedrock surface in a geologically instantaneous moment (Parker et al. 2011; Li et al. 2014; Stolle et al. 2017; Marc et al. 2019). Existing mass balances on single (Parker et al. 2011) or sequences (Li et al. 2014; Marc et al. 2016b; Li et al. 2019) of earthquakes demonstrate that landslide volumes of

large thrust earthquakes are comparable to, and may exceed, rock uplift. However, earthquakes are not the only rock uplift process in mountain belts; aseismic mechanisms such as viscous and elastic crustal deformation (Meade 2010; Simpson 2015), lithospheric delamination (Molnar et al. 1993; Hales et al. 2005), and isostatic rock uplift (Molnar 2012; Molnar et al. 2015) can also contribute. The total time-averaged mass balance, and any net surface uplift, is also affected by erosion between earthquakes (Yanites et al. 2010; Hovius et al. 2011; Marc et al. 2019). Therefore, the contribution of earthquakes to the generation of long-term surface uplift of mountains remains poorly constrained (England and Molnar 1990; Li et al. 2019).

Despite the importance of earthquake-triggered landslides in the total erosion budget of mountain belts, there is little evidence of large earthquakes in most sedimentary or exhumation records. The lack of widespread evidence of earthquakes could be due to the long term storage of coseismic sediment in mountain ranges, something that is not always considered in modelling exhumation and surface uplift of tectonic mountain ranges (Parker et al. 2011; Li et al. 2014; Marc et al. 2016b). Constraining the long-term contribution of earthquakes to a mountainous orogen is impossible without fully constraining the rate at which coseismic landslide deposits are removed from the mountain range and the contribution of non-seismic erosion and uplift. The rock uplift minus the coseismic landsliding produced by earthquakes is commonly assumed to be equal to surface uplift which directly assumes there is no sediment cover in the mountain range and thus all landslides are in bedrock (England and Molnar 1990; Li et al. 2014; Marc et al. 2016b; Li et al. 2019). If sediment remains in orogens for extended periods of time it is likely it will be remobilised, reducing the erosion and increasing the surface uplift of an earthquake. Remobilisation of coseismic sediment can also occur between earthquakes, altering sediment fluxes and estimates of erosion rates from cosmogenic nuclides (Yanites et al. 2009; Andermann et al. 2012; Dingle et al. 2018). Constraining any aseismic uplift and how it affects coseismic uplift is also be important for understanding whether earthquakes build mountain ranges (Royden et al. 1997; Hovius et al. 2011; Parker et al. 2011; Li et al. 2014). Using observations of the 2008 Wenchuan earthquake I can start to constrain the role of coseismic sediment production in landscape evolution and its impact on exhumation records and determine how these maybe impacted by aseismic uplift.

The rate at which landslide deposits can be evacuated from a catchment is typically related to the capacity of the fluvial system to transport the influx of sediment (Yanites et al. 2010; Croissant et al. 2017). After the Wenchuan earthquake however, this is not the case with debris flows being the key process responsible for remobilising sediment into the Min

Jiang. The stochastic triggering of debris flows, along with the rapid stabilisation of hillslope deposits, rather than a constant rate of remobilisation could be one reason why large pulses of sediment associated with single earthquakes are rare or absent from downstream sinks (Fan et al. 2018a; Zhang et al. 2019). Rather than a sink receiving a large impulse of sediment, which can be easily recorded via a change in average grain size or sedimentation rate, the rate change is instead smeared or shredded by stochastic sediment transport processes like flooding or debris flows (Jerolmack and Paola 2010).

Another reason for large earthquakes being missed in exhumation records could be due to the period of time the exhumation is recorded for. Cosmogenic radionuclides, such as ^{10}Be, record denudation over 10^3 years which is similar to that of the return time of large earthquakes. Large earthquakes can therefore be missed in these shorter records but stored in longer records such as thermochronometric data (averaging time of $10^{4\text{-}5}$ years), any difference between short and long term erosion rates could be due to the influence of earthquakes (Kirchner et al. 2001; Ouimet 2010). By investigating the variation of erosion rates with varying time scales, or with coseismic landslide density (Niemi et al. 2005; West et al. 2014), we may be able to identify the long-term impact of earthquakes on orogen scale erosion rates.

In this chapter I use a zero-dimensional volume balance model to explicitly track earthquake generated sediment through time in a hypothetical orogen based upon the Longmen Shan. I use the tracked sediment thickness into order to understand how earthquake-triggered landslides (EQTLs) affect exhumation and surface uplift at orogenic scales. My model co-varies the amount of aseismic uplift in the orogen, imposed earthquake magnitude-frequency relationships, and both the timing and maximum magnitude of earthquakes, under multiple possible uplift regimes, in order to fully investigate the role of earthquakes in orogen scale volume budgets. I then use these scenarios to investigate whether earthquakes can be identified from erosion or exhumation records over different timescales and by modelling cosmogenic radionuclide concentrations of sediment leaving the orogen. Finally, I test my hypothesis that the variation in recorded erosion rates in a landscape can be an indicator of seismic activity using a global database of cosmogenic radionuclide derived erosion rates.

5.2.3 **Definitions of terms**

This chapter is precise in its use of terminology around the changes in elevation of the various surfaces I discuss. These follow standard modern definitions (England and Molnar 1990), but as I am explicitly measuring the generation of regolith and the movement of two

surfaces (the topographic surface and the bedrock surface), the potential for ambiguity requires me to clearly define these terms:

Erosion is the transport away of material from a site, and thus, a change in the topography. In this context, it describes the full evacuation of regolith material from the model domain, i.e., removal of sediment from the entire mountain range.

Weathering is the in-situ conversion of rock into regolith. In this model, rock must be converted to regolith before it can be transported. I explicitly separate the role of EQTLs generating regolith by *weathering* bedrock from their role as (inefficient) *eroders* of bedrock and regolith – i.e., I separate their role in producing loose material from their role in transporting that material. EQTLs on average occur on hillslopes near ridge tops, typically with transport lengths less than hillslope lengths, with only the largest impinging on the fluvial system (Li et al. 2016a).

Regolith is the mobile transportable layer of sediment at the surface. In the model, regolith can be created by two distinct weathering mechanisms: landslides cutting into bedrock to create transportable debris, and soil production by physiochemical processes.

Uplift is the increase in elevation of a material or surface in an absolute frame of reference. I distinguish *rock uplift, topographic surface uplift*, and *bedrock surface uplift*. Rock uplift is the expected increase in the bedrock surface before considering erosion, it is either produced by coseismic or aseismic means. Bedrock surface uplift is the vertical distance moved by the bedrock surface after erosion. Topographic surface uplift is the total vertical distance moved after considering changes in the bedrock surface and the thickness of the regolith layer.

Exhumation is the approach of the rock mass towards the topographic surface and/or the bedrock surface, in the frame of reference of that surface. My model tracks both surfaces, so therefore it is possible to have a rock uplift event that causes exhumation relative to the bedrock surface without exhumation relative to the topographic surface, by thickening the regolith.

Denudation is used almost as a synonym for exhumation, but where the frame of reference is the rock mass or the bedrock surface, and the topographic surface moves towards it.

5.3 Methods

5.3.1 **0-dimensional volume balance model**

Here I present a generalised zero-dimensional mountain volume balance model which I use to test the impact of regolith storage on bedrock surface uplift and exhumation. In the absence of sufficient empirical evidence on the long-term spatial distributions of rock uplift, exhumation, and regolith volumes in mountain ranges, I simulate these parameters by treating the evolution of a landscape as a series of dimensionless seismic volume balances.

In my model I define the change in topographic surface elevation (S_T) with time as

$$\frac{dS_T}{dt} = U - E \qquad \text{Equation 19}$$

where U (units of length/time) is the thickness of rock entering the orogen during a time step and resulting in rock uplift (calculated as the volume entering the orogen across the area of the model per unit time), while E is the rate of regolith removed (length/time) from the topographic surface and thus is the long-term erosion rate of the orogen. Rock can enter the orogen in two ways, either via shortening and thickening of the crust during coseismic thrusting earthquakes (U_{co}) or through one of a number of aseismic uplift mechanisms (U_{as}), such as lower crustal flow (Royden et al. 1997) or lithospheric delamination (Hales et al. 2005). Coseismic deformation (Bonilla et al. 1984; Wells and Coppersmith, Kevin 1994), and hence the volume of rock uplifted, scales as a function of earthquake magnitude (Li et al. 2014; Marc et al. 2016b). The addition of mass to a column of crust by thickening will produce an isostatic compensation which will reduce the overall surface uplift response to rock uplift. In my model I apply a simple compensation based upon the relative densities of the crust and mantle to account for the isostatic response (Turcotte and Schubert 2002; Densmore et al. 2012; Molnar 2012). The calculated response is applied immediately to the volume balance and the surface uplift. I do not consider interseismic strain as an uplifting mechanism in this model due its limited contribution to permanent surface deformation (Avouac 2007). There is ongoing debate to how much surface uplift can be attributed to aseismic versus coseismic sources and how they interact (Royden et al. 1997; Hubbard and Shaw 2009). Acknowledging the complexity of the debate, I simplify the aseismic component of uplift and generalise it as the proportion of uplift that cannot be accounted for by U_{co}. Hence, topographic surface uplift can be represented as

$$\frac{dS_T}{dt} = U_{co} + U_{as} - E \qquad \text{Equation 20}$$

where the ratio between coseismic uplift rate (U_{co}) and aseismic uplift rate (U_{as}) is defined by the term α which represents the proportion of the total uplift rate that is caused by aseismic uplift, such that $(1 - \alpha)\, U = U_{co}$ and $\alpha U = U_{as}$.

In my zero-dimensional model the change in thickness of regolith (R) during a timestep of the surface of the orogen is defined as

$$\frac{dR}{dt} = \frac{CLRP}{dt} + \frac{W}{dt} - E \qquad \text{Equation 21}$$

where *CLRP (Coseismic Landslide Regolith Production)* is the average thickness (length/time) of weathered material generated by coseismic landslides, all of which is assumed to be transportable, and W (*length/time*) is the thickness of rock weathering caused by all other mechanisms (simply the thickness of material removed from the bedrock when there is no regolith cover). W is included to ensure that erosion can continue even when regolith is not present. In my model weathering does not occur when there is a covering of regolith as the background weathering rates for the study site in the Longmen Shan are unknown. This way of including weathering in the model allows it to be an emerging property rather than a fixed rate. The rate of elevation change (length/time) of the bedrock surface (S_B) can now be described as

$$\frac{dS_B}{dt} = U_{co} + U_{as} - \frac{CLRP}{dt} - \frac{W}{dt} \qquad \text{Equation 22}$$

I can now define the rate of surface uplift again as a combination of the bedrock surface elevation and the regolith thickness:

$$\frac{dS_T}{dt} = \frac{dS_B}{dt} + \frac{dR}{dt} \qquad \text{Equation 23}$$

The model represents the average topographic surface uplift, regolith generation, and bedrock surface lowering for the area (A) of coseismic displacement of the largest possible earthquake for a fault found within a mountain belt. The length of the modelled area (L) is set by the length of the surface rupture on the fault that generates the maximum

earthquake, while the width is the distance to the estimated line of zero strain based upon the dip of the modelled fault (θ) and the focus depth (D) (Li et al., 2014).

$$A = L * (\frac{D}{\theta}) \quad \text{Equation 24}$$

As surface uplift rates for mountain ranges are hard to define (England and Molnar 1990), I set the model to a flux steady state, where U is set to equal the long-term erosion rate (E). For each timestep in the model, an earthquake with M_w>5 is randomly chosen from a power law distribution, and the coseismic rock uplift volume associated with this earthquake is calculated using an empirical scaling relationship (Li et al. 2014) between magnitude and rock uplift volume,

$$log\ (V_u) = 1.06(\pm 0.22)M_w - 8.40(\pm 1.44) \quad \text{Equation 25}$$

where V_u is the volume of rock uplift generated by an earthquake of magnitude M_w. This volume is scaled by α and divided by the model area A to calculate $U_{co.}$ M_w 5 earthquakes are the smallest that regularly produce coseismic landsliding so represent the smallest earthquakes of interest to my study (Marc et al. 2016b). I use an optimising algorithm to fit the uplift produced by equation 26 to ensure the model remains in a flux steady state. The algorithm uses the uncertainty within equation 26 to fit the model parameters so that the average uplift produced during a time step is equal to the long-term erosion rate. The use of the aseismic uplift scaling parameter α has the effect of increasing the time-averaged rock uplift of time steps of small earthquakes and decreasing the rock uplift of large earthquakes.

Regolith is generated in the model based on calculations of bedrock lowering by CLRP and weathering by other mechanisms. I use the scaling between landslide volume (V_l) and earthquake magnitude proposed by (Malamud et al. 2004b) (Figure 50A)

$$log\ V_l = 1.42M_w - 11.26(\pm 0.52) \quad \text{Equation 26}$$

is converted to a depth of landsliding by dividing by the area of the model space (A). The area of the landscape affected by landsliding of the largest earthquakes is greater than the model space, so a scaling is applied based on the landslide density of the Wenchuan earthquake. Alternative models of coseismic landslide volume as a function of seismic moment (Marc et al. 2016a; Robinson et al. 2016) cannot easily be scaled into a zero-

dimensional model space due to their reliance upon earthquake source depth and landscape metrics. These models describe the relationship between earthquake magnitude and total landslide volume as a curve around a hinge magnitude. The shaking produced by an earthquake correlates with the length and width of its surface rupture, however the width (depth) of the rupture is limited by the thickness of elastic crust. At a maximum magnitude (~M_w 6.75) the scaling between earthquake magnitude and shaking changes resulting in a curved relationship between total landslide volume and earthquake magnitude. This has the effect of reducing the importance of large earthquakes in the surface uplift balance. As my chosen model does not include this threshold the larger earthquakes of this model will more erosive than other models. All empirical models relating coseismic landslide volume and earthquake magnitude have large uncertainties in them. I acknowledge these uncertainties by applying a normal distribution of error using the uncertainty bounds on the landsliding volume produced by each earthquake (Figure 50A), reducing the difference between the different models. The total new regolith generated by coseismic landslides is then calculated as the difference between the average depth of landsliding and the average thickness of the regolith.

$$CLRP = (\frac{V_l}{A} - R) \qquad \text{Equation 27}$$

5.3.2 **Model implementation: Longmen Shan**

To apply the model to the Longmen Shan I use a power law relationship of earthquake frequency and magnitude derived from historical earthquake records (Li et al. 2017b):

$$N > M_w = 3.93 - 0.91M_w \qquad \text{Equation 28}$$

N is the number of earthquakes that occurs above a certain magnitude in a year. The smallest earthquake I model is a M_w 5 which occur on average every 5 years. This relationship gives a return time of 1816 years for earthquakes of the same magnitude as the Wenchuan earthquake. Other studies (Densmore et al. 2007; Li et al. 2014; Li et al. 2017a), have proposed a return time of anywhere between 500 – 4000 years for a M_w 7.9 earthquake. I use the uncertainty in the frequency of Wenchuan-sized earthquakes to vary equation 9 to test the impact of earthquake frequency on exhumation and surface uplift. I use an apatite fission track-derived exhumation rate of 0.62 (+0.14 -0.08) mm/yr. (Li et al., 2017a) to represent the long-term sediment flux from the orogen (E). The model area is set

by equation 6, using parameters derived from the Wenchuan earthquake. The length (L) is the surface rupture of the Wenchuan earthquake (240 km), the focal depth (D) was between 14 and 18 km deep and the dip angle ranged between 40 and 90° (Li et al., 2014). These parameters yield an area (A) of 2600 km^2. I run the model for 25 Myr to allow multiple analyses over various timescales and vary α between 0 and 1.

5.3.3 Exhumation calculations within the model

I calculate exhumation for 2 kyr intervals, which is the average time the model takes to exhume 1.2m of rock through the rock-regolith interface given the assumed value of E. This depth is chosen as it broadly representing the recording timescale for cosmogenic radionuclides (Gosse and Philips 2001). Exhumation is calculated as the difference between rock uplift ($U_{co} + U_{as}$) and bedrock surface uplift (S_B) over the recording time. I randomly choose 10,000 2 kyr samples from each 25 Myr run to produce a distribution of exhumation rates. I investigate the change in exhumation rates due to different proportions of coseismic and aseismic rock uplift and varying earthquake frequency and maximum earthquake magnitudes.

5.3.4 Cosmogenic radionuclide calculations

I also calculate the cosmogenic ^{10}Be flux out of the model through time. For each time step I add ^{10}Be atoms to the system using published production rates and attenuation lengths to simulate the depth profile of cosmogenic concentrations (Granger and Muzikar 2001; Balco et al. 2008; Braucher et al. 2011).

$$P_{(z)} = P_0 e^{-z(\rho/\Lambda)} \qquad \text{Equation 29}$$

The production rate (P) of ^{10}Be decreases exponentially with depth below the topographic surface, z, from the production rate at the topographic surface (P_o) based upon the density of the bedrock (ρ) and the attenuation length (Λ). The production rates (atoms per gram per year) and attenuation length (grams per centimetre squared) depend on the radiation being modelled. In my model I simulate spallation (production rate, 5.784 at g^{-1} yr^{-1}, attenuation length, 160 g cm^{-2}), fast muons (production rate, 0.0418 at g^{-1} yr^{-1}, attenuation length, 4320 g cm^{-2}) and slow muons (production rate, 0.014 at g^{-1}yr^{-1}, attenuation length, 1500 g cm^{-2}) and combine them to give a total concentration at depth intervals set by the long term erosion rate (Granger and Muzikar 2001; Braucher et al. 2011). When an earthquake generates regolith the top depth intervals are mixed, and the constant erosion rate is applied to remove regolith from the surface. After a spin up time of 10 kyr, the model tracks concentration of ^{10}Be in the sediment leaving the model. The spin up time is the time

required for the concentrations to reach a stable value which is perturbed by earthquakes. As erosion in the model is constant, and set to the long-term exhumation rate, any change in concentration represents the effect of stochastic EQTL on exhumation.

5.4 Results and discussion

5.4.1 Coseismic landslide regolith production

Within the model, regolith generated by the largest earthquakes can remain on hillslopes for ~1000 years (Figure 50A). The average thickness of new regolith that is produced in an earthquake (expressed as volume per area; i.e., a depth) is a strong function of both the pre-existing depth of regolith prior to new failures, the magnitude of the earthquake, and stochastic differences in the volume of landslides for a given earthquake magnitude (Figure 50B). The primary control on the total landslide volume produced by an earthquake magnitude is the strength of the shaking, with topography and rock strength as secondary factors (Marc et al. 2016a; Valagussa et al. 2019). If shaking can produce similar volumes of landsliding regardless of how much bedrock or regolith is on the hillslopes, landslide deposits in a mountain range with widespread regolith will contain less fresh bedrock, as regolith will make up a greater proportion of material mobilised by the earthquake. As regolith makes up a greater volume of the landslide deposits, less bedrock weathering occurs. This effect will be particularly powerful in areas where large earthquakes occur frequently in similar locations. However, the distribution of earthquake magnitudes exerts a stronger influence on total regolith production through time, as more frequent small earthquakes can only ever weather small depths of regolith from the bedrock (Figure 50B). The decline of coseismic landslide regolith production (CLRP) with existing regolith thickness is reminiscent of soil production functions described for soil mantled landscapes (Heimsath et al. 1997), and by analogy, I term the non-linear relationship between regolith production rate and the average depth of weathering by landslides seen here a *coseismic landslide regolith production function* (CLRPF). However, unlike a "traditional" soil production function, two elements of stochasticity are inherent to a CLRPF. One reflects the role of shielding of the bedrock surface (S_B) from lowering when the regolith layer is thicker than the average depth of the generated landslides (Larsen et al. 2010), and that thickness is dependent on the past history of landsliding in the model. The other reflects the inherent randomness in the size and distribution of the landslides that occur in response to an earthquake of a given magnitude, i.e., within equation (27).

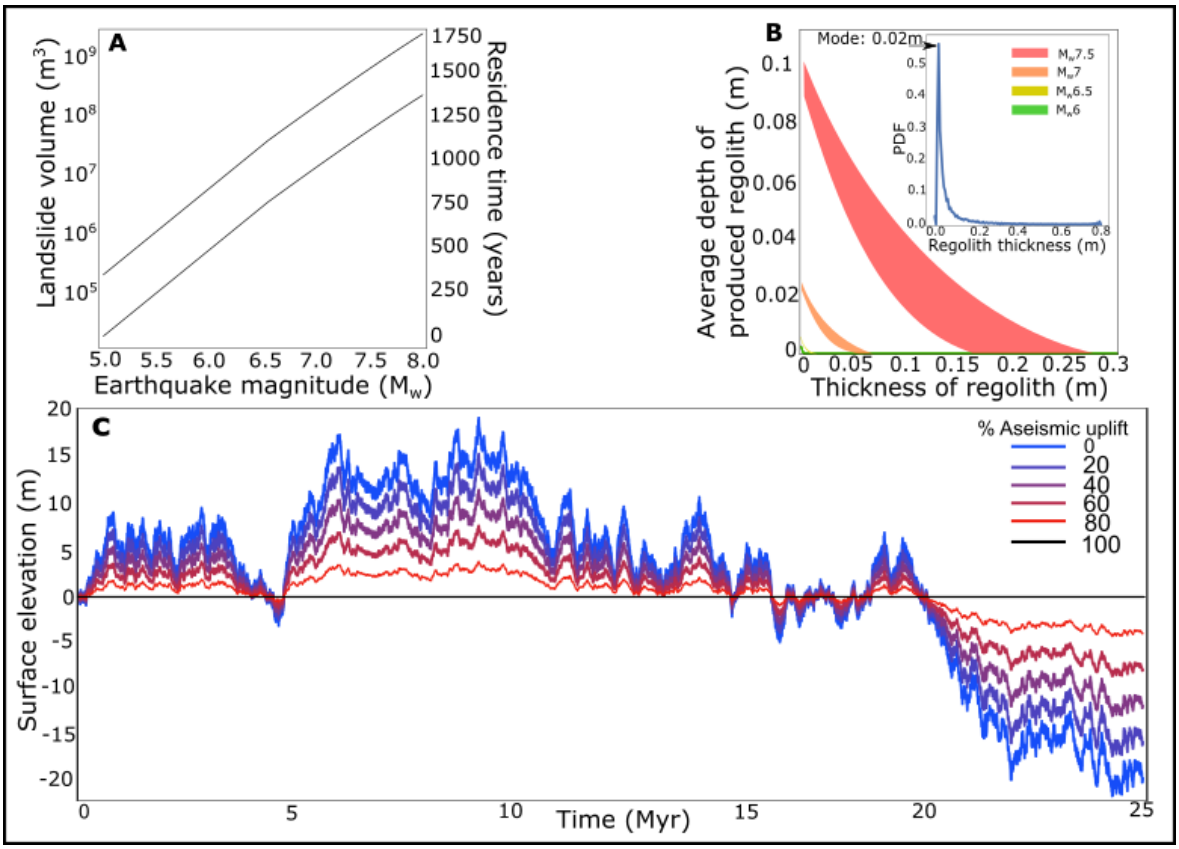

Figure 50 The average depth of regolith produced by an earthquake is impacted by the earthquake magnitude and the thickness of regolith that is on the hillslope before the earthquake occurs . (A) Scaling of landslide volume with magnitude from Malamud et al., 2004 and the average residence time of landslide sediment in the Longmen Shan based upon an erosion rate of 0.62mm/yr. The two lines represent the minimum and maximum volumes of landsliding generated, within the bounds on equation 27. (B) Variability of regolith production, expressed as volume per area, with existing depth of regolith on the hillslope, for four representative earthquake magnitudes. Coloured areas represent the variability of the landslide volume produced by an earthquake, randomly sampling within the bounds of equation 27. These coseismic landslide regolith production functions (CLRPF) emerge from the model rather than being set in advance, and the variability at each magnitude is driven by noise inherent in the relationship between magnitude and landslide size (equation 27). Inset shows the probability distribution function for regolith thickness across the whole model run, integrating the effects of the CLRPF through time. A small but nonzero spatially averaged modal regolith thickness persists, but significantly larger thicknesses regularly occur. (C) Variability of surface elevation through time for model runs with identical earthquake sequences, but with varying additional proportions of aseismic uplift. The assumption of steady state prevents any long-term permanent uplift, and so all variations in surface elevation are driven by the sequence of earthquakes and changes in regolith thickness. Increasing the aseismic contribution to uplift reduces the uplift of large earthquakes, resulting in much less variable surface uplift and therefore exhumation.

As expected, total seismic regolith production is dominated by the largest earthquakes, which produce the largest mean landslide volumes (Malamud et al., 2004) (Figure 50B). Summing through time, earthquakes produce 42% of the total regolith generated by the model; M_w>7 earthquakes account for ~65% of the total earthquake-generated regolith and

so 27% of the total regolith production. However, because smaller earthquakes occur often but produce little regolith, allowing the layer to thin, the time- and spatially-averaged regolith layer is predominantly thin – the modal thickness is only 0.02m, and the mean is 0.03m (Figure 50B inset). Thus, the model shows that although mountain belt regolith cover appears thin almost all the time, at times it can be thick enough to severely affect the short-term exhumation rates of the mountain range. The Longmen Shan is primarily classified as a bedrock landscape with little storage, but significant volumes of sediment remain in the mountain range after the earthquake, in a similar way as simulated by the model (Zhang et al. 2016; Fan et al. 2018a).Variability in surface uplift through time (Figure 50C) is affected by the pre-earthquake regolith thickness and therefore the sequence of earthquakes which occur before it. Where large earthquakes are closely spaced in time, pre-existing regolith can limit weathering of the bedrock surface, encouraging uplift of the topographic surface. In catchments close to active faults the bedrock is likely to be heavily fractured and the shaking is more intense, producing larger landslides with greater densities (Meunier et al. 2013; Marc et al. 2016a; Valagussa et al. 2019). If the regolith is not fully removed from these catchments in between earthquakes it is possible that the CLRPF may encourage greater surface uplift. In my model the regolith produced by earthquakes is spread evenly across the landscape, which does not occur in reality. Even in the most impacted catchments in Wenchuan landslide density is rarely above 10% per km^2, suggesting that remobilisation of landslide regolith on the hillslope may be rare unless the regolith can remain in the catchment for multiple earthquake cycles (Dai et al. 2011; Parker et al. 2011; Marc et al. 2015; Parker et al. 2015). The remobilisation of previous coseismic landslide regolith is, likely to be a local effect mainly impacting catchments close to active fault belts. Ultimately, this interaction between surface uplift and regolith depth is controlled by 1. the time between earthquakes; 2. the magnitude of the previous earthquake; and 3. the rate of regolith removal. The closer together, in both time and space, large earthquakes occur and the slower regolith is removed from hillslopes, the greater the impact of the CLRPF on the surface uplift of a mountain range.

5.4.2 **Regolith generation and volume budgets of earthquakes**

My model demonstrates that the contribution of earthquakes to the uplift and weathering budgets of mountains varies with earthquake magnitude, frequency, and the relative contribution of aseismic weathering and erosion, i.e., erosion or weathering not directly related to earthquakes such as rainfall triggered landsliding or chemical weathering. When coseismic rock uplift is the dominant uplift mechanism, I can classify four distinct landscape response styles at different earthquake magnitudes (Figure 51A and C zones 1-

4). On average, an earthquake of magnitude M_w<5.6 lowers the topographic surface (S_T). Here, the erosion of regolith (E) out of the model space is greater than the rock uplift produced by the earthquakes (Zone 1 in Figure 51A). For earthquakes with magnitudes 5.6 < M_w < 7.6 the bedrock surface (S_B) rises because the rock uplift rate is greater than the typical regolith generation rate (Zones 2-3). The regolith thins because the change in the regolith thickness due to CLRP is less than the erosion rate (E) out of the model (Zone 2). Conversely the change in regolith thickness due to CLRP exceeds erosion rate in earthquakes with magnitudes M_w>6.4 so the regolith layer increases in thickness (Zones 3-4). The largest earthquakes with M_w >7.6 lower the bedrock surface due to the large volumes of regolith produced (Zone 4). However, much of the regolith is not removed before the next earthquake resulting in a net topographic surface uplift, primarily due to thickening of the regolith. For a theoretical purely aseismic uplift scenario, where earthquakes produce landslides but do not create rock uplift (earthquakes produce only horizontal motion, this scenario is not realistic but acts as an extreme end member), earthquakes with M_w>6.5 would cause bedrock surface lowering while smaller earthquakes would permit bedrock surface uplift due to low CLRP. Earthquakes with M_w>6.5 produce a thick layer of regolith which can persist until the next earthquake, limiting bedrock surface weathering and resulting in net uplift of the bedrock surface.

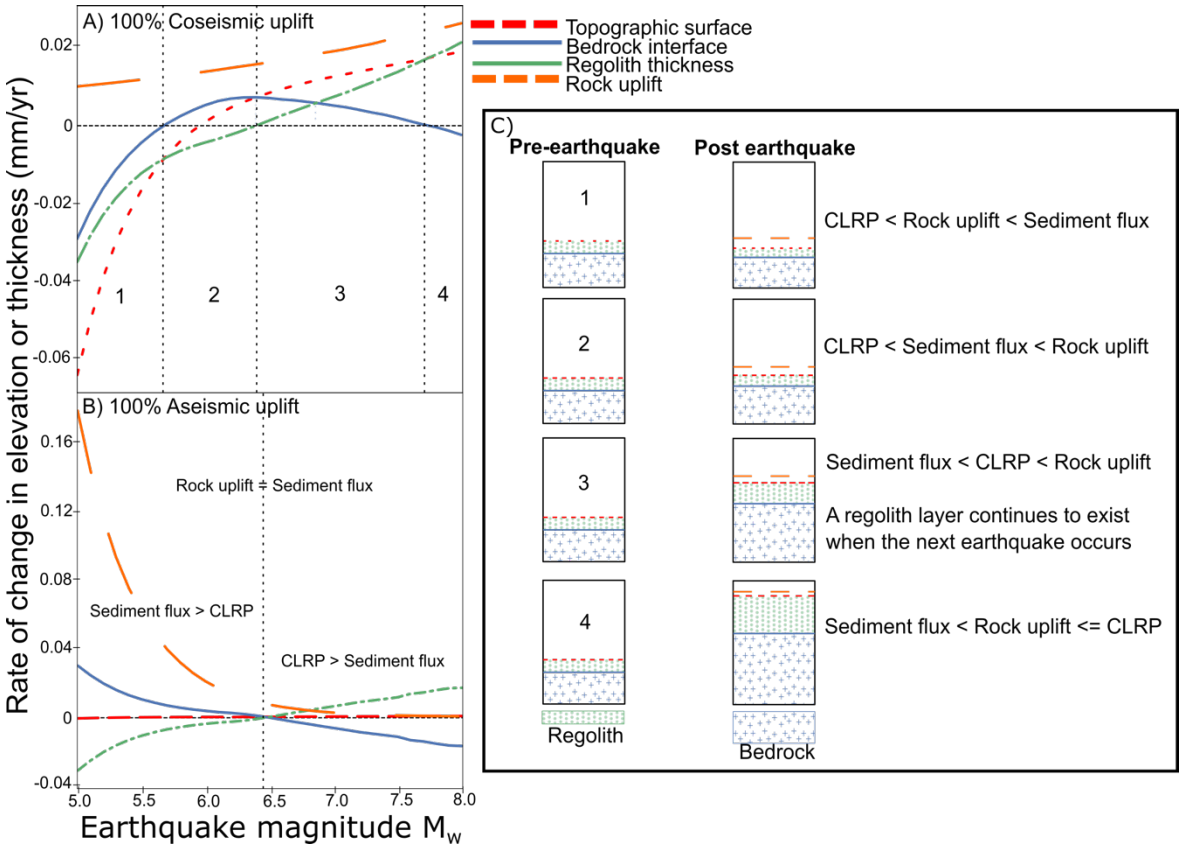

Figure 51 Interplay of changes to the modelled rock uplift rate, the topographic and bedrock surface uplift, and the resulting regolith thickness through time, classified according to earthquake magnitude. The total

bedrock and topographic uplift produced by each earthquake magnitude through the model run is summed up and divided by the run time to produce a rate. A) represents a run with 100% coseismic uplift while B) is purely aseismic. Each time a recorded surface intersects the horizontal axis I separate the chart into a zone which is further described in the text and panel C).

5.4.3 **Earthquakes and exhumation**

I explore how earthquakes affect exhumation through direct calculation of exhumation of rock at the bedrock surface (S_B) relative to the topographic surface. There is very little (~1%) variability in erosion rates in model runs with maximum earthquake magnitudes of M_w<5.0. However, the introduction of stochastic weathering of many tens of cm of the bedrock surface by earthquakes with M_w>7 introduces variability in exhumation. When large earthquakes are present, exhumation rates have a standard deviation of 0.055-0.081 mm/yr. (9-14% of the long-term exhumation rate), and a range of 0.77-0.89 mm/yr., with the lower figures reflecting a greater contribution of aseismic uplift (Figure 52A and B). Decreasing the return times of Wenchuan-like earthquakes from 4000 yr. to 500-years produces more variable distributions of exhumation rates, with the standard deviation of exhumation rate increasing from 0.044 mm/yr. (7% of long-term average) to 0.076 mm/yr. (12% of the long-term average) (Figure 52C). Taken together, my model results suggest that up to 14% of the variability in a sample of exhumation rates from a single geographical region could be associated with the time since the last large (M_w>7.0) earthquake. However, this variation may only be seen in exhumation or surface uplift records with recording times of less than 1000 years (Figure 53A). Pre-Wenchuan earthquake measurements of cosmogenically-derived erosion rates are between 40% and 60% lower than low-temperature thermochronometrically derived exhumation rates (Ouimet, 2010). Stochastic exhumation of low-concentration bedrock by EQTL may explain some of that difference.

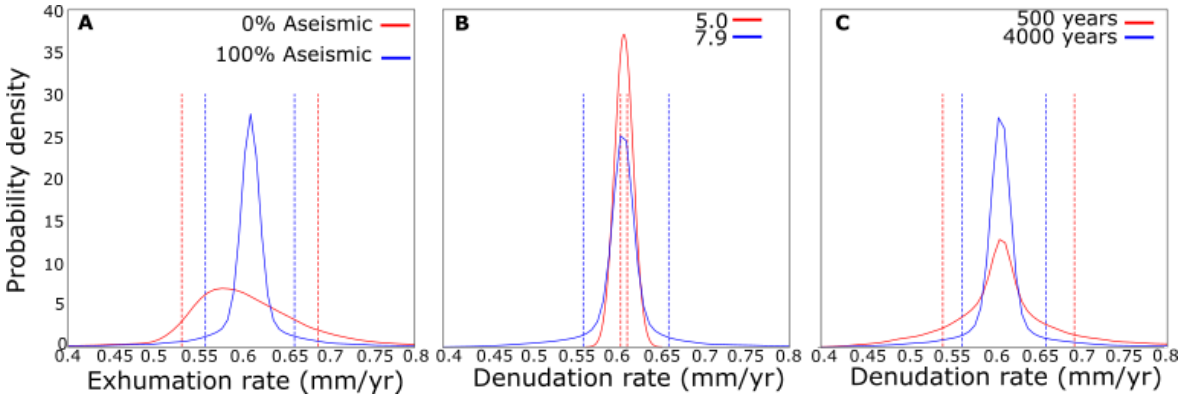

Figure 52 Kernel density plots (bandwidth of 0.01) of exhumation and denudation rates in various scenarios. Dashed lines indicate the position of the mean +/- the standard deviation of the distribution. Each curve is made up of 10,000 samples taken from their respective model runs. A) Exhumation rates in different uplift

regimes. B) Denudation rates while varying the maximum earthquake magnitude in a run, the run with a maximum magnitude 5 has only earthquakes of a magnitude 5. C) Denudation rates while varying the frequency of Wenchuan size earthquakes from every 500 to every 4000 years.

Cosmogenic radionuclides provide a record of potential earthquake-driven changes in exhumation because they have a relatively short averaging time that is close to the frequency of large earthquakes in many mountain belts. My modelling results demonstrate the scale of stochastic variability in surface uplift and exhumation. I extend this analysis by simulating cosmogenic concentration in the model to estimate the potential impact of a large earthquake on both the cosmogenic concentration through time and the distribution of cosmogenic concentrations that are likely to be measured. I assume each earthquake thoroughly mixes the regolith down to its average weathering depth. The cosmogenic analysis (Figure 53B) shows that immediately after a large earthquake, mixing of low concentration bedrock material with higher concentration regolith lowers the concentration of radionuclides exiting the model. Regolith exiting the mountain range has a lower cosmogenic nuclide concentration for 200-300 years after the earthquake; after this period of low concentrations there is a peak of concentration higher than the long-term average before a rapid return to the long term average concentration (Figure 53B). In the case of a representative magnitude M_w~8 earthquake, the concentration falls initially by around one third. However, the process of mixing also increases the concentration of nuclides close to the regolith-bedrock interface compared to the values before mixing, so that as the regolith is slowly eroded through time the lower half releases concentrations *greater* than the long-term average. Therefore, in landscapes with frequent M_w>7 earthquakes and regular long-term storage of regolith, it is possible to record more variable cosmogenic concentrations than might be expected, including positive as well as negative excursions from the long-term mean (Figure 53B).

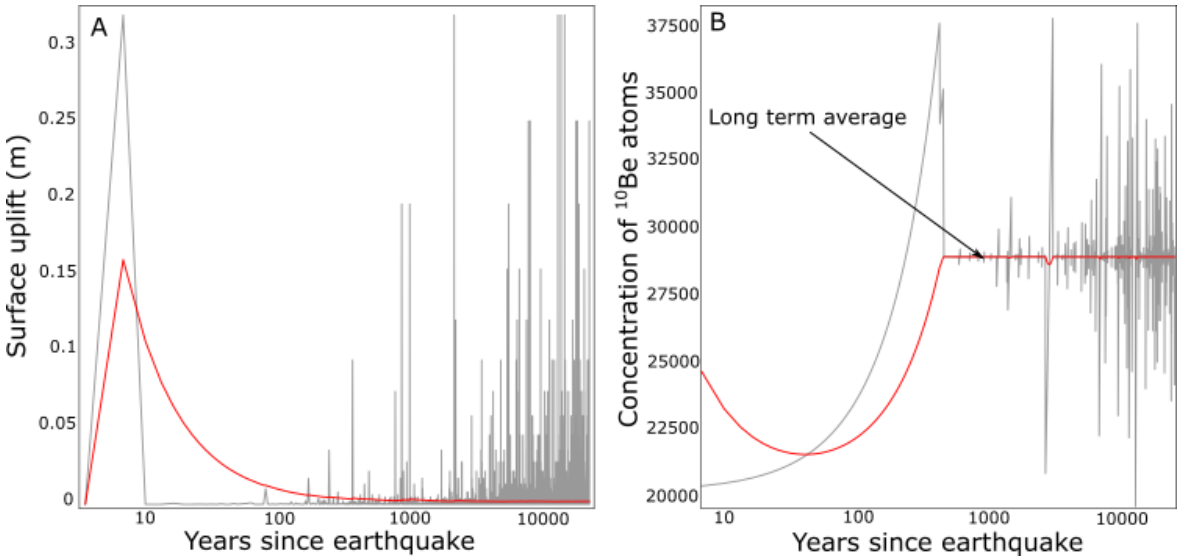

Figure 53 Variability of (A) topographic surface uplift and (B) the recorded concentration of cosmogenic nuclides leaving the orogen after a representative magnitude 8 earthquake within the model run. Red lines are the mean for the elapsed time since the earthquake while the grey are the real time concentrations.

These modelling results provide testable predictions of the exhumation-related changes to cosmogenic concentration caused by large earthquakes. Hence, I look to examine whether the predicted variability might represent some of the variability associated with cosmogenic erosion rates in seismically active areas using a global dataset compiled by Harel et al., (2016). Harel et al. (2016) collated detrital cosmogenic ^{10}Be concentrations for 59 geographical areas, separated into areas of similar climates, and recalculated the erosion rates using consistent production rate and shielding corrections. I limit the sampling to those sites with >18 measurements and basins larger than 10^5 m^2 to limit sampling bias (Niemi et al. 2005; Dingle et al. 2018), I compare the probability density distribution of erosion rates from within those geographic regions to seismicity, as represented by the 475 year return peak ground acceleration (PGA) derived from a global seismic hazard map (Giardini et al. 1999; Harel et al. 2016) (Figure 54A). Due to the size of the geographical areas there may be multiple seismic hazard levels recorded; I simply use the mean value to classify the area. The use of a single number to characterise a large area can underestimate the potential PGA. While a single number may not accurately describe the entire area, it does allow the comparison of the variability of denudation rates with seismic hazard. I crudely classify the regions as dominantly coseismic or dominantly aseismic: regions with thrust faults (identified from a literature review) and erosion rates greater than the median are deemed coseismic, while slowly eroding regions with no thrust faults are aseismic. “Mixed” regions are those that do not fall under either of these classifications. Coseismic landscapes, as expected, have higher average cosmogenically-determined erosion rates with higher standard deviations (Krustal-Wallis H-test statistic=14.14, p-value=0.00017)

(Figure 54A&B). Relief is a major control on erosion rates, with steeper catchments having higher erosion rates than shallower ones (Montgomery and Brandon 2002). The most seismically active mountain ranges are also among the most varied in relief as they have some of the steepest catchments in the world. Therefore, I need to test whether variability in erosion rates is more closely related to variation in catchment steepness or the seismicity of the area. Within the database compiled by Harel et al., 2016 they include a normalised channel steepness index which I use to compare the impact of catchment steepness on erosion rate. The channel steepness index equation is defined by

$$M_x = \left(\frac{E}{K{A_0}^m}\right)^{\frac{1}{n}} \qquad \text{Equation 30}$$

where M_x is the steepness index, E is the erosion rate, K is the erodibility coefficient, A_0 is a reference area of 1m^2 and m and n are empirical constants. The index is normalised by assuming fixed values for m and n (Harel et al. 2016). I would expect that in areas with highly variable steepness indexes the erosion rates are also more variable. I find that while areas with higher seismicity have more variable erosion rates, the variation in erosion rates correlates much more closely with the variation in steepness index (Figure 54B&C). Steeper basins in tectonically active mountain ranges are more susceptible to coseismic landsliding (Marc et al. 2016a; Li et al. 2017a) so will have more variable denudation rates through time, depending on the residence time of the landslide regolith and the frequency of earthquakes, than shallower basins. Landscapes with more variation in basin relief could enhance the temporal perturbations in denudation rates produced by earthquakes, but the contribution of tectonics to long term variation is difficult to isolate.

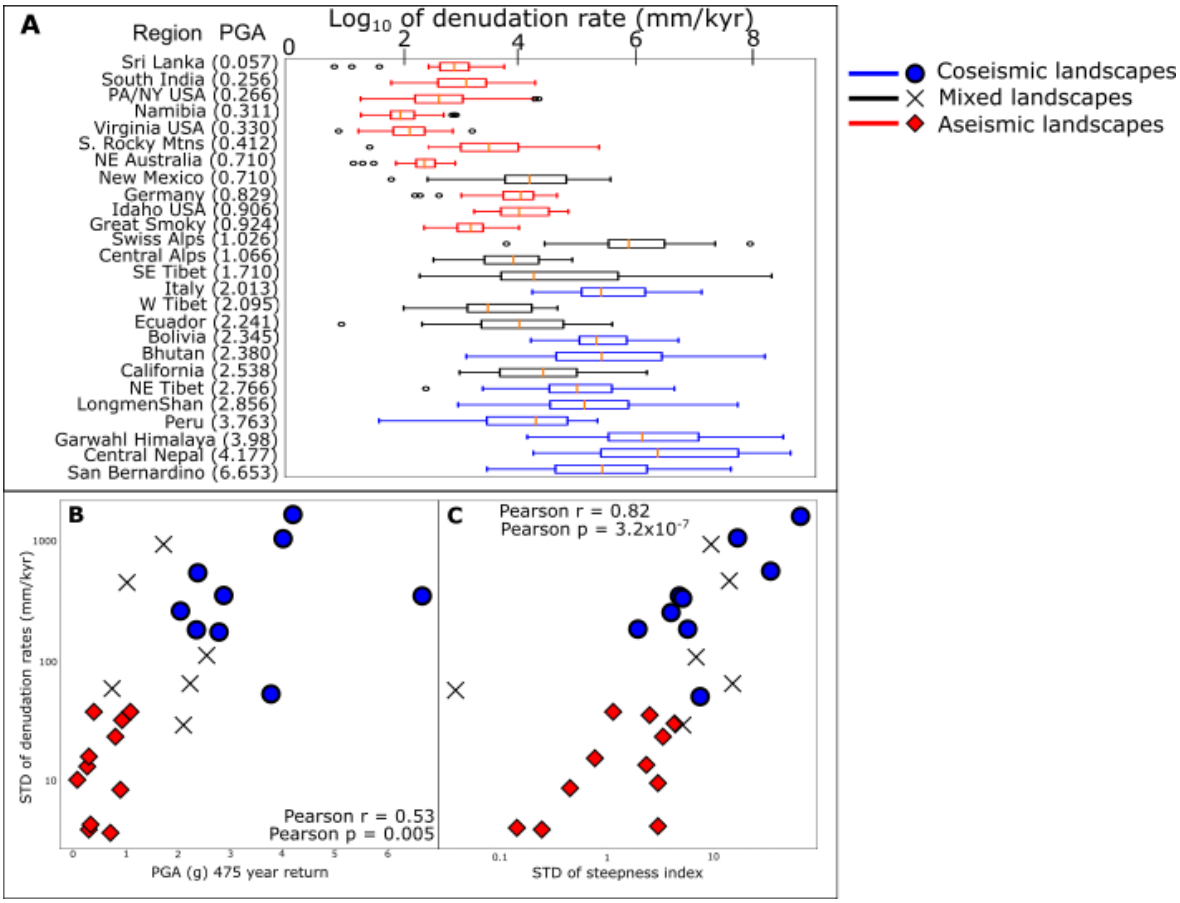

Figure 54 Reanalysis of detrital cosmogenic radionuclide derived denudation rates for mountain belts around the world compiled by Harel et al (2016), in the context of peak ground acceleration and tectonic environment. (A) A box plot indicating the median (central orange line), quartiles (end of box) and the range ('the whiskers') of denudation rates in the analysed localities ordered by their average seismicity (in brackets), defined as the maximum Peak Ground Acceleration (PGA) of a 475-year return period. Points indicate values outside the range, ±1.5 times the inter-quartile range. (B) Standard deviation (STD) of denudation rates for each mountain belt against seismicity represented by the 475-year return PGA (ms-2). (C) Standard deviation of denudation rates for each mountain belt compared to the standard deviation of steepness indexes. The areas of highest variability are found in steep, tectonically active mountain ranges.

I also explore the averaging time required to reach the mean exhumation rate in model runs with different contributions from seismic and aseismic uplift. After a large earthquake that produces tens of centimetres of instantaneous weathering of S_B, exhumation rates measured with different averaging times converge to the long-term mean rate within hundreds to thousands of years (Figure 53A). Bedrock surface exhumation rates are impacted by both surface uplift and lowering rates so as a result the time scale of the perturbation is impacted by the dominant form of uplift in the mountain range. As a result, the more dominant coseismic uplift is in a landscape, the longer the recording time needs to be before a reliable exhumation record can be made. Landscapes with more frequent earthquakes have more variable exhumation rates which require longer averaging times to achieve accurate measurements of the long-term average exhumation rate. Regardless of the frequency of

earthquakes in a mountain range, the events of the greatest magnitude remain uncommon while being the dominant contributors to weathering. Hence the relationship between exhumation rate and averaging time is consistent with the Sadler effect that has been described for sedimentary systems (Schumer and Jerolmack 2009). Unlike sedimentary systems, where it is possible to measure sedimentation rates from timescales of seconds to millions of years, there are few measures of exhumation that we can use and many of these have long averaging times. Thermochronometric methods average across timescales of 10^5-10^7 years, much longer than the recurrence times of individual earthquakes. There is a possibility that cosmogenic radionuclide analysis record individual earthquakes, where earthquake-triggered landslides weather bedrock that has a low cosmogenic concentration (West et al. 2014; Wang et al. 2017), although enhanced erosion during and immediately after an earthquake complicate the cosmogenic signal in practice.

Despite representing close to half of the weathering flux of mountain belts, stochastic earthquakes still remain substantively missing from our models of the development of mountain belts. The modelling here demonstrates that stochastic uplift and exhumation by large earthquakes is likely to be averaged away across the timescale of most thermochronometers, with the variability in uplift and exhumation representing around 15% of the average exhumation rate. Even when a large earthquake occurs at the edge of a mountain belt, as has occurred in the Wenchuan region, the variable exhumation signal is further shredded by sediment transport by floods and debris flows, such that even sinks that are within 40 km of the epicentre show limited immediate evidence for large earthquakes (Zhang et al. 2019). This result along with my model demonstrates the importance of understanding the processes by which and the time taken for landslide sediment to be mobilised out of catchments. Without improved understanding of the cascading nature of sediment transport from catchments it is unlikely we will be able to identify earthquakes other than within smaller basins or sinks immediately adjacent to the epicentre (Howarth et al. 2012). Large basins (greater than 10,000 km^2) have been shown to be large enough to average out the perturbations in cosmogenic radionuclide concentrations caused by large landsliding events (Dingle et al. 2018; Marc et al. 2019). While the largest basins are able to offer reliable estimates of long-term erosion rates, the detrital cosmogenic nuclide concentrations from smaller basins will be more affected by bedrock landsliding caused by earthquakes. Therefore, smaller basins could be suitable targets to recognise variations in erosion rates due to earthquakes. My model suggests that the impact of a large earthquake is not necessarily big enough to perturb the denudation rate of an orogen for the whole of a cosmogenic nuclide recording time. The combination

of averaging times, shredding, and the relative contributions of large earthquakes to long term exhumation rates help us to understand the lack of clear signatures for single earthquakes in sedimentary or exhumation records.

5.5 Conclusions and implications

My simulations show that the regolith generated by large earthquakes can reduce the rate of weathering and exhumation of rock due to its potentially long residence time on hillslopes. Reducing exhumation rates also increases the uplift rate of the bedrock surface, but these effects are small when compared to the role of the magnitude and frequency of earthquakes. These results demonstrate that background tectonic processes and rates are the dominant control on surface uplift, while the more important role for large earthquakes is their control on weathering. Small earthquakes contribute very little to both uplift and weathering resulting in below average rock exhumation being recorded if a large earthquake does not occur during the averaging time of the exhumation record. While large earthquakes produce higher than average rock exhumation rates, the slow removal of regolith from the orogen reduces the magnitude and timescale of the signal. The relatively long timescales of exhumation records prevent the recording of orogen-scale variation in exhumation due to a single earthquake. A better understanding of the controls on bedrock weathering by earthquake triggered landslides is required to identify signals of earthquakes in sedimentary records. Higher resolution exhumation records and the growing recognition of the complex nature of exporting landslide sediment from mountainous catchments will help to explore this problem.

Chapter 6 Discussion and conclusion

6.1 Summary

Through this thesis I have investigated the immediate aftermath of the coseismic landsliding produced by the 2008 Wenchuan earthquake and put it into the context of long-term landscape evolution.

In chapter 3 I detailed the construction of a sediment budget of the earthquake and the 10 years following it. Through this I identified that less than 12.5% of the sediment produced during this time had left the hillslopes (Figure 29). Of the sediment that had been remobilised off the hillslopes, over 50% was transported via debris flows (Table 5). The activity of debris flows is very transient, a significant decrease in the frequency of these events is seen within the 10-year study period (Figure 30).

In chapter 4 I investigated the spatial-temporal evolution of the coseismic landslide deposits and what this tells us about debris flow triggering after the earthquake. The smallest landslide deposits along the ridges are initially preferentially eroded by debris flows (Figure 37). These deposits contribute the most to the overall volume deposited into the channel network during this period of preferential erosion. Through time the frequency at which the smallest deposits higher up on the hillslope are remobilised decreases rapidly so that the preference for small deposits diminishes by the end of the observation period. In 2018 reactivation occurs close to the channel heads, suggesting reactivation becomes more difficult through time as hydrology becomes more important through time (Figure 34). Susceptibility modelling of the landslide deposits also suggests the probability of reactivation changes through time due to a change in the physical conditions of the deposits, most likely an increase in the internal friction angle and the hydraulic conductivity. These changes could occur as a result of preferential mobilisation of fine sediment which drives compaction of the deposit and enhanced conductivity of some areas of the deposit.

Finally, in chapter 5 I investigated the long-term impacts of earthquakes on mountain ranges and whether earthquakes can be recognised in sedimentary or exhumation records. Using a 0-dimensional landscape volume budget model I demonstrated that in catchments of consistent high landslide density remobilisation of coseismic landslide regolith can protect bedrock from erosion potentially increasing surface uplift (Figure 50). While coseismic sediment can initially be recorded in detrital cosmogenic nuclides sampling, through time the concentration difference decreases, and the perturbation becomes impossible to recognise within 1000 years (Figure 53). The long-term storage of coseismic

sediment may prevent earthquakes from being recognised in all but the most local sediment sinks and exhumation proxies with averaging times less than 1000 years.

6.2 Overview and significance

Through preparing the first complete sediment budget of an earthquake I have demonstrated the importance of debris flows to remobilising landslide generated sediment following earthquakes. Fluvial processes, while potentially becoming more important through time, remobilise very little of the sediment deposited into the channels and cannot impact the hillslope deposits. Partial sediment budgets, such as those of fine suspended sediment (Hovius et al. 2011; Wang et al. 2015; Wang et al. 2017), have missed the importance of these mass movements in transferring sediment from the hillslope into tributary and major rivers. Debris flows can remobilise sediment from anywhere along the hillslope into the channel network without the need for a direct connection. Previous modelling has suggested that fluvial incision is significant enough to mobilise most of the volume of landslide deposits out of catchments within 100 years, if it is deposited directly into the channel network (Croissant et al. 2017). However, I have seen little evidence for the direct fluvial reworking of coseismic landslide deposits in the Longmen Shan. Similar to observations in Taiwan (Yanites et al. 2010; Yanites et al. 2018) channels are prone to aggradation suggesting deposition rates overwhelm the transport capacity of the channel network in many locations. If channels are transport limited, they require large discharge events to remobilise the sediment, which typically produce debris flows when there is significant volumes of sediment which can maintain the required pore pressures and be entrained (Bovis and Jakob 1999; Jakob et al. 2005; Bennett et al. 2013; Bennett et al. 2014). Once the majority of this sediment has been evacuated from the catchments debris flows will stop occurring. For as long as the sediment remains, or is replenished via enhanced sedimentation rates from the hillslope, debris flow frequency in channels will remain enhanced. Once the debris flow frequency decreases it can be expected that the fluvial entrainment of sediment will be the main process, however this is likely to erode channel deposits at a significantly slower rate (Croissant et al. 2017; Major et al. 2019). Without debris flows remobilising sediment from hillslope deposits there is no obvious process to remove these deposits from the hillslope. These deposits could be remobilised during future earthquakes or intense monsoons or could be broken down via chemical weathering and converted into soil. If significant volumes of sediment remain in the catchments for extended periods of time it is possible that most of the sediment in the Longmen Shan was formed during earthquakes with climatic events primarily remobilising sediment rather than generating it through bedrock landsliding.

While debris flows are incredibly important for remobilising and removing the coseismic sediment from the hillslopes our understanding of their triggering is poor. I have shown that the internal conditions of landslide deposits can change rapidly following an earthquake making predictions and risk assessments of debris flow frequency and magnitude difficult. Debris flow triggering probability is commonly defined in risk assessments by rainfall intensity-duration thresholds (Guzzetti et al. 2008; Ma et al. 2017; Frank et al. 2018). The rainfall intensity-duration threshold of a catchment are closely linked to the sediment properties of the landslide deposits and its location in the catchment (Jakob et al. 2005). The intensity – duration threshold of debris flow triggering decreases significantly after an earthquake but rapidly rebounds to the pre-earthquake relationship within 10 years (Lin et al. 2004; Guo et al. 2016a; Ma et al. 2017). We lack understanding on exactly what controls the rainfall intensity-duration threshold and how it changes through time making its use as a predictive tool difficult. Along with the hillslope deposits reactivating less through time, the increase in the volume of sediment in the steep channels of the catchments make channel triggered debris flows more likely through time (Zhang and Zhang 2017). These debris flows have a different triggering mechanism and so will require separate risk assessment modelling (Prancevic et al. 2014). To accurately model the triggering of debris flows through time we need to include the change in the properties and location of the source sediment through time. These two factors need to be constrained by in field observations and rapid and frequent mapping of sediment locations after the earthquake.

I have shown that while large earthquakes can be constructive producing surface uplift, their primary role is erosive producing huge volumes of sediment which can potentially remain in the orogen over multiple earthquake cycles. While the existence of long term storage in mountain ranges has long been recognised, particularly in large landslide deposits and fluvial terraces (Pratt et al. 2002; Korup et al. 2004; Straumann and Korup 2009; Blöthe and Korup 2013; Stolle et al. 2017), I have shown that significant volumes of sediment can remain on hillslopes and they have the potential to be remobilised. Tectonically active mountain ranges are commonly assumed to be bedrock landscapes with steep slopes unable to maintain regolith cover (Montgomery and Brandon 2002; Ouimet et al. 2009). However, my results show that this assumption is too simplistic and can lead to the over estimation of tectonic erosion rates in mountain ranges. The long-term storage of coseismic sediment also prevents the easy recognition of single large earthquakes across orogens and geochemical records. Many models of the impact of earthquakes upon cosmogenic nuclide concentrations assume that the sediment is deposited directly into the

channel network producing a huge perturbation in the recorded concentrations leaving the catchments (Niemi et al. 2005; Yanites et al. 2009). My results suggest that a maximum of 13% of the coseismic landslide volume is deposited into streams in the 10 years after the earthquake. Two years after the earthquake samples of channel sediment showed a decrease of up to 10x of the pre earthquake ^{10}Be concentrations in even the largest catchments (West et al. 2014). However this perturbation decreases rapidly and is only expected to last for up to 20 years after the earthquake, well before significant volumes of sediment are to be removed from the catchments (Wang et al. 2017). This timescale of perturbation is considerably smaller, by several orders of magnitude, than model results which do not simulate storage (Niemi et al. 2005). Storage of coseismic sediment and slow remobilisation can lead to significant underestimation of coseismic erosion and prevents the recognition of earthquakes in well mixed geochemical records.

6.3 Further work

6.3.1 **Landslide deposit structure**

The internal structure of landslide deposits is very poorly understood and lacks constraints. Catchments with more coseismic landsliding within them tend to have more debris flow activity after the earthquake, however as the triggering process of the debris flows is not known, predictions of debris flow frequency cannot be derived from landslide mapping. The rapid decrease in debris flow triggering after the earthquake is also unknown but likely linked to a change in the properties of the landslide deposits. During chapter 4 I showed that many landslides did not reactivate and generate debris flows despite being in very similar locations to landslides which did fail. The deposits which did not fail could have different sediment properties to those which did fail but this cannot be determined without in situ measurements. Similarly, without observations of debris flow triggering the exact initiation process and its controlling variables cannot be identified or modelled. Studying the landslide deposits in the field rapidly after the earthquake would provide a base line with which older deposits can be compared to identify the nature of any changes which occur. Long-term experiments in flumes focusing on how landslide deposits change through time and how this may be affected by varying degrees of compaction and grain size distributions will also provide useful context for risk assessments and debris flow triggering.

6.3.2 **Depth of regolith across hillslopes**

A key observation of my sediment budget of the Wenchuan earthquake is that much of the sediment produced by the earthquake remains on the hillslope for an extended period of

time. Modelling suggests that this time can be longer than the return times of major earthquakes raising the possibility of remobilising sediment for multiple earthquakes. Measuring the depth of regolith across hillslopes in tectonically active regions would allow for the identification of stable deposits, which when combined with dating would help constrain the frequency-magnitude of landslides in a mountain range. Regolith depth is a notoriously difficult parameter to constrain due to the long and intensive nature of the fieldwork required. However increased resolution of DEMs and aerial and satellite imagery may be able to help identify landslide deposits. Ground penetrating radar and resistivity studies can also help to recognise the average depth of regolith across the hillslope and help to constrain the hydrology of the hillslope. Currently the impact of regolith in mountain ranges on earthquake landslide magnitude – frequency and total volume is poorly understood. Identifying likely areas of remobilising regolith will help to further constrain the impact of earthquakes on mountain ranges.

6.3.3 **Improved debris flow triggering models**

All three of the slope stability models I tested in my thesis performed poorly in predicting the triggering of debris flows. While they accurately identified many deposits as unstable more were identified as unstable than failed. The poor performance may be due to the lack of consideration of positive pore pressures in the models. Debris flows require positive pore pressure and localised liquefaction to fail, something which many models do not include. Positive pore pressures form as part of the failure process as result of shifting grains within a material or a precipitation wave. These models would require knowledge of both the material properties of the sediment and the precipitation to identify pressure waves resulting from either grains or precipitation. A model like this would be the link between a susceptibility and a prediction model and would have the potential to be useful for early warning systems and risk assessments.

6.3.4 **Conclusions**

This thesis demonstrates the massive erosional power of large earthquakes and the complicated nature of understanding their long-term effects on mountain ranges. The coseismic landslide deposits generated by an earthquake can take 1000s of years to be evacuated from the orogen. The long and currently unconstrainable residence time of landslide deposits is due to the reliance on debris flows to remove sediment from hillslopes and deposit sediment into the major river system. The triggering of debris flows in coseismic landslide deposits is poorly understood and changes through time due to changing internal material properties of the deposits. These changes cause a shift of

preferential erosion from the smallest deposits along the ridges to any deposit near the channel network. Identifying this trend could help aid the development of risk assessments by highlighting the importance of focusing on the hillslope immediately after the earthquake before tracking the evolution of the channel deposits after the first widespread debris flow events. Finally, the long-term storage of coseismic landslide regolith can cause a decrease in exhumation rates due to remobilisation in locations with high landslide density and a corresponding increase in surface uplift. The storage of sediment also prevents the easily recording of single earthquakes in geochemical or sedimentary records.

Chapter 7 References

Adams, J.M. et al. 2017. The Landlab v1.0 OverlandFlow component: A Python tool for computing shallow-water flow across watersheds. *Geoscientific Model Development* 10(4), pp. 1645–1663. doi: 10.5194/gmd-10-1645-2017.

Andermann, C. et al. 2012. Connecting source and transport: Suspended sediments in the Nepal Himalayas. *Earth and Planetary Science Letters* 351–352, pp. 158–170. Available at: https://linkinghub.elsevier.com/retrieve/pii/S0012821X12003512.

Anderson, M.G. and Lloyd, D.M. 1991. Using a combined slope hydrology-stability model to develop cut slope design charts. *Proceedings - Institution of Civil Engineers. Part 2. Research and theory* 91, pp. 705–718. doi: 10.1680/iicep.1991.17486.

Anderson, R.S. and Anderson, S.P. 2010. *Geomorphology: the mechanics and chemistry of landscapes*. Cambridge: Cambridge University Press. Available at: http://ebooks.cambridge.org/ref/id/CBO9780511794827.

Ardizzone, F. et al. 2002. Impact of mapping errors on the reliability of landslide hazard maps. *Natural Hazards and Earth System Sciences* 2(1–2), pp. 3–14. doi: 10.5194/nhess-2-3-2002.

Avouac, J.P. 2007. Dynamic Processes in Extensional and Compressional Settings – Mountain Building : From Earthquakes to Geological Deformation. *Treatise on Geophysics* 6, pp. 377–439.

Balco, G. et al. 2008. A complete and easily accessible means of calculating surface exposure ages or erosion rates from 10Be and 26Al measurements. *Quaternary Geochronology* 3(3), pp. 174–195. doi: 10.1016/j.quageo.2007.12.001.

Bareither, C.A. et al. 2008. Geological and physical factors affecting the friction angle of compacted sands. *Journal of Geotechnical and Geoenvironmental Engineering* 134(10), pp. 1476–1489. doi: 10.1061/(ASCE)1090-0241(2008)134:10(1476).

Benda, L. and Dunne, T. 1997. Stochastic forcing of sediment routing and storage in channel networks. *Water Resources* 33(12), pp. 2865–2880.

Bennett, G.L. et al. 2013. Patterns and controls of sediment production, transfer and yield in the Illgraben. *Geomorphology* 188, pp. 68–82. Available at: http://dx.doi.org/10.1016/j.geomorph.2012.11.029.

Bennett, G.L. et al. 2014. A probabilistic sediment cascade model of sediment transfer in the Illgraben. *Water Resources Research* 50(2), pp. 1225–1244. Available at:

http://doi.wiley.com/10.1002/2013WR013806.

Blöthe, J.H. and Korup, O. 2013. Millennial lag times in the Himalayan sediment routing system. *Earth and Planetary Science Letters* 382, pp. 38–46. Available at: http://dx.doi.org/10.1016/j.epsl.2013.08.044.

Bonilla, M.G. et al. 1984. Statistical relations among earthquake magnitude, surface rupture length and surface fault displacement. *Bulletin of the Seismological Society of America* 74(6), pp. 2379–2411.

Bovis, M.J. and Jakob, M. 1999. The role of debris supply conditions in predicting debris flow activity. *Earth Surface Processes and Landforms* 24(11), pp. 1039–1054. doi: 10.1002/(SICI)1096-9837(199910)24:11<1039::AID-ESP29>3.0.CO;2-U.

Brain, M.J. et al. 2015. The effects of normal and shear stress wave phasing on coseismic landslide displacement. *Journal of Geophysical Research: Earth Surface* 120(6), pp. 1009–1022. doi: 10.1002/2014JF003417.

Brardinoni, F. et al. 2009. Colluvial sediment dynamics in mountain drainage basins. *Earth and Planetary Science Letters* 284(3–4), pp. 310–319. Available at: http://dx.doi.org/10.1016/j.epsl.2009.05.002.

Braucher, R. et al. 2011. Production of cosmogenic radionuclides at great depth: A multi element approach. *Earth and Planetary Science Letters* 309(1–2), pp. 1–9. doi: 10.1016/j.epsl.2011.06.036.

Burchfiel, B.C. et al. 1995. Tectonics of the Longmen Shan and Adjacent Regions, Central China. *International Geology Review* 37(8), pp. 661–735. Available at: https://www.tandfonline.com/doi/full/10.1080/00206819509465424.

Burchfiel, B.C. et al. 2008. A geological and geophysical context for the Wenchuan earthquake of 12 May 2008, Sichuan, People's Republic of China. *GSA Today* 18(7), pp. 4–11. doi: 10.1130/GSATG18A.1.

Cannon, S.H. et al. 2001. Wildfire-related debris-flow initiation processes, Storm King Mountain, Colorado. *Geomorphology* 39(3–4), pp. 171–188. doi: 10.1016/S0169-555X(00)00108-2.

Chang, D.S. et al. 2011. Field testing of erodibility of two landslide dams triggered by the 12 May Wenchuan earthquake. *Landslides* 8(October 2009), pp. 321–332. doi: 10.1007/s10346-011-0256-x.

Chen, H.X. et al. 2014. Evolution of debris flow properties and physical interactions in debris-flow mixtures in the Wenchuan earthquake zone. *Engineering Geology* 182(PB), pp. 136–147. Available at: http://dx.doi.org/10.1016/j.enggeo.2014.08.004.

Chen, S.F. et al. 1994. Active faulting and block movement associated with large earthquakes in the Min Shan and Longmen Mountains, northeastern Tibetan Plateau. *Journal of Geophysical Research: Solid Earth* 99(B12), pp. 24025–24038. Available at: http://doi.wiley.com/10.1029/94JB02132.

Chen, S.F. and Wilson, C.J.L. 1996. Emplacement of the Longmen Shan Thrust-Nappe Belt along the eastern margin of the Tibetan Plateau. *Journal of Structural Geology* 18(4), pp. 413–430. doi: 10.1016/0191-8141(95)00096-V.

Chen, X.L. et al. 2012. Evaluation of factors controlling large earthquake-induced landslides by the Wenchuan earthquake. *Natural Hazards and Earth System Science* 12(12), pp. 3645–3657. doi: 10.5194/nhess-12-3645-2012.

Clark, M.K. et al. 2005. Dynamic topography produced by lower crustal flow against rheological strength heterogeneities bordering the Tibetan Plateau. *Geophysical Journal International* 162(2), pp. 575–590. doi: 10.1111/j.1365-246X.2005.02580.x.

Collins, B.D. and Dunne, T. 2019. Thirty years of tephra erosion following the 1980 eruption of Mount St. Helens. *Earth Surface Processes and Landforms* 2793(August), pp. 2780–2793. doi: 10.1002/esp.4707.

Copley, A. 2008. Kinematics and dynamics of the southeastern margin of the Tibetan Plateau. *Geophysical Journal International* 174(3), pp. 1081–1100. doi: 10.1111/j.1365-246X.2008.03853.x.

Croissant, T. et al. 2017. Rapid post-seismic landslide evacuation boosted by dynamic river width. *Nature Geoscience* 10(9), pp. 680–684. doi: 10.1038/ngeo3005.

Croissant, T. et al. 2019. Seismic cycles, earthquakes, landslides and sediment fluxes: Linking tectonics to surface processes using a reduced-complexity model. *Geomorphology* 339, pp. 87–103. doi: 10.1016/j.geomorph.2019.04.017.

Cui, P. et al. 2013. Scale amplification of natural debris flows caused by cascading landslide dam failures. *Geomorphology* 182(August 2010), pp. 173–189. doi: 10.1016/j.geomorph.2012.11.009.

Cui, P. et al. 2014. The mechanisms behind shallow failures in slopes comprised of landslide deposits. *Engineering Geology* 180, pp. 34–44. Available at:

http://dx.doi.org/10.1016/j.enggeo.2014.04.009.

D'Odorico, P. and Fagherazzi, S. 2003. A probabilistic model of rainfall-triggered shallow landslides in hollows: A long-term analysis. *Water Resources Research* 39(9), pp. 1–14. doi: 10.1029/2002WR001595.

Dadson, S.J. et al. 2003. Links between erosion, runoff variability and seismicity in the Taiwan orogen. *Nature* 426(6967), pp. 648–651. doi: 10.1038/nature02150.

Dadson, S.J. et al. 2004. Earthquake-triggered increase in sediment delivery from an active mountain belt. *Geology* 32(8), p. 733. Available at: https://pubs.geoscienceworld.org/geology/article/32/8/733-736/29559.

Dahlquist, M.P. and West, A.J. 2019. Initiation and Runout of Post-Seismic Debris Flows: Insights From the 2015 Gorkha Earthquake. *Geophysical Research Letters* 46(16), pp. 9658–9668. Available at: https://onlinelibrary.wiley.com/doi/abs/10.1029/2019GL083548.

Dai, F.C. et al. 2011. Spatial distribution of landslides triggered by the 2008 Ms 8.0 Wenchuan earthquake, China. *Journal of Asian Earth Sciences* 40(4), pp. 883–895. doi: 10.1016/j.jseaes.2010.04.010.

Davy, P. and Lague, D. 2009. Fluvial erosion/transport equation of landscape evolution models revisited. *Journal of Geophysical Research: Solid Earth* 114(3), pp. 1–16. doi: 10.1029/2008JF001146.

Densmore, A.L. et al. 2007. Active tectonics of the Beichuan and Pengguan faults at the eastern margin of the Tibetan Plateau. *Tectonics* 26(4), pp. 1–17. doi: 10.1029/2006TC001987.

Densmore, A.L. et al. 2010. The role of late quaternary upper-crustal faults in the 12 may 2008 Wenchuan earthquake. *Bulletin of the Seismological Society of America* 100(5 B), pp. 2700–2712. doi: 10.1785/0120090294.

Densmore, A.L. et al. 2012. Reply to 'Isostasy can't be ignored'. *Nature Geoscience* 5(2), pp. 83–84. Available at: http://dx.doi.org/10.1038/ngeo1385.

Dietrich, W.E. et al. 1982. Construction of sediment budgets for drainage basins. *Workshop on sediment budgets and routing in forested drainage basins: proc.* , pp. 5–23.

Dietrich, W.E. and Montgomery, D.R. 1998. SHALSTAB: a digital terrain model for mapping shallow landslide potential. *National Council of the Paper Industry for Air and Stream Improvement Technical Report, February 1998* LVIII(1976), p. 29. Available at:

http://calm.geo.berkeley.edu/geomorph/shalstab/index.htm.

Dingle, E.H. et al. 2018. Temporal variability in detrital 10Be concentrations in a large Himalayan catchment. *Earth Surface Dynamics* 6(3), pp. 611–635. doi: 10.5194/esurf-6-611-2018.

Dunne, T. 1991. Stochastic aspects of the relations between climate, hydrology and landform evolution. *Transactions of Japanese Geomorphological Union (地形)* 12, pp. 1–24. Available at: http://ci.nii.ac.jp/naid/80005684834/en/.

Dunning, S.A. et al. 2006. Formation and failure of the Tsatichhu landslide dam, Bhutan. *Landslides* 3(2), pp. 107–113. doi: 10.1007/s10346-005-0032-x.

Dunning, S.A. 2006. The grain-size distribution of rock avalanche deposits in valley-confined settings. *Italian Journal of Engineering Geology andEnvironment* 1(1), pp. 117–121. doi: 10.4408/IJEGE.2006-01.S-15.

Egholm, D.L. et al. 2013. Lifespan of mountain ranges scaled by feedbacks between landsliding and erosion by rivers. *Nature* 498(7455), pp. 475–478. doi: 10.1038/nature12218.

England, P. and Molnar, P. 1990. Surface uplift, uplift of rocks, and exhumation of rocks. *Geology* 18(12), pp. 1173–1177. doi: 10.1130/0091-7613(1990)018<1173:SUUORA>2.3.CO.

Fan, X. et al. 2012a. Simulating dam-breach flood scenarios of the Tangjiashan landslide dam induced by the Wenchuan Earthquake. *Natural Hazards and Earth System Science* 12(10), pp. 3031–3044. doi: 10.5194/nhess-12-3031-2012.

Fan, X. et al. 2012b. Transient water and sediment storage of the decaying landslide dams induced by the 2008 Wenchuan earthquake, China. *Geomorphology* 171–172, pp. 58–68. Available at: http://dx.doi.org/10.1016/j.geomorph.2012.05.003.

Fan, X. et al. 2018a. Spatio-temporal evolution of mass wasting after the 2008 Mw 7 . 9 Wenchuan Earthquake revealed by a detailed multi-temporal inventory. *Landslides* 15(September), pp. 2325–2341. doi: 10.1007/s10346-018-1054-5.

Fan, X. et al. 2018b. What we have learned from the 2008 Wenchuan Earthquake and its aftermath: A decade of research and challenges. *Engineering Geology* 241(May), pp. 25–32. Available at: https://doi.org/10.1016/j.enggeo.2018.05.004.

Fan, X. et al. 2019a. Comment on ‘Gigantic rockslides induced by fluvial incision in the

Diexi area along the eastern margin of the Tibetan Plateau' by Zhao et al. (2019) Geomorphology 338, 27–42. *Geomorphology* (xxxx), p. 106963. Available at: https://doi.org/10.1016/j.geomorph.2019.106963.

Fan, X. et al. 2019b. Earthquake-Induced Chains of Geologic Hazards: Patterns, Mechanisms, and Impacts. *Reviews of Geophysics* . doi: 10.1029/2018RG000626.

Fan, X. et al. 2019c. Two multi-temporal datasets that track the enhanced landsliding after the 2008 Wenchuan earthquake. *Earth System Science Data* 11(1), pp. 35–55. Available at: https://www.earth-syst-sci-data.net/11/35/2019/.

Feng, G. et al. 2010. Coseismic fault slip of the 2008 Mw 7.9 Wenchuan earthquake estimated from InSAR and GPS measurements. *Geophysical Research Letters* 37(1), pp. 1–5. doi: 10.1029/2009GL041213.

Frank, F. et al. 2018. Landslides and increased debris-flow activity: A systematic comparison of six catchments in Switzerland. *Earth Surface Processes and Landforms* 712(November 1987), pp. 699–712. doi: 10.1002/esp.4524.

Froude, M.J. and Petley, D.N. 2018. Global fatal landslide occurrence from 2004 to 2016. *Natural Hazards and Earth System Sciences* 18(8), pp. 2161–2181. doi: 10.5194/nhess-18-2161-2018.

Fusun, S. et al. 2013. Effects of different types of vegetation recovery on runoff and soil erosion on a Wenchuan earthquake-triggered landslide, China. *Journal of Soil and Water Conservation* 68(2), pp. 138–145. doi: 10.2489/jswc.68.2.138.

Gabet, E.J. and Mudd, S.M. 2006. The mobilization of debris flows from shallow landslides. *Geomorphology* 74(1–4), pp. 207–218. doi: 10.1016/j.geomorph.2005.08.013.

Gallen, S.F. et al. 2015. Coseismic landslides reveal near-surface rock strength in a highrelief, tectonically active setting. *Geology* 43(1), pp. 11–14. doi: 10.1130/G36080.1.

Galli, M. et al. 2008. Comparing landslide inventory maps. *Geomorphology* 94(3–4), pp. 268–289. doi: 10.1016/j.geomorph.2006.09.023.

Giardini, D. et al. 1999. The GSHAP Global Seismic Hazard Map. *Annali Di Geofisica* 42(6), pp. 1225–1230.

Godard, V. et al. 2009. Late Cenozoic evolution of the central Longmen Shan, eastern Tibet: Insight from (U-Th)/He thermochronometry. *Tectonics* 28(5). doi: 10.1029/2008TC002407.

Godard, V. et al. 2010. Spatial distribution of denudation in Eastern Tibet and regressive erosion of plateau margins. *Tectonophysics* 491(1–4), pp. 253–274. Available at: http://dx.doi.org/10.1016/j.tecto.2009.10.026.

Gorum, T. et al. 2011. Distribution pattern of earthquake-induced landslides triggered by the 12 May 2008 Wenchuan earthquake. *Geomorphology* 133(3–4), pp. 152–167. Available at: http://dx.doi.org/10.1016/j.geomorph.2010.12.030.

Gosse, J. and Philips, F. 2001. Terrestrial in situ cosmogenic nuclides:theory and application. *Quaternary Science Reviews* 20, pp. 1475–1560.

Gran, K.B. and Czuba, J.A. 2017. Sediment pulse evolution and the role of network structure. *Geomorphology* 277, pp. 17–30. Available at: http://dx.doi.org/10.1016/j.geomorph.2015.12.015.

Granger, D.E. and Muzikar, P.F. 2001. Dating sediment burial with in situ-produced cosmogenic nuclides: Theory, techniques, and limitations. *Earth and Planetary Science Letters* 188(1–2), pp. 269–281. doi: 10.1016/S0012-821X(01)00309-0.

Grieve, S.W.D. et al. 2016. How does grid-resolution modulate the topographic expression of geomorphic processes? *Earth Surface Dynamics* 4(3), pp. 627–653. doi: 10.5194/esurf-4-627-2016.

Guo, C. and Cui, Y. 2020. Pore structure characteristics of debris flow source material in the Wenchuan earthquake area. *Engineering Geology* 267(August 2018), p. 105499. Available at: https://doi.org/10.1016/j.enggeo.2020.105499.

Guo, X. et al. 2016a. Intensity-duration threshold of rainfall-triggered debris flows in the Wenchuan Earthquake affected area, China. *Geomorphology* 253, pp. 208–216. doi: 10.1016/j.geomorph.2015.10.009.

Guo, X. et al. 2016b. The formation and development of debris flows in large watersheds after the 2008 Wenchuan Earthquake. *Landslides* 13(1), pp. 25–37. doi: 10.1007/s10346-014-0541-6.

Guzzetti, F. et al. 2008. The rainfall intensity-duration control of shallow landslides and debris flows: An update. *Landslides* 5(1), pp. 3–17. doi: 10.1007/s10346-007-0112-1.

Guzzetti, F. et al. 2012. Landslide inventory maps: New tools for an old problem. *Earth-Science Reviews* 112(1–2), pp. 42–66. Available at: http://dx.doi.org/10.1016/j.earscirev.2012.02.001.

de Haas, T. et al. 2020. How memory effects, check dams, and channel geometry control erosion and deposition by debris flows. *Scientific Reports* 10(1), pp. 1–8. Available at: https://doi.org/10.1038/s41598-020-71016-8.

Haefeli, R. 1948. The stability of slopes acted upon by parallel seepage. *Proc. 2nd Int. Conf on Soil Mechanics* 1, pp. 57–62.

Hales, T.C. et al. 2005. A lithospheric instability origin for Columbia River flood basalts and Wallowa Mountains uplift in northeast Oregon. *Nature* 438(7069), pp. 842–845. doi: 10.1038/nature04313.

Hales, T.C. 2018. Modelling biome-scale root reinforcement and slope stability. *Earth Surface Processes and Landforms* 43(10), pp. 2157–2166. doi: 10.1002/esp.4381.

Harel, M. et al. 2016. Geomorphology Global analysis of the stream power law parameters based on worldwide Be denudation rates. *Geomorphology* 268, pp. 184–196. Available at: http://dx.doi.org/10.1016/j.geomorph.2016.05.035.

Harrison, L.M. et al. 2015. Post-rock-avalanche dam outburst flood sedimentation in Ram Creek, Southern Alps, New Zealand. *Geomorphology* . doi: 10.1016/j.geomorph.2015.03.038.

Heimsath, A.M. et al. 1997. The soil production function and landscape equilibrium. *Nature* 388(6640), pp. 358–361. doi: 10.1038/41056.

Hilton, R.G. and West, A.J. 2020. Mountains, erosion and the carbon cycle. *Nature Reviews Earth & Environment* 1(6), pp. 284–299. Available at: http://dx.doi.org/10.1038/s43017-020-0058-6.

Horton, A.J. et al. 2019. Identifying post-earthquake debris flow hazard using Massflow. *Engineering Geology* 258. doi: 10.1016/j.enggeo.2019.05.011.

Hovius, N. et al. 1997. Sediment flux from a mountain belt derived by landslide mapping. *Geology* 25(3), pp. 231–234. doi: 10.1130/0091-7613(1997)025<0231:SFFAMB>2.3.CO;2.

Hovius, N. et al. 2011. Prolonged seismically induced erosion and the mass balance of a large earthquake. *Earth and Planetary Science Letters* 304(3–4), pp. 347–355. Available at: http://dx.doi.org/10.1016/j.epsl.2011.02.005.

Howarth, J.D. et al. 2012. Lake sediments record cycles of sediment flux driven by large earthquakes on the Alpine fault, New Zealand. *Geology* 40(12), pp. 1091–1094. doi:

10.1130/G33486.1.

Hu, W. et al. 2016. Initiation processes for run-off generated debris flows in the Wenchuan earthquake area of China. *Geomorphology* 253, pp. 468–477. doi: 10.1016/j.geomorph.2015.10.024.

Hu, W. et al. 2017. Sensitivity of the initiation and runout of flowslides in loose granular deposits to the content of small particles: An insight from flume tests. *Engineering Geology* 231(July), pp. 34–44. Available at: https://doi.org/10.1016/j.enggeo.2017.10.001.

Hu, W. et al. 2018. Internal Erosion Controls Failure and Runout of Loose Granular Deposits: Evidence From Flume Tests and Implications for Postseismic Slope Healing. *Geophysical Research Letters* 45(11), pp. 5518–5527. doi: 10.1029/2018GL078030.

Huang, R. 2011. Geo-engineering lessons learned from the 2008 Wenchuan earthquake in Sichuan and their significance to reconstruction. *Journal of Mountain Science* 8(2), pp. 176–189. doi: 10.1007/s11629-011-2103-x.

Huang, R. and Fan, X. 2013. The landslide story. *Nature Geoscience* 6(5), pp. 325–326. Available at: http://dx.doi.org/10.1038/ngeo1806.

Hubbard, J. and Shaw, J.H. 2009. Uplift of the Longmen Shan and Tibetan plateau, and the 2008 Wenchuan (M = 7.9) earthquake. *Nature* 458(7235), pp. 194–197. Available at: http://dx.doi.org/10.1038/nature07837.

Huffman, G.J. et al. 2019. GPM IMERG Final Precipitation L3 1 month 0.1 degree x 0.1 degree V06. Available at: https://disc.gsfc.nasa.gov/datasets/GPM_3IMERGM_06/summary [Accessed: 15 January 2020].

Hungr, O. et al. 2014. The Varnes classification of landslide types, an update. *Landslides* 11(2), pp. 167–194. doi: 10.1007/s10346-013-0436-y.

Iverson, R.M. et al. 1997. Debris-Flow Mobilization From Landslides. *Annual Review of Earth and Planetary Sciences* 25, pp. 85–138.

Iverson, R.M. 1997. The Physics of Debris Flows. *Reviews of Geophysics* 35(3), pp. 245–296.

Iverson, R.M. et al. 2000. Acute sensitivity of landslide rates to initial soil porosity. *Science* 290(5491), pp. 513–516. doi: 10.1126/science.290.5491.513.

Iverson, R.M. 2000. Landslide triggering by rain infiltration. *Water Resources Research*

36(7), pp. 1897–1910. doi: 10.1029/2000WR900090.

Iverson, R.M. et al. 2011. Positive feedback and momentum growth during debris-flow entrainment of wet bed sediment. *Nature Geoscience* 4(2), pp. 116–121. doi: 10.1038/ngeo1040.

Iverson, R.M. and George, D.L. 2016. Modelling landslide liquefaction, mobility bifurcation and the dynamics of the 2014 Oso disaster. *Geotechnique* 66(3), pp. 175–187. doi: 10.1680/jgeot.15.LM.004.

Jakob, M. et al. 2005. The significance of channel recharge rates for estimating debris-flow magnitude and frequency. *Earth Surface Processes and Landforms* 30(6), pp. 755–766. doi: 10.1002/esp.1188.

Jerolmack, D.J. and Paola, C. 2010. Shredding of environmental signals by sediment transport. *Geophysical Research Letters* 37(19), p. n/a-n/a. Available at: http://doi.wiley.com/10.1029/2010GL044638.

Kaitna, R. et al. 2016. Effects of coarse grain size distribution and fine particle content on pore fluid pressure and shear behavior in experimental debris flow. *Journal of Geophysical Research: Earth Surface* 121, pp. 2298–2317. doi: 10.1002/2015JF003725.

Kargel, J.S. et al. 2016. Geomorphic and geologic controls of geohazards induced by Nepal's 2015 Gorkha earthquake. *Science* 351(6269). doi: 10.1126/science.aac8353.

Keefer, D.K. 1994. The importance of earthquake-induced landslides to long-term slope erosion and slope-failure hazards in seismically active regions. *Geomorphology* 10(1–4), pp. 265–284. doi: 10.1016/0169-555X(94)90021-3.

Keefer, D.K. 2002. Investigating landslides caused by earthquakes - A historical review. *Surveys in Geophysics* 23(6), pp. 473–510. doi: 10.1023/A:1021274710840.

Kirby, E. et al. 2003. Distribution of active rock uplift along the eastern margin of the Tibetan Plateau: Inferences from bedrock channel longitudinal profiles. *Journal of Geophysical Research: Solid Earth* 108(B4), p. B4,2217. Available at: http://doi.wiley.com/10.1029/2001JB000861.

Kirby, E. and Ouimet, W. 2011. Tectonic geomorphology along the eastern margin of Tibet: insights into the pattern and processes of active deformation adjacent to the Sichuan Basin. *Geological Society, London, Special Publications* 353(1), pp. 165–188. Available at: http://sp.lyellcollection.org/lookup/doi/10.1144/SP353.9.

Kirchner, J.W. et al. 2001. Mountain erosion over 10 yr , 10 k.y ., and 10 m.y. time scales. *Geology* 29(7), pp. 591–594. Available at: http://geology.geoscienceworld.org/content/29/7/591.short%0Ahttp://www.fs.fed.us/rm/pubs_other/rmrs_2001_clayton_j001.pdf%0Ahttp://geology.gsapubs.org/cgi/doi/10.1130/0091-7613(2001)029%3C0591:MEOYKY%3E2.0.CO;2%0Ahttp://geology.gsapubs.org/content/29/7/59.

Korup, O. et al. 2004. Sediment generation and delivery from large historic landslides in the Southern Alps, New Zealand. *Geomorphology* 61(1–2), pp. 189–207. doi: 10.1016/j.geomorph.2004.01.001.

Korup, O. 2005. Large landslides and their effect on sediment flux in South Westland, New Zealand. *Earth Surface Processes and Landforms* 30(3), pp. 305–323. doi: 10.1002/esp.1143.

Korup, O. et al. 2010. The role of landslides in mountain range evolution. *Geomorphology* 120(1–2), pp. 77–90. Available at: http://dx.doi.org/10.1016/j.geomorph.2009.09.017.

Korup, O. and Clague, J.J. 2009. Natural hazards, extreme events, and mountain topography. *Quaternary Science Reviews* 28(11–12), pp. 977–990. Available at: http://dx.doi.org/10.1016/j.quascirev.2009.02.021.

Koyanagi, K. et al. 2020. Characteristics of landslides in forests and grasslands triggered by the 2016 Kumamoto earthquake. *Earth Surface Processes and Landforms* 45(4), pp. 893–904. doi: 10.1002/esp.4781.

Lamb, M.P. et al. 2008. Is the critical shields stress for incipient sediment motion dependent on channel-bed slope? *Journal of Geophysical Research: Earth Surface* 113(2), pp. 1–20. doi: 10.1029/2007JF000831.

Larsen, I.J. et al. 2006. Geologic versus wildfire controls on hillslope processes and debris flow initiation in the Green River canyons of Dinosaur National Monument. *Geomorphology* 81(1–2), pp. 114–127. doi: 10.1016/j.geomorph.2006.04.002.

Larsen, I.J. et al. 2010. Landslide erosion controlled by hillslope material. *Nature Geoscience* 3(4), pp. 247–251. Available at: http://dx.doi.org/10.1038/ngeo776.

Larsen, I.J. et al. 2014. The contribution of mountains to global denudation. *Geology* 42(6), pp. 527–530. doi: 10.1130/G35136.1.

Legros, F. 2002. The mobility of long runout landslides. *Engineering Geology* 63, pp. 301–

331. doi: http://dx.doi.org/10.1016/S0013-7952(01)00090-4.

Li, G. et al. 2014. Seismic mountain building: Landslides associated with the 2008 Wenchuan earthquake in the context of a generalized model for earthquake volume balance. *Geochemistry, Geophysics, Geosystems* 15(4), pp. 833–844. Available at: http://doi.wiley.com/10.1002/2013GC005067.

Li, G. et al. 2016a. Connectivity of earthquake-triggered landslides with the fluvial network: Implications for landslide sediment transport after the 2008 Wenchuan earthquake. *Journal of Geophysical Research: Earth Surface* 121(4), pp. 703–724. Available at: http://doi.wiley.com/10.1002/2015JF003718.

Li, G. et al. 2017a. Earthquakes drive focused denudation along a tectonically active mountain front. *Earth and Planetary Science Letters* 472, pp. 253–265. Available at: http://dx.doi.org/10.1016/j.epsl.2017.04.040.

Li, G. et al. 2019. Competing Effects of Mountain Uplift and Landslide Erosion Over Earthquake Cycles. *Journal of Geophysical Research: Solid Earth* 124(5), pp. 5101–5133. Available at: https://onlinelibrary.wiley.com/doi/abs/10.1029/2018JB016986.

Li, Y. et al. 2003. Evolution of the Longmen Shan Foreland Basin (Western Sichuan, China) during the Late Triassic Indosinian orogeny. *Basin Research* 15(1), pp. 117–138. doi: 10.1046/j.1365-2117.2003.00197.x.

Li, Z. et al. 2016b. Quaternary activity of the range front thrust system in the Longmen Shan piedmont, China, revealed by seismic imaging and growth strata. *Tectonics* 35(12), pp. 2807–2827. doi: 10.1002/2015TC004093.

Li, Z. et al. 2017b. Re-evaluating seismic hazard along the southern Longmen Shan, China: Insights from the 1970 Dayi and 2013 Lushan earthquakes. *Tectonophysics* 717(135), pp. 519–530. Available at: http://dx.doi.org/10.1016/j.tecto.2017.09.001.

Lin, C.W. et al. 2004. Impact of Chi-Chi earthquake on the occurrence of landslides and debris flows: Example from the Chenyulan River watershed, Nantou, Taiwan. *Engineering Geology* 71(1–2), pp. 49–61. doi: 10.1016/S0013-7952(03)00125-X.

Liu-Zeng, J. et al. 2009. Co-seismic ruptures of the 12 May 2008, Ms8.0 Wenchuan earthquake, Sichuan: East-west crustal shortening on oblique, parallel thrusts along the eastern edge of Tibet. *Earth and Planetary Science Letters* 286(3–4), pp. 355–370. Available at: http://dx.doi.org/10.1016/j.epsl.2009.07.017.

Ma, C. et al. 2017. Rainfall intensity–duration threshold and erosion competence of debris

flows in four areas affected by the 2008 Wenchuan earthquake. *Geomorphology* 282, pp. 85–95. Available at: http://dx.doi.org/10.1016/j.geomorph.2017.01.012.

Major, J.J. et al. 2019. Multidecadal Geomorphic Evolution of a Profoundly Disturbed Gravel Bed River System—A Complex, Nonlinear Response and Its Impact on Sediment Delivery. *Journal of Geophysical Research: Earth Surface* 124(5), pp. 1281–1309. doi: 10.1029/2018JF004843.

Malamud, B.D. et al. 2004a. Landslide inventories and their statistical properties. *Earth Surface Processes and Landforms* 29(6), pp. 687–711. doi: 10.1002/esp.1064.

Malamud, B.D. et al. 2004b. Landslides, earthquakes, and erosion. *Earth and Planetary Science Letters* 229(1–2), pp. 45–59. doi: 10.1016/j.epsl.2004.10.018.

Marc, O. et al. 2015. Transient changes of landslide rates after earthquakes. *Geology* 43(10), pp. 883–886. doi: 10.1130/G36961.1.

Marc, O. et al. 2016a. A seismologically consistent expression for the total area and volume of earthquake-triggered landsliding. *Journal of Geophysical Research: Earth Surface* 121(4), pp. 640–663. Available at: http://doi.wiley.com/10.1002/2015JF003732.

Marc, O. et al. 2016b. The mass balance of earthquakes and earthquake sequences. *Geophysical Research Letters* 43(8), pp. 3708–3716. doi: 10.1002/2016GL068333.

Marc, O. et al. 2017. Prediction of the area affected by earthquake-induced landsliding based on seismological parameters. *Natural Hazards and Earth System Sciences* 17(7), pp. 1159–1175. Available at: https://www.nat-hazards-earth-syst-sci.net/17/1159/2017/.

Marc, O. et al. 2019. Long-term erosion of the Nepal Himalayas by bedrock landsliding: the role of monsoons, earthquakes and giant landslides. *Earth Surface Dynamics* 7, pp. 107–128. doi: 10.5194/esurf-2018-69.

Marc, O. and Hovius, N. 2015. Amalgamation in landslide maps: Effects and automatic detection. *Natural Hazards and Earth System Sciences* 15(4), pp. 723–733. doi: 10.5194/nhess-15-723-2015.

McGuire, L.A. et al. 2013. Controls on the spacing and geometry of rill networks on hillslopes: Rain splash detachment, initial hillslope roughness, and the competition between fluvial and colluvial transport. *Journal of Geophysical Research: Earth Surface* 118(1), pp. 241–256. doi: 10.1002/jgrf.20028.

McGuire, L.A. et al. 2016. Constraining the relative importance of raindrop- and flow-

driven sediment transport mechanisms in postwildfire environments and implications for recovery time scales. *Journal of Geophysical Research: Earth Surface* 121(11), pp. 2211–2237. doi: 10.1002/2016JF003867.

McGuire, L.A. et al. 2017a. Debris flow initiation by runoff in a recently burned basin: Is grain-by-grain sediment bulking or en masse failure to blame? *Geophysical Research Letters* 44(14), pp. 7310–7319. doi: 10.1002/2017GL074243.

McGuire, L.A. et al. 2017b. Debris flow initiation by runoff in a recently burned basin: Is grain-by-grain sediment bulking or en masse failure to blame? *Geophysical Research Letters* 44(14), pp. 7310–7319. doi: 10.1002/2017GL074243.

Meade, B.J. 2010. The signature of an unbalanced earthquake cycle in Himalayan topography? *Geology* 38(11), pp. 987–990. doi: 10.1130/G31439.1.

Meunier, P. et al. 2008. Topographic site effects and the location of earthquake induced landslides. *Earth and Planetary Science Letters* 275(3–4), pp. 221–232. Available at: http://dx.doi.org/10.1016/j.epsl.2008.07.020.

Meunier, P. et al. 2013. Landslide patterns reveal the sources of large earthquakes. *Earth and Planetary Science Letters* 363, pp. 27–33. Available at: http://dx.doi.org/10.1016/j.epsl.2012.12.018.

Michel, G.P. et al. 2014. Comparative analysis of SHALSTAB and SINMAP for landslide susceptibility mapping in the Cunha River basin, southern Brazil. *Journal of Soils and Sediments* 14(7), pp. 1266–1277. doi: 10.1007/s11368-014-0886-4.

Milledge, D.G. et al. 2012. Limits on the validity of infinite length assumptions for modelling shallow landslides. *Earth Surface Processes and Landforms* 37(11), pp. 1158–1166. doi: 10.1002/esp.3235.

Milledge, D.G. et al. 2014. A multidimensional stability model for predicting shallow landslide size and shape across landscapes. *Journal of Geophysical Research: Earth Surface* 119, pp. 2481–2504. doi: 10.1002/2014JF003135.Received.

Molnar, P. et al. 1993. Mantle dynamics, uplift of the Tibetan plateau, and the Indean monsoon. *Reviews of Geophysics* 31(4), pp. 357–396. Available at: http://www.agu.org/pubs/crossref/1993/93RG02030.shtml.

Molnar, P. 2012. Isostasy can’t be ignored. *Nature Geoscience* 5(2), p. 83. Available at: http://dx.doi.org/10.1038/ngeo1383.

Molnar, P. et al. 2015. Mantle dynamics, isostasy, and the support of high terrain. *Journal of Geophysical Research: Solid Earth* 120(3), pp. 1932–1957. Available at: http://doi.wiley.com/10.1002/2014JB011724.

Montgomery, D.R. and Brandon, M.T. 2002. Topographic controls on erosion rates in tectonically active mountain ranges. *Earth and Planetary Science Letters* 201(3–4), pp. 481–489. doi: 10.1016/S0012-821X(02)00725-2.

Montgomery, D.R. and Dietrich, W.E. 1994. A physically based model for the topographic control on shallow landsliding. *Water Resources Research* 30(4), pp. 1153–1171. doi: 10.1029/93WR02979.

Mudd, S.M. et al. 2020. LSDtopotools/LSDTopoTools2: LSDTopoTools2 v0.3. Available at: https://doi.org/10.5281/zenodo.3769703#.X6AA9d3MMXY.mendeley [Accessed: 2 November 2020].

Murphy, B.P. et al. 2019. Post-wildfire sediment cascades: A modeling framework linking debris flow generation and network-scale sediment routing. *Earth Surface Processes and Landforms* 2140(June), pp. 2126–2140. doi: 10.1002/esp.4635.

Niemi, N.A. et al. 2005. Effects of bedrock landslides on cosmogenically determined erosion rates. *Earth and Planetary Science Letters* 237(3–4), pp. 480–498. doi: 10.1016/j.epsl.2005.07.009.

Nowicki Jessee, M.A. et al. 2018. A Global Empirical Model for Near-Real-Time Assessment of Seismically Induced Landslides. *Journal of Geophysical Research: Earth Surface* 123(8), pp. 1835–1859. doi: 10.1029/2017JF004494.

Ouimet, W.B. et al. 2007. The influence of large landslides on river incision in a transient landscape: Eastern margin of the Tibetan Plateau (Sichuan, China). *Bulletin of the Geological Society of America* 119(11–12), pp. 1462–1476. doi: 10.1130/B26136.1.

Ouimet, W.B. et al. 2009. Beyond threshold hillslopes: Channel adjustment to base-level fall in tectonically active mountain ranges. *Geology* 37(7), pp. 579–582. doi: 10.1130/G30013A.1.

Ouimet, W.B. 2010. Landslides associated with the May 12, 2008 Wenchuan earthquake: Implications for the erosion and tectonic evolution of the Longmen Shan. *Tectonophysics* 491(1–4), pp. 244–252. Available at: http://dx.doi.org/10.1016/j.tecto.2009.09.012.

Ouyang, C. et al. 2015. Numerical analysis of dynamics of debris flow over erodible beds in Wenchuan earthquake-induced area. *Engineering Geology* 194, pp. 62–72. Available at:

http://dx.doi.org/10.1016/j.enggeo.2014.07.012.

Parker, R.N. et al. 2011. Mass wasting triggered by the 2008 Wenchuan earthquake is greater than orogenic growth. *Nature Geoscience* 4(7), pp. 449–452. Available at: http://dx.doi.org/10.1038/ngeo1154.

Parker, R.N. et al. 2015. Spatial distributions of earthquake-induced landslides and hillslope preconditioning in the northwest South Island, New Zealand. *Earth Surface Dynamics* 3(4), pp. 501–525. Available at: https://www.earth-surf-dynam.net/3/501/2015/.

Pearce, A.J. and Watson, A.J. 1986. Effects of earthquake-induced landslides on sediment budget and transport over a 50-yr period. *Geology* 14, pp. 52–55.

Prancevic, J.P. et al. 2014. Incipient sediment motion across the river to debris-flow transition. *Geology* 42(3), pp. 191–194. doi: 10.1130/G34927.1.

Prancevic, J.P. et al. 2018. The Role of Three-Dimensional Boundary Stresses in Limiting the Occurrence and Size of Experimental Landslides. *Journal of Geophysical Research: Earth Surface* 123(1), pp. 46–65. doi: 10.1002/2017JF004410.

Pratt, B. et al. 2002. Impulsive alluviation during early Holocene strenghened monsoons, central Nepal Himalaya. *Geology* 30(10), pp. 911–914. doi: 10.1130/0091-7613(2002)030<0911:IADEHS>2.0.CO;2.

Reichenbach, P. et al. 2018. A review of statistically-based landslide susceptibility models. *Earth-Science Reviews* 180(March), pp. 60–91. Available at: https://doi.org/10.1016/j.earscirev.2018.03.001.

Roback, K. et al. 2018. The size, distribution, and mobility of landslides caused by the 2015 Mw7.8 Gorkha earthquake, Nepal. *Geomorphology* 301, pp. 121–138. Available at: https://doi.org/10.1016/j.geomorph.2017.01.030.

Robert, A. et al. 2010. Structural and thermal characters of the Longmen Shan (Sichuan, China). *Tectonophysics* 491(1–4), pp. 165–173. doi: 10.1016/j.tecto.2010.03.018.

Robinson, T.R. et al. 2016. Coseismic landsliding estimates for an Alpine Fault earthquake and the consequences for erosion of the Southern Alps, New Zealand. *Geomorphology* 263, pp. 71–86. Available at: http://dx.doi.org/10.1016/j.geomorph.2016.03.033.

Roda-Boluda, D.C. et al. 2018. Lithological controls on hillslope sediment supply: insights from landslide activity and grain size distributions. *Earth Surface Processes and Landforms* 43(5). doi: 10.1002/esp.4281.

Royden, L.H. et al. 1997. Surface deformation and lower crust flow in eastern Tibet. *Science* 276(788–790), pp. 788–791.

Royden, L.H. et al. 2008. The Geological Evolution of the Tibetan Plateau. *Science* 321(5892), pp. 1054–1058. Available at: https://www.sciencemag.org/lookup/doi/10.1126/science.1155371.

Schumer, R. and Jerolmack, D.J. 2009. Real and apparent changes in sediment deposition rates through time. *Journal of Geophysical Research: Solid Earth* 114(3), pp. 1–12. doi: 10.1029/2009JF001266.

Schürch, P. et al. 2011. Dynamic controls on erosion and deposition on debris-flow fans. *Geology* 39(9), pp. 827–830. doi: 10.1130/G32103.1.

Selby, M.J. 1983. *Hillslope materials and processes.* Oxford University Press.

Shen, P. et al. 2020. Declining geohazard activity with vegetation recovery during first ten years after the 2008 Wenchuan earthquake. *Geomorphology* 352, p. 106989. Available at: https://doi.org/10.1016/j.geomorph.2019.106989.

Shen, X. et al. 2019. Late Miocene Hinterland Crustal Shortening in the Longmen Shan Thrust Belt, the Eastern Margin of the Tibetan Plateau. *Journal of Geophysical Research: Solid Earth* , pp. 972–991. doi: 10.1029/2019JB018358.

Shieh, C.L. et al. 2009. Variability in rainfall threshold for debris flow after the Chi-Chi earthquake in central Taiwan, China. *International Journal of Sediment Research* 24(2), pp. 177–188. Available at: http://dx.doi.org/10.1016/S1001-6279(09)60025-1.

Simpson, G. 2015. Accumulation of permanent deformation during earthquake cycles on reverse faults. *Journal of Geophysical Research: Solid Earth* 120(3), pp. 1958–1974. doi: 10.1002/2014JB011442.

Stark, C.P. et al. 2001. The characterization of landslide size distributions. *Geophysical Research Letters* 28(6), pp. 1091–1094.

Stark, C.P. and Guzzetti, F. 2009. Landslide rupture and the probability distribution of mobilized debris volumes. *Journal of Geophysical Research: Earth Surface* 114(2), pp. 1–16. doi: 10.1029/2008JF001008.

Stolle, A. et al. 2017. Catastrophic valley fills record large Himalayan earthquakes, Pokhara, Nepal. *Quaternary Science Reviews* 177, pp. 88–103. Available at: https://doi.org/10.1016/j.quascirev.2017.10.015.

Straumann, R.K. and Korup, O. 2009. Quantifying postglacial sediment storage at the mountain-belt scale. *Geology* 37(12), pp. 1079–1082. doi: 10.1130/G30113A.1.

Tadono, T. et al. 2016. Generation of the 30 M-MESH global digital surface model by alos prism. *International Archives of the Photogrammetry, Remote Sensing and Spatial Information Sciences - ISPRS Archives* 41(July), pp. 157–162. doi: 10.5194/isprsarchives-XLI-B4-157-2016.

Takahashi, T. 1981. Debris flow. *Annual review of fluid mechanics* 13, pp. 57–77. doi: 10.1146/annurev.fl.13.010181.000421.

Tang, C. et al. 2009. Rainfall-triggered debris flows following the Wenchuan earthquake. *Bulletin of Engineering Geology and the Environment* 68(2), pp. 187–194. doi: 10.1007/s10064-009-0201-6.

Tang, C. et al. 2011. Catastrophic debris flows triggered by a 14 August 2010 rainfall at the epicenter of the Wenchuan earthquake. *Landslides* 8(4), pp. 485–497. doi: 10.1007/s10346-011-0269-5.

Tang, C. et al. 2012. Catastrophic debris flows on 13 August 2010 in the Qingping area, southwestern China: The combined effects of a strong earthquake and subsequent rainstorms. *Geomorphology* 139–140(August 2010), pp. 559–576. Available at: http://dx.doi.org/10.1016/j.geomorph.2011.12.021.

Tang, C. et al. 2016. Analysing post-earthquake landslide activity using multi-temporal landslide inventories near the epicentral area of the 2008 Wenchuan earthquake. *Natural Hazards and Earth System Sciences* 16(12), pp. 2641–2655. doi: 10.5194/nhess-16-2641-2016.

Tang, H. et al. 2019. Evolution of debris-flow initiation mechanisms and sediment sources during a sequence of post-wildfire rainstorms. *Journal of Geophysical Research: Earth Surface* , pp. 1–24. doi: 10.1029/2018jf004837.

Tapponnier, P. 2001. Oblique Stepwise Rise and Growth of the Tibet Plateau. *Science* 294(5547), pp. 1671–1677. Available at: http://www.sciencemag.org/cgi/doi/10.1126/science.105978.

Taylor, D.W. 1948. *Fundamentals of Soil Mechanics*. New York: Wiley.

Tian, Y. et al. 2013. Constructing the Longmen Shan eastern Tibetan Plateau margin: Insights from low-temperature thermochronology. *Tectonics* 32(3), pp. 576–592. doi: 10.1002/tect.20043.

Tian, Y. et al. 2018. Eocene to Miocene Out-of-Sequence Deformation in the Eastern Tibetan Plateau: Insights From Shortening Structures in the Sichuan Basin. *Journal of Geophysical Research: Solid Earth* 123(2), pp. 1840–1855. doi: 10.1002/2017JB015049.

Tolorza, V. et al. 2019. Suspended Sediments in Chilean Rivers Reveal Low Postseismic Erosion After the Maule Earthquake (Mw 8.8) During a Severe Drought. *Journal of Geophysical Research: Earth Surface* 124(6), pp. 1378–1397. Available at: https://onlinelibrary.wiley.com/doi/abs/10.1029/2018JF004766.

Turcotte, D.L. and Schubert, G. 2002. *Geodynamics*. Second edi. Cambridge University Press.

Valagussa, A. et al. 2019. Seismic and geological controls on earthquake-induced landslide size. *Earth and Planetary Science Letters* 506, pp. 268–281. Available at: https://linkinghub.elsevier.com/retrieve/pii/S0012821X18306563.

Wang, E. et al. 2012. Two-phase growth of high topography in eastern Tibet during the Cenozoic. *Nature Geoscience* 5(9), pp. 640–645. doi: 10.1038/ngeo1538.

Wang, G. et al. 2003. Downslope volume enlargement of a debris slide-debris flow in the 1999 Hiroshima, Japan, rainstorm. *Engineering Geology* 69(3–4), pp. 309–330. doi: 10.1016/S0013-7952(02)00289-2.

Wang, J. et al. 2015. Controls on fluvial evacuation of sediment from earthquake-triggered landslides. *Geology* 43(2), pp. 115–118. doi: 10.1130/G36157.1.

Wang, J.J. et al. 2013. Angle of repose of landslide debris deposits induced by 2008 Sichuan Earthquake. *Engineering Geology* 156, pp. 103–110. Available at: http://dx.doi.org/10.1016/j.enggeo.2013.01.021.

Wang, W. et al. 2017. Perturbation of fluvial sediment fluxes following the 2008 Wenchuan earthquake. *Earth Surface Processes and Landforms* 42(15), pp. 2611–2622. doi: 10.1002/esp.4210.

Weidinger, J.T. et al. 2014. Giant rockslides from the inside. *Earth and Planetary Science Letters* 389, pp. 62–73. Available at: http://dx.doi.org/10.1016/j.epsl.2013.12.017.

Wells, D.L. and Coppersmith, Kevin, J. 1994. New empical relationship between magnitude, rupture length, rupture width, rupture area, and surface displacement. *Bulletin of the Seismological Society of America* 84(4), pp. 974–1002.

West, A.J. et al. 2014. Dilution of10Be in detrital quartz by earthquake-induced landslides:

Implications for determining denudation rates and potential to provide insights into landslide sediment dynamics. *Earth and Planetary Science Letters* 396, pp. 143–153. Available at: http://dx.doi.org/10.1016/j.epsl.2014.03.058.

Whipple, K.X. 2004. Bedrock Rivers and the Geomorphology of Active Orogens. *Annual Review of Earth and Planetary Sciences* 32(1), pp. 151–185. Available at: http://www.annualreviews.org/doi/10.1146/annurev.earth.32.101802.120356.

Wilkinson, P.L. et al. 2002. An integrated hydrological model for rain-induced landslide prediction. *Earth Surface Processes and Landforms* 27(12), pp. 1285–1297. doi: 10.1002/esp.409.

Williams, J.G. et al. 2018. Satellite-based emergency mapping using optical imagery: Experience and reflections from the 2015 Nepal earthquakes. *Natural Hazards and Earth System Sciences* 18(1), pp. 185–205. doi: 10.5194/nhess-18-185-2018.

Xu, C. et al. 2014. Three (nearly) complete inventories of landslides triggered by the May 12, 2008 Wenchuan Mw 7.9 earthquake of China and their spatial distribution statistical analysis. *Landslides* 11(3), pp. 441–461. doi: 10.1007/s10346-013-0404-6.

Xu, X. et al. 2009. Coseismic reverse- and oblique-slip surface faulting generated by the 2008 Mw 7.9 Wenchuan earthquake, China. *Geology* 37(6), pp. 515–518. doi: 10.1130/G25462A.1.

Yanites, B.J. et al. 2009. Numerical and analytical models of cosmogenic radionuclide dynamics in landslide-dominated drainage basins. *Journal of Geophysical Research: Earth Surface* 114(1). doi: 10.1029/2008JF001088.

Yanites, B.J. et al. 2010. How rivers react to large earthquakes: Evidence from central Taiwan. *Geology* 38(7), pp. 639–642. Available at: http://pubs.geoscienceworld.org/geology/article/38/7/639/130315/How-rivers-react-to-large-earthquakes-Evidence.

Yanites, B.J. et al. 2018. Landslides control the spatial and temporal variation of channel width in southern Taiwan: Implications for landscape evolution and cascading hazards in steep, tectonically active landscapes. *Earth Surface Processes and Landforms* . doi: 10.1002/esp.4353.

Yu, B. et al. 2013. Case study of a giant debris flow in the Wenjia Gully, Sichuan Province, China. *Natural Hazards* 65(1), pp. 835–849. doi: 10.1007/s11069-012-0395-y.

Yunus, A.P. et al. 2020. Decadal vegetation succession from MODIS reveals the spatio-

temporal evolution of post-seismic landsliding after the 2008 Wenchuan earthquake. *Remote Sensing of Environment* 236(October 2019), p. 111476. Available at: https://doi.org/10.1016/j.rse.2019.111476.

Zhang, F. et al. 2019. Monsoonal control on a delayed response of sedimentation to the 2008 Wenchuan earthquake. *Science Advances* 5(6). Available at: http://advances.sciencemag.org/lookup/doi/10.1126/sciadv.aav7110.

Zhang, L. et al. 2012. Emergency medical rescue efforts after a major earthquake: Lessons from the 2008 Wenchuan earthquake. *The Lancet* 379(9818), pp. 853–861. Available at: http://dx.doi.org/10.1016/S0140-6736(11)61876-X.

Zhang, P.Z. et al. 2004. Continuous deformation of the Tibetan Plateau from global positioning system data. *Geology* 32(9), pp. 809–812. doi: 10.1130/G20554.1.

Zhang, S. et al. 2014a. Characteristics of earthquake- and rain-induced landslides near the epicenter of Wenchuan earthquake. *Engineering Geology* 175(May 2008), pp. 58–73. Available at: http://dx.doi.org/10.1016/j.enggeo.2014.03.012.

Zhang, S. et al. 2014b. Relationships among three repeated large-scale debris flows at Pubugou Ravine in the Wenchuan earthquake zone. *Canadian Geotechnical Journal* 51(9), pp. 951–965. Available at: http://www.nrcresearchpress.com/doi/abs/10.1139/cgj-2013-0368.

Zhang, S. et al. 2016. Evolution of Mass Movements near Epicentre of Wenchuan Earthquake, the First Eight Years. *Scientific Reports* 6(December 2015), pp. 1–9. Available at: http://dx.doi.org/10.1038/srep36154.

Zhang, S. and Zhang, L.M. 2017. Impact of the 2008 Wenchuan earthquake in China on subsequent long-term debris flow activities in the epicentral area. *Geomorphology* 276, pp. 86–103. Available at: http://dx.doi.org/10.1016/j.geomorph.2016.10.009.

Zhou, R. et al. 2007. Active Tectonics of the Longmen Shan Region on the Eastern Margin of the Tibetan Plateau. *Acta Geologica Sinica - English Edition* 81(4), pp. 593–604. doi: 10.1111/j.1755-6724.2007.tb00983.x.

Chapter 8 Appendix

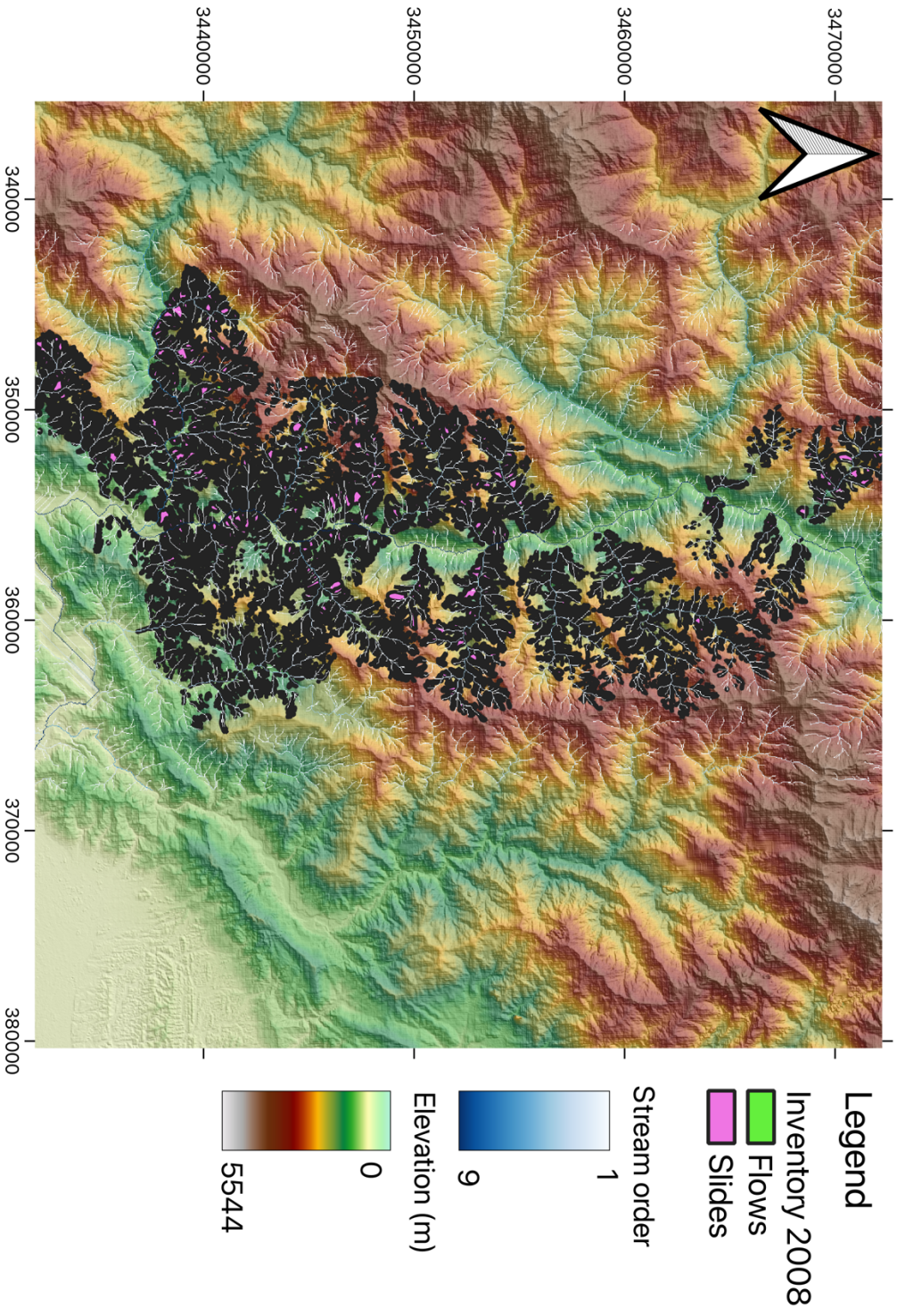

Apx Figure 1 The full inventory of the coseismic mass movements on a (30m) hillshaded relief map with the delineated stream network. The stream network is coloured by the Strahler stream order. The main trunk of the Min Jiang flows from north to south in this image.

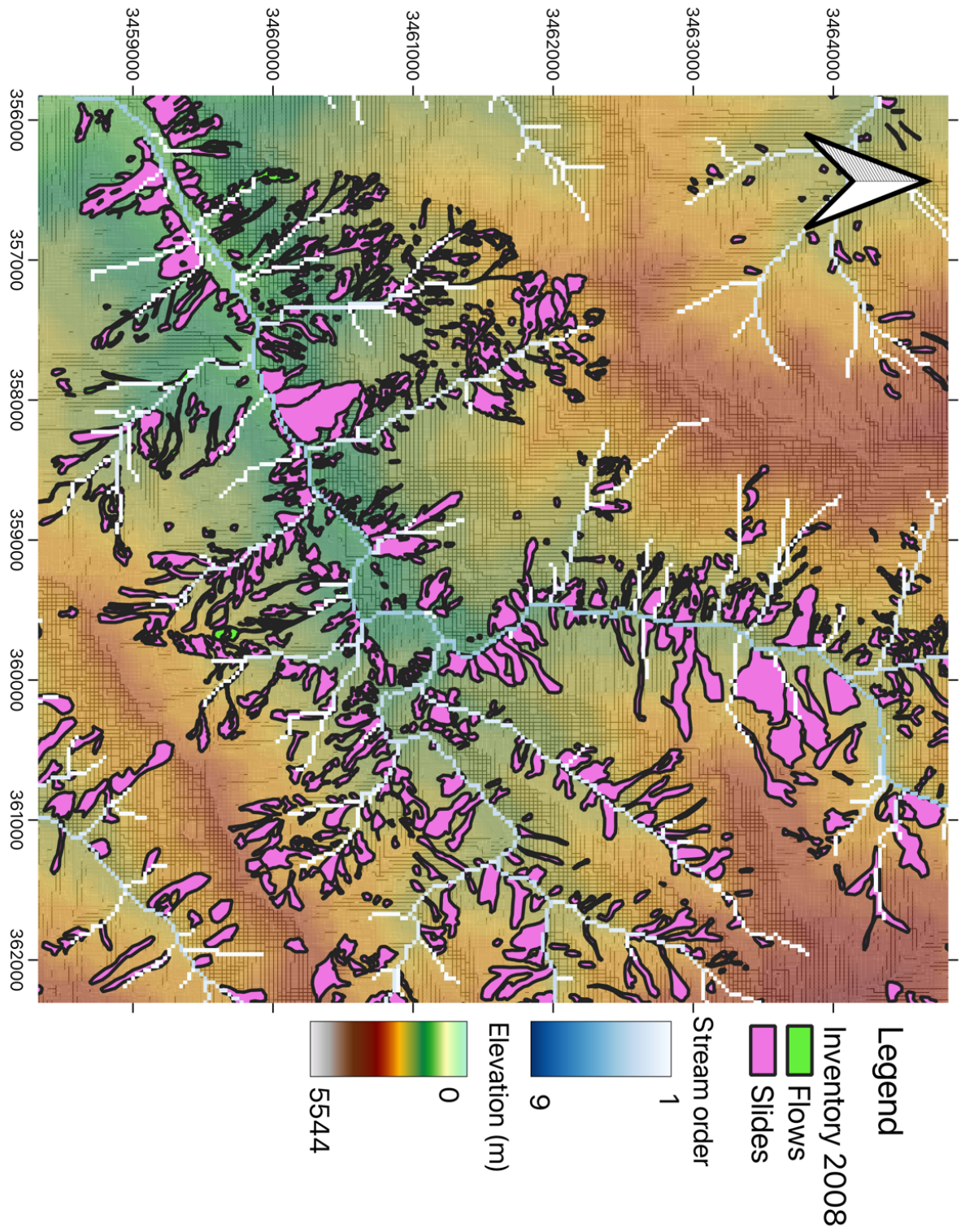

Apx Figure 2 Zoomed in section of the coseismic mass movement inventory with slides highlighted in pink and flows highlighted in green. The inventory is shown on top of a (30m) hillshaded relief map and delineated stream network coloured by the Strahler stream order.

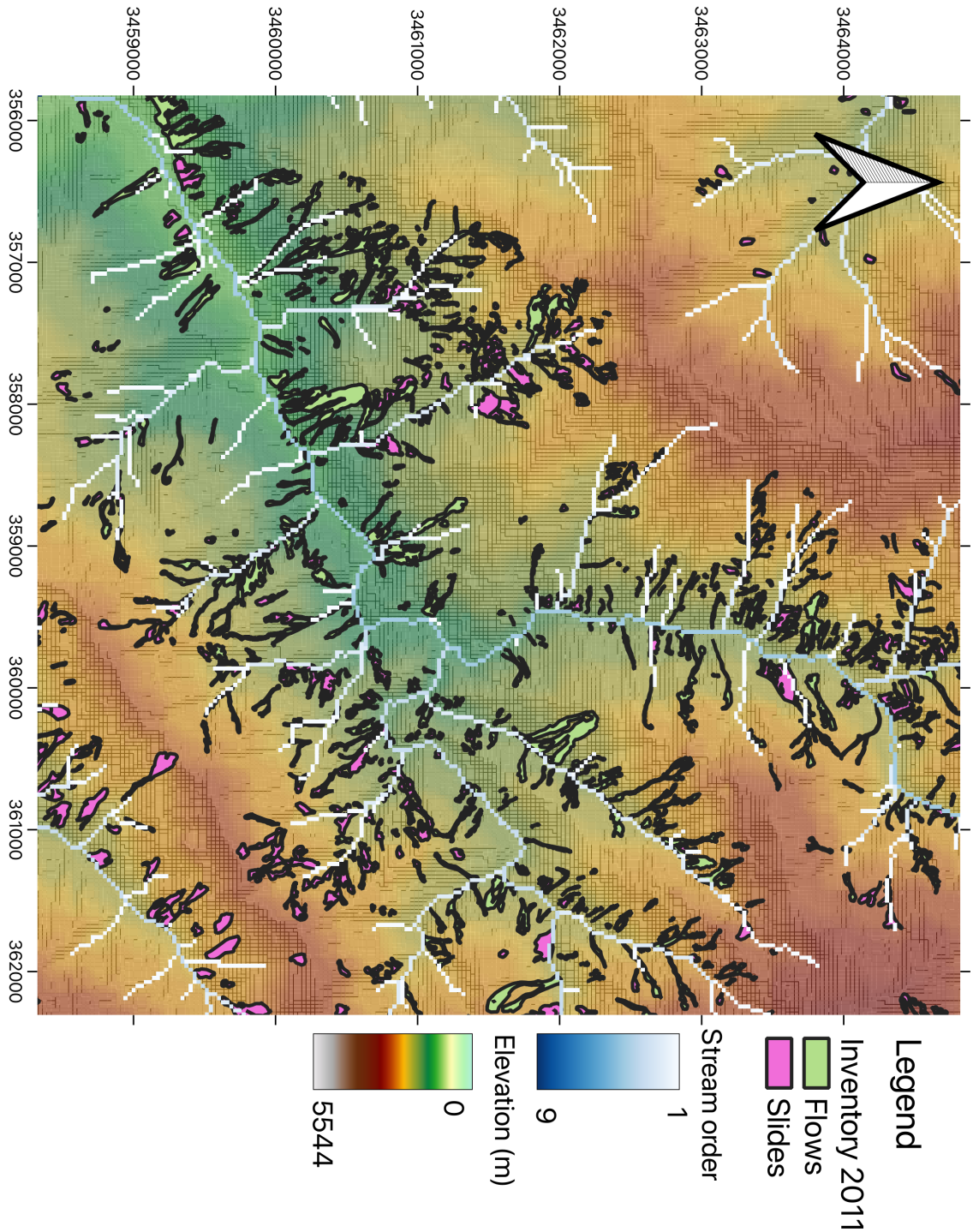

Apx Figure 3 Zoomed in section of the 2011 inventory with flows shown in green and slides shown in pink. As before the inventory is on a (30m) hillshaded relief map with the delineated Strahler stream order.

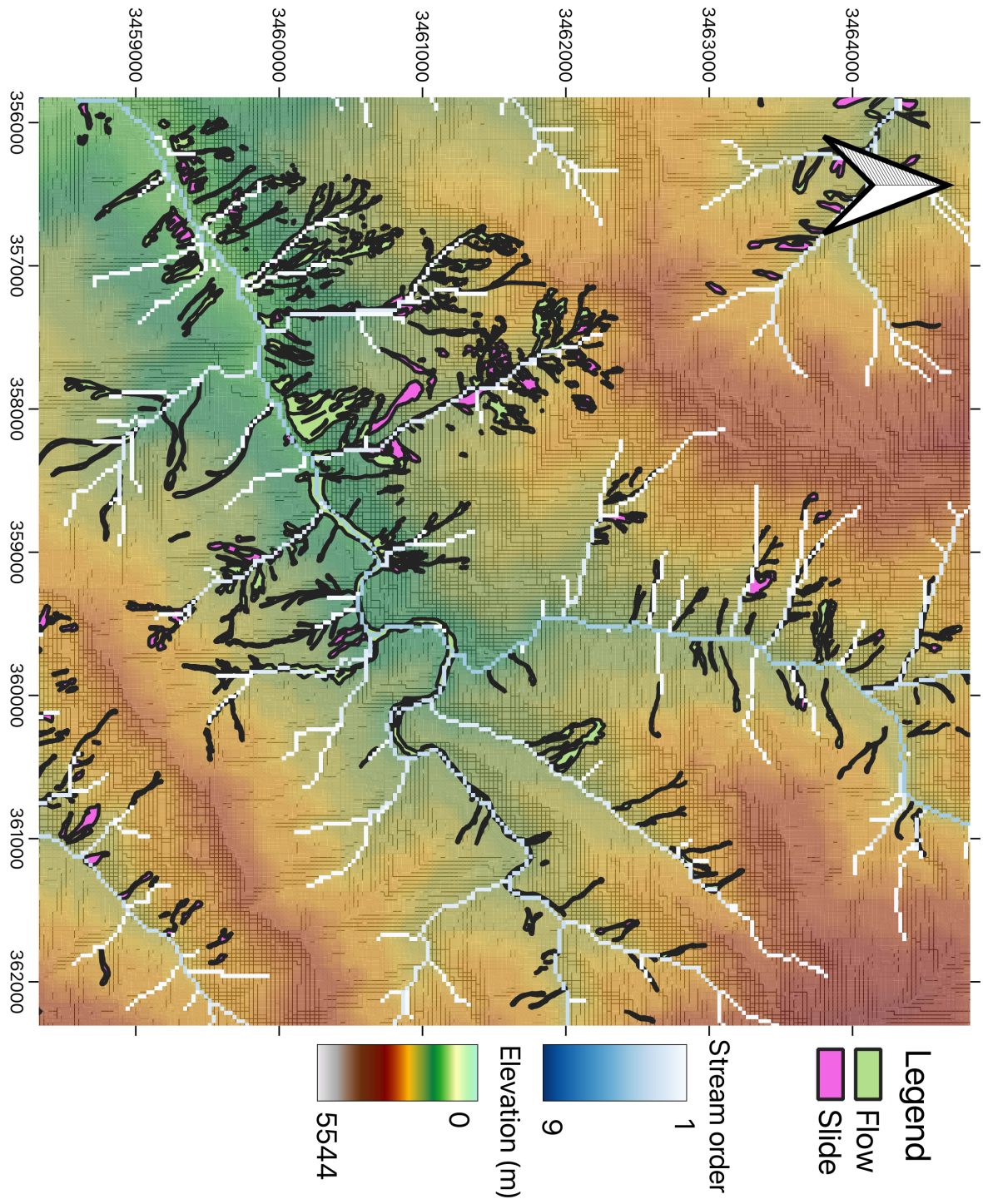

Apx Figure 4 A section of the 2013 mass movement inventory categorised by movement type on a (30m) hillshaded relief map with a delineated steam network coloured by Strahler stream order.

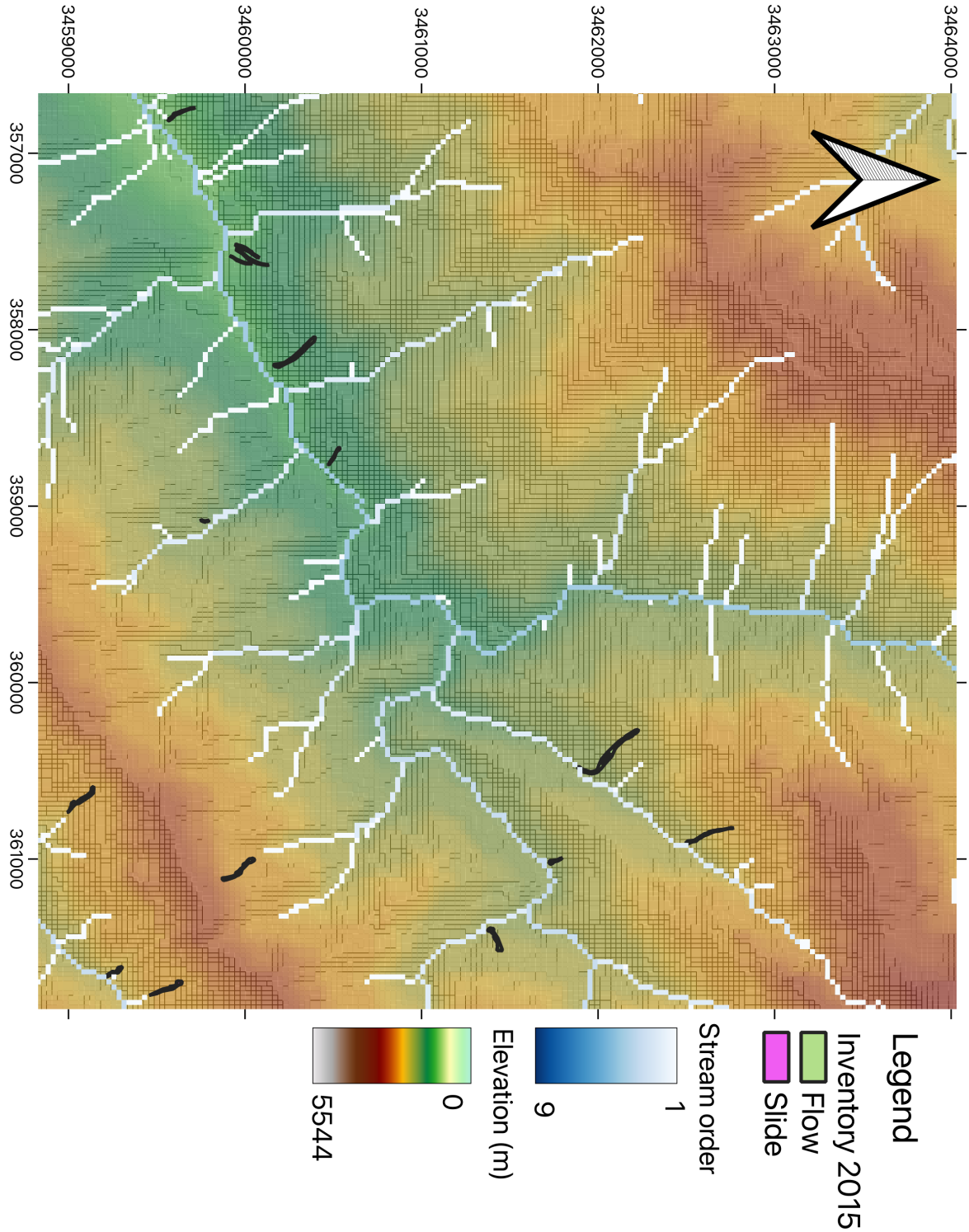

Apx Figure 5 Section of the 2015 mass movement inventory on a (30m) hillshaded relief map with the delineated stream order coloured by Strahler stream order. Note the significant decrease in the number of mass movements mapped due to the decrease in activity on the hillslope.

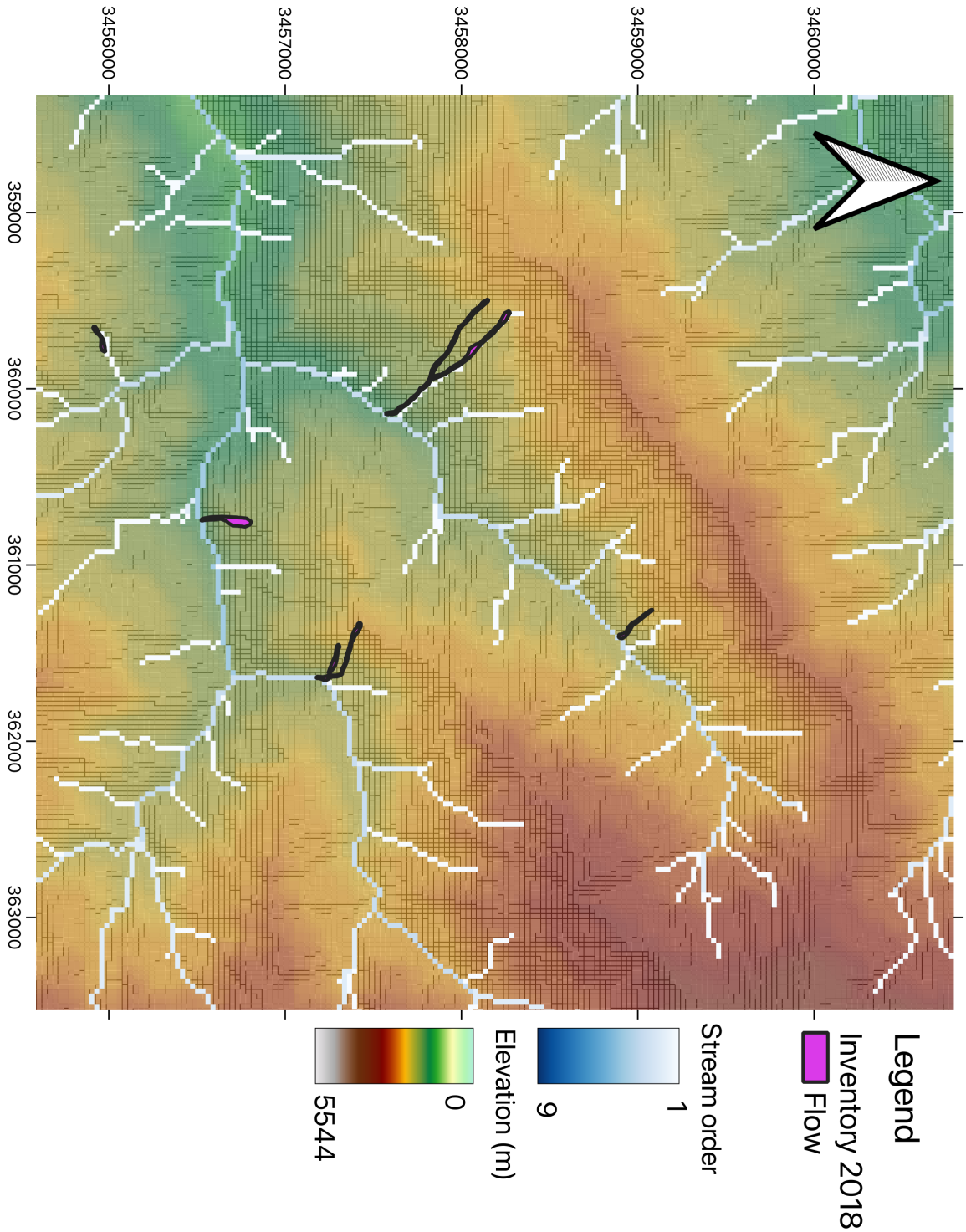

Apx Figure 6 Section of the 2018 mass movement inventory on a (30m) hillshaded relief map with the delineated stream order coloured by Strahler stream order. Mass movements frequency has again decreased.

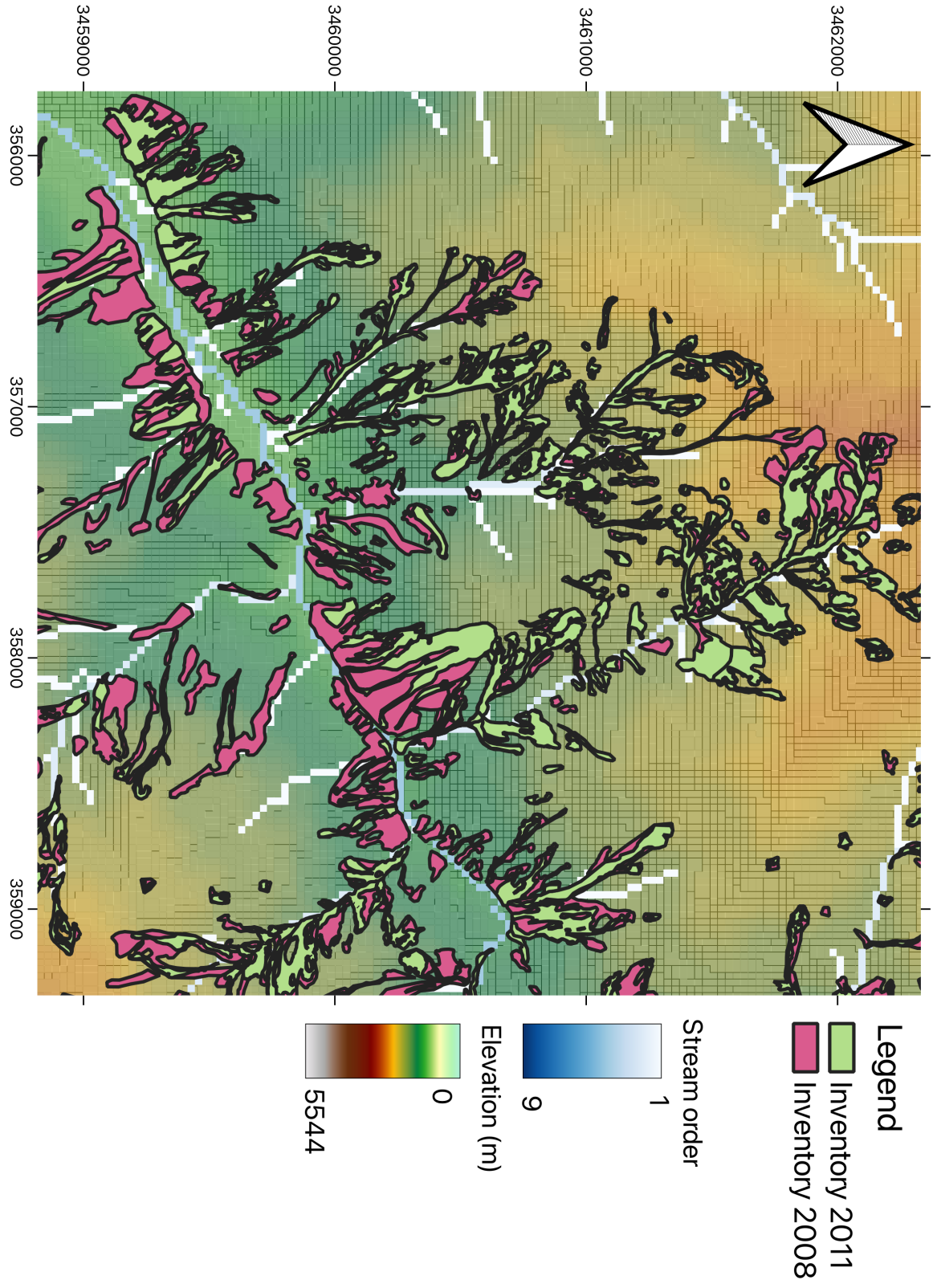

Apx Figure 7 A section of the 2001 inventory overlaying the 2008 coseismic landslide map. Using intersects and the delineated stream network I determine which coseismic landslides have been eroded and wherever they have transferred sediment into the channel network or not.

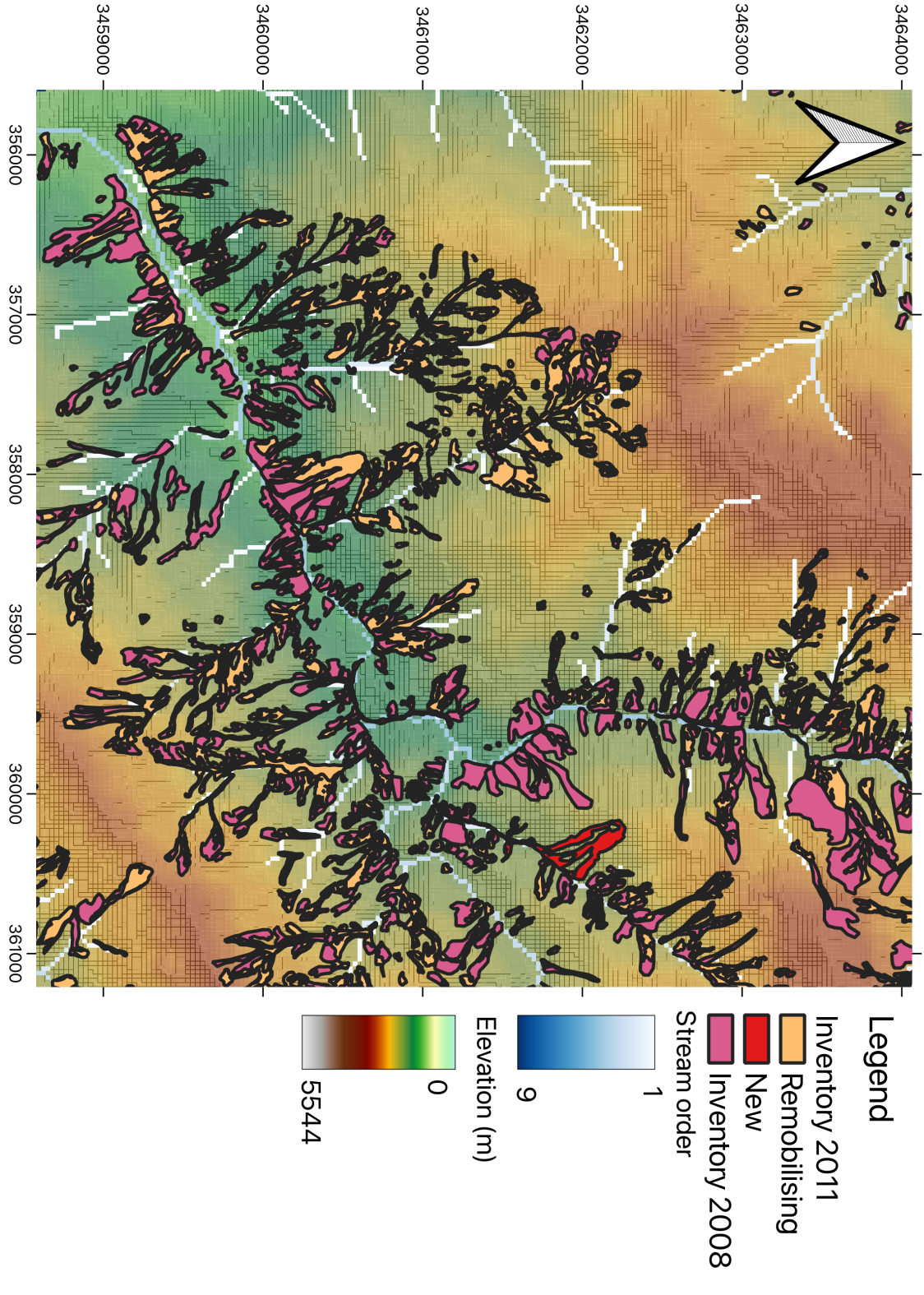

Apx Figure 8 The 2011 inventory overlying the coseismic 2008 landslide inventory with the hillshaded relief map and delineated stream network. Here the 2011 inventory is separated into remobilising and new mass movements depending on their relationship with the cosiesmic landslides. Any landslide mapped in the 2011 inventory which intersects with the 2008 inventory is classed as remobilising while any not associated with previous movements are classed as new or post seismic.

Apx Table 1 Summary statistics of the multitemporal landslide inventory by year. Volumes are determined by the area – volume scaling relationships derived in chapter 3.

Year	Number of mass movements mapped	Smallest mapped area (m^2)	Largest mapped Area (m^2)	Total Area (m^2)	Total volume (m^3)
2008	8917	30	6×10^5	1×10^8	4×10^8 ($+4\times10^8/-3\times10^8$)
2011 New	832	44	5×10^5	5×10^6	6×10^5 ($\pm4\times10^5$)
2011 Remobilisation	4099	35	3×10^5	4×10^7	$7\times10^6(\pm4\times10^6)$
2013 New	387	121	5×10^5	3×10^6	1×10^5 ($\pm5\times10^5$)
2013 Remobilisation	1152	55	5×10^5	1×10^7	9×10^5 ($\pm2\times10^5$)
2015 New	14	1672	7×10^4	2×10^5	2×10^5 ($\pm1\times10^4$)
2015 Remobilisation	273	35	4×10^5	6×10^6	2×10^6 ($\pm1\times10^6$)
2018 New	14	228	3×10^4	8×10^4	6×10^4 ($\pm3\times10^4$)
2018 Remobilisation	51	292	7×10^4	6×10^5	6×10^5 ($\pm3\times10^5$)